AD-A056 732 CALIFORNIA UNIV LIVERMORE LAWRENCE LIVERMORE LAB F/G 20/14
SOMINT: AN IMPROVED MODEL FOR STUDYING CONDUCTING OBJECTS NEAR --ETC(U)
FEB 78 J N BRITTINGHAM, E K MILLER, J T OKADA W-7405-ENG-48
UNCLASSIFIED UCRL-52423 NL

1 OF 2
AD A056732

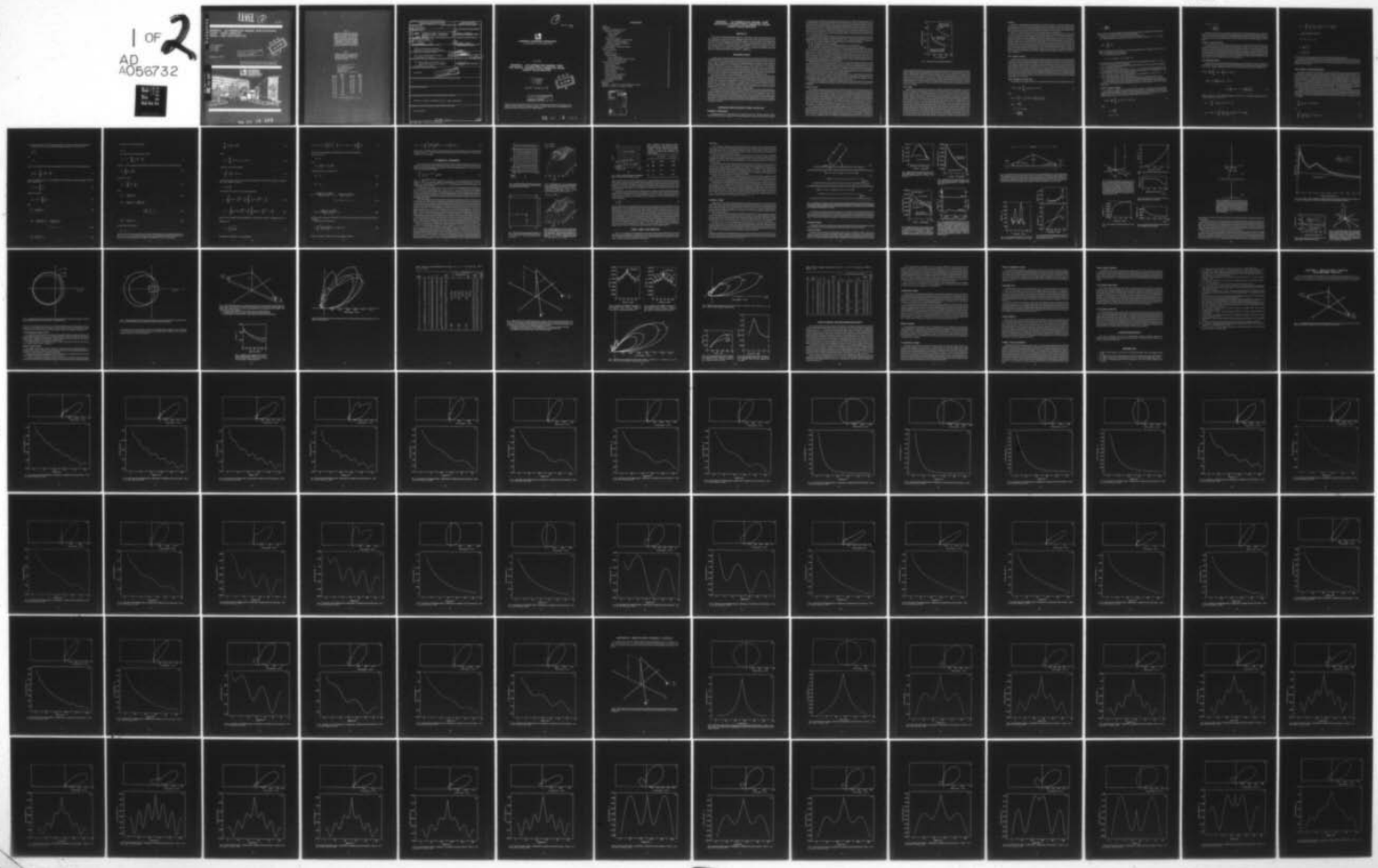

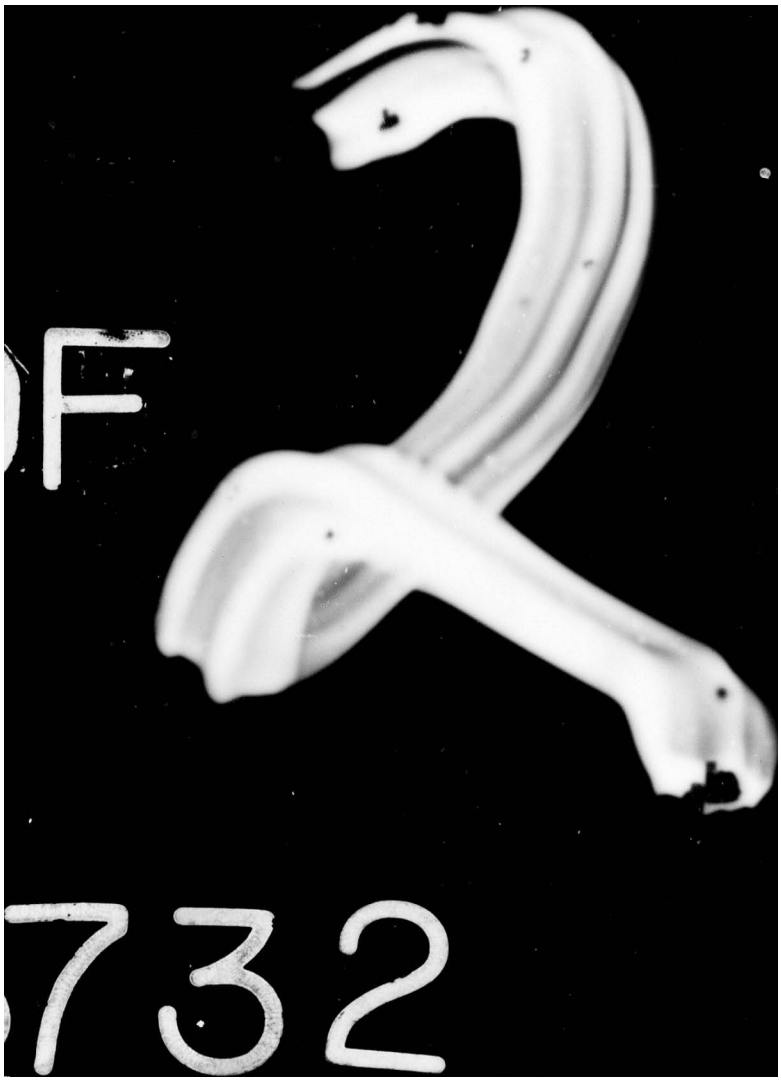
F
732

AD A056732

LEVEL II

UCRL-52423

SOMINT: AN IMPROVED MODEL FOR STUDYING CONDUCTING OBJECTS NEAR LOSSY HALF-SPACES

J. N. Brittingham
E. K. Miller
J. T. Okada

DDC
RECEIVED
JUL 26 1978
F

This document has been approved for public release and sale; its distribution is unlimited.

February 24, 1978

Work performed under the auspices of the U.S. Department of Energy by the UCLLL under contract number W-7405-ENG-48.

DDC FILE COPY

78 07 25 043

NOTICE

"This report was prepared as an account of work sponsored by the United States Government. Neither the United States nor the United States Department of Energy, nor any of their employees, nor any of their contractors, subcontractors, or their employees, makes any warranty, express or implied, or assumes any legal liability or responsibility for the accuracy, completeness or usefulness of any information, apparatus, product or process disclosed, or represents that its use would not infringe privately-owned rights."

NOTICE

Reference to a company or product name does not imply approval or recommendation of the product by the University of California or the U.S. Department of Energy to the exclusion of others that may be suitable.

Printed in the United States of America
Available from
National Technical Information Service
U.S. Department of Commerce
5285 Port Royal Road
Springfield, VA 22161
Price: Printed Copy $; Microfiche $3.00

Page Range	Domestic Price	Page Range	Domestic Price
001-025	$ 4.00	326-350	$12.00
026-050	4.50	351-375	12.50
051-075	5.25	376-400	13.00
076-100	6.00	401-425	13.25
101-125	6.50	426-450	14.00
126-150	7.25	451-475	14.50
151-175	8.00	476-500	15.00
176-200	9.00	501-525	15.25
201-225	9.25	526-550	15.50
226-250	9.50	551-575	16.25
251-275	10.75	576-600	16.50
276-300	11.00	601-up	--[1]
301-325	11.75		

[1] Add $2.50 for each additional 100-page increment from 601 pages up.

SECURITY CLASSIFICATION OF THIS PAGE *(When Data Entered)*

REPORT DOCUMENTATION PAGE

READ INSTRUCTIONS BEFORE COMPLETING FORM

1. REPORT NUMBER: UCRL-52423	2. GOVT ACCESSION NO.
3. RECIPIENT'S CATALOG NUMBER	
4. TITLE (and Subtitle): SOMINT: AN IMPROVED MODEL FOR STUDYING CONDUCTING OBJECTS NEAR LOSSY Half-SPACES	5. TYPE OF REPORT & PERIOD COVERED: Final rept.
6. PERFORMING ORG. REPORT NUMBER	
7. AUTHOR(s): J. N. Brittingham, E. K. Miller, J. T. Okada	8. CONTRACT OR GRANT NUMBER(s): W-7405-Eng-48
9. PERFORMING ORGANIZATION NAME AND ADDRESS: Lawrence Livermore Laboratory, University of California/Livermore	10. PROGRAM ELEMENT, PROJECT, TASK AREA & WORK UNIT NUMBERS: 011700
11. CONTROLLING OFFICE NAME AND ADDRESS: U.S. Army Communications Command, Ft Huachuca, AZ 85613	12. REPORT DATE: Feb 24 1978
	13. NUMBER OF PAGES: 92
14. MONITORING AGENCY NAME & ADDRESS *(if different from Controlling Office)*: U.S. Army Communications-Electronics Engineering Installation Agency, Ft Huachuca, AZ 85613	15. SECURITY CLASS. *(of this report)*: Unclassified
	15a. DECLASSIFICATION/DOWNGRADING SCHEDULE

16. DISTRIBUTION STATEMENT *(of this Report)*

Unlimited

This document has been approved for public release and sale; its distribution is unlimited.

17. DISTRIBUTION STATEMENT *(of the abstract entered in Block 20, if different from Report)*

18. SUPPLEMENTARY NOTES

19. KEY WORDS *(Continue on reverse side if necessary and identify by block number)*

HF Radio, Antenna, Transmission loss, earth absorbtion.

20. ABSTRACT *(Continue on reverse side if necessary and identify by block number)*

Copy abstract.

390 999

DD FORM 1 JAN 73 1473 EDITION OF 1 NOV 65 IS OBSOLETE

Distribution Category
UC-37

LAWRENCE LIVERMORE LABORATORY
University of California / Livermore, California / 94550

UCRL-52423

SOMINT: AN IMPROVED MODEL FOR STUDYING CONDUCTING OBJECTS NEAR LOSSY HALF-SPACES

J. N. Brittingham
E. K. Miller
J. T. Okada

MS. date: February 24, 1978

DDC
RECEIVED
JUL 26 1978
F

This document has been approved for public release and sale; its distribution is unlimited.

This work was supported by the U.S. Army Communication Electronics Engineering Installation Agency under the auspices of the U.S. Energy Research and Development Administration under Contract No. W-7405-ENG-48.

78 07 25 043

CONTENTS

Abstract 1
Introduction 1
Methods for Studying Wire Antennas 1
Preliminary Considerations 1
Junction Treatment 2
Source Models 3
Integration 4
Wire Antenna Analysis 4
Infinite, Homogeneous, Isotropic Media 4
Perfectly Conducting Half-Space 5
Imperfectly Conducting Half-Space 6
The Sommerfeld Theory 6
Series Solution to Sommerfeld Integrals 7
Numerical Methods 12
Test Cases and Results 14
Test Cases 15
Preliminary Results 15
Parametric Results 16
Ground-Screen Effects 16
Vertical Half-Rhombic Parametric Results 22
Sloping V Parametric Results 22
Conclusions and Recommendations 30
Ground-Screen Models 31
Dielectric Sheaths 31
Two-Half-Space Problem 31
Effect of Nonuniform Currents 32
Penetrating Wires 32
Antenna Efficiency 32
Frequency Domain Interpolation 32
Nonwire Integral Equations 33
User-Oriented Improvements 33
User-Experience Data Base 33
Acknowledgments 33
References 33
Appendix A. Results for a Vertical Half-Rhombic Antenna 35
Appendix B. Results for a Sloping V Antenna 70

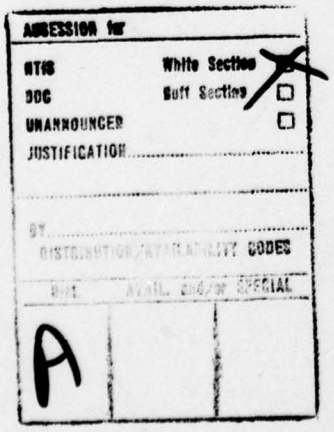

SOMINT: AN IMPROVED MODEL FOR STUDYING CONDUCTING OBJECTS NEAR LOSSY HALF-SPACES

ABSTRACT

This report summarizes the development of a moment-method numerical code to study wire antennas near lossy earth. The computation time of this code is greatly reduced by two new methods for evaluating the Sommerfeld integrals. In the evaluation of the integrals off the earth, a bivariate interpolation scheme on a prestored grid is shown to give very quick and accurate results. A new series solution is presented to evaluate the integral for values near the interface. Test results of this program are given, along with extensive numerical data on vertical half-rhombic and sloping V antennas.

INTRODUCTION

A problem that has traditionally resisted a genuinely practical solution despite considerable study is that of modeling conducting structures (antennas or scatterers) located near a planar interface such as the earth's surface. Nearly 70 years ago Sommerfeld (1909) worked out the basis for its rigorous solution in terms of Fourier integrals of cylindrical wave expansions. The Sommerfeld integrals have been extensively studied, and numerous approximations have been developed for them for various combinations of the problem's parameters.[1] However, evaluation of the Sommerfeld integrals for the ranges of source and observation points that typically must be covered for any self-consistent description of the structure's current—an integral equation for example—almost inevitably involves some parameter combinations to which such approximations do not apply. Consequently, the only feasible approach for obtaining a reliable solution in such cases has been to *numerically* integrate the Sommerfeld integrals, a computationally inefficient process.

This situation has, until now, kept moment-method models of wire antennas based on internal-equation formulations too expensive for routine use in treating the half-space problem. In this report we present a new approach to the interface problem that is based on an old (interpolation) numerical procedure. Our interpolation approach, which we refer to as SOMINT for convenience, is shown below to make computer modeling of antennas near an interface now affordable. For example, relative to the free-space computation, the time penalty for rigorous treatment of the interface-reflected fields will be ultimately a factor of only 5 to 10 vs the former value of 100 to 1000. Consequently, a whole new range of problems becomes practicable, including, as illustrated here, radiation-pattern control through ground-screen design.

The second section of this report provides analytical background for the interface problems and formulation of the integral equations upon which our approach is based. The third section discusses the numerical procedures employed, including the interpolation treatment that is the key contribution of this work. Numerical results are given in the fourth section: first a series of test cases and preliminary calculation and then the results of some parametric calculations performed for two Army antennas, the vertical half-rhombic and sloping V. The final section presents our conclusions and recommendations for future work. Two appendices contain representative plots of radiation patterns and current magnitude values for vertical half-rhombic and sloping V antennas.

METHODS FOR STUDYING WIRE ANTENNAS

Preliminary Considerations

An integral equation for a wire structure can be derived in many ways. The basic procedure involves writing Maxwell's equations in integral form to express the scattered or secondary fields in terms of integrals

over induced-source distributions. Expressing the secondary field over loci of points where the behavior of the total field (incident or primary plus secondary) is known via boundary or continuity conditions yields an integral equation for the induced source in terms of the primary field. Two broad general classes of integral equations result, depending on whether the forcing function (primary field) is electric or magnetic. An electric forcing function gives rise to a Fredholm integral equation of the first kind (so called because the unknown appears only under the integral). A magnetic forcing field gives rise to a Fredholm integral equation of the second kind (in which the unknown also appears outside the integral). While derivatives of the unknown may occur as well, these equations are commonly termed integral equations, rather than integro-differential equations, as would be strictly correct.

Generally speaking, the magnetic-field type of integral equation has been found better suited for smooth, closed surfaces than for thin-plate or shell geometries and wires. [2] The converse is generally true for the electric-field type of integral equation, which, accordingly, is most commonly employed for treating wire structures. Also involved in developing wire integral equations are three approximations:

- The circumferential current is negligible,
- The circumferential variation of the longitudinal current can be ignored; and
- The thin-wire or reduced kernel can be used in place of the actual surface integration.

Many analytically equivalent integral equations for wires based upon the electric field can be derived. Three of the most commonly employed are the Hallen or vector potential type, [3] the scalar-vector (mixed) potential version, [4] and the Pocklington integral equation. [5] All are solved within the framework of the moment (or matrix) method, but each exhibits distinctive characteristics that must be taken into account in its numerical treatment. The Hallen equation, for example, can produce results using a pulse-current basis of accuracy comparable to those obtained from the Pocklington equation solved with a three-term (constant, sine, and cosine) basis for simple structures. [6] The Hallen equation is not, however, readily extendable to the complex geometries that the Pocklington equation can handle. [7]

Although pulse-current [8,9] and linear-current [10] bases have been quite widely used, and can, under suitable circumstances, be essentially equivalent, they are not as efficient for modeling traveling wave equation, as are sinusoidal bases that possess nonconstant derivatives and can closely resemble the actual current solution. Sinusoidal bases have appeared in subsectional or subdomain form in both the three-term expansion mentioned above and in the piecewise sinusoidal [5] or two-term form. Fourier series have also been studied as complete-domain sinusoidal bases, but have not been widely adopted because they require more integration effort than subsectional bases and can lead to ill-conditioned matrices. [8]

The weight or test functions most often used have been delta functions, although Galerkin's method with both linear (two-term) [10] and sinusoidal (two-term) [5] functions has also been quite widely applied. The term "point matching" refers to the use of delta-function weights. A comparison of numerical convergence rates for several common methods applied to a straight-wire scatterer is shown in Fig. 1. [11]

In addition to the problem of choosing basis and weight functions, other special aspects of the numerical development must be considered when selecting a code for computer modeling. Three of these aspects are discussed below.

Junction Treatment

Any subsectional approach that employs either finite-difference operators in the integral equation or any other basis than pulse-current requires special consideration of both simple (two wires) and multiple (three or more wires) junctions. The problem essentially is to relate, in some physically and mathematically reasonable way, the current basis of each subsection (segment) to those of its neighbors. When pulse bases are used in the scalar-vector potential integral equation, the finite-difference operator spans two segments and thus leads to a charge involving the two corresponding pulse-current samples. [4] For two- or three-term bases, the condition of current amplitude and slope continuity at each simple juction leads to equations that permit all the constants in the current expansion to be given in terms of current samples at the segment junctions or centers. [6] Yeh and Mei [12] developed a slightly different handling of the three-term basis in which the current is extrapolated from a given segment to the adjacent segment centers, but which is otherwise basically the same.

For a multiple junction, the treatment can become considerably more involved. The pulse-basis approach mentioned above has been extended to the multiple junction [9] by dividing the total junction charge between the junction segments according to the ratio of their individual areas to the total area on a logarithmic basis in radius and linear in segment length. This approach has been found useful for the three-term expansion as well. [6] The two-term expansions have been applied to multiple junctions by overlapping M – 1 of the bases a pair at a time at an M-segment junction. [10] Applications of the three-term expansion to the multiple junction

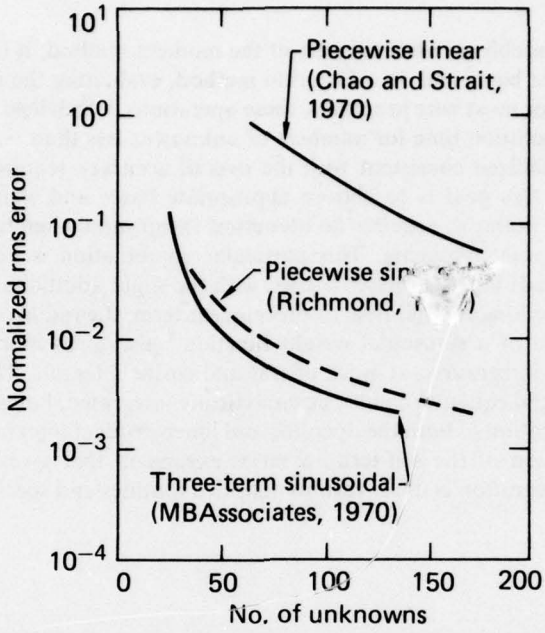

Fig. 1. Convergence rate for several solution methods (Ref. 11).

has been accomplished by MBAssociates using the Yeh and Mei simple-junction procedure by incorporating a composite segment having the averaged length and total current of the M – 1 connected segments. [13] A more elaborate multiple-junction approach has been developed for the three-term expansion by Andreasen and Harris. [14] Their procedure apparently is the only one in which the junction geometry plays an explicit role in establishing the current relationships at the junction. Although all of these approaches evidently can produce satisfactory results, there is little or no direct evidence of their validity in terms of the junction current and charge distributions. It should be noted that the numerical results have been found in some cases to be quite sensitive to the junction treatment. [6] Further, the above list by no means exhausts all possible alternatives for the junction treatment.

Source Models

Determination of quantities such as absolute gain, efficiency, radiated power, input power, etc., requires not only the antenna current distribution but also the input characteristics, particularly the feedpoint impedance (or admittance). The feedpoint admittance can be found in various ways, but using the integral-equation approach ordinarily also involves defining it in terms of source-region current per unit of terminal voltage. Calculation of this quantity requires a realistic source model that not only provides an appropriate means for numerically exciting the antenna, but also permits ready evaluation or specification of the effective terminal voltage. Thus if, as in a point-matching procedure, the excitation arises as a tangential field on the source segment of length Δ, the driving voltage might be assumed to be $-E^I\Delta$ if E^I is constant on the source segment and zero elsewhere. This assumption may be invalid, however, with the result that the actual voltage can be obtained only by integrating the tangential field in the vicinity of the source segment. [6] Somewhat less ambiguity should arise from Galerkin-type approaches where the boundary conditions are integrated, so that the classical delta-function source might be numerically approximated. An alternative source model for point-matching is provided as a current-slope discontinuity, which also approximates a delta-function source field. The current bases, junction treatment, and weight functions can all influence the usefulness of these alternative source models. In case of uncertainty, once the current distribution has been found, the impedance can be computed from the classical emf method, although at the expense of the additional integration this entails.

Integration

Integration is understandably an essential part of the moment method; it is involved in applying the integral operator to the current bases and, in a Galerkin method, evaluating the inner product of these results with the weight functions. For most wire programs, these operations, which lead to the generalized impedance matrix, dominate the total solution time for numbers of unknowns less than ~200. It is thus important that the integration time be minimized consistent with the overall accuracy requirements.

One way to approach this goal is to choose appropriate bases and weight functions. The two-term sinusoidal current basis, for example, requires no numerical integration when the Pocklington integral equation is used together with point matching. This particular combination is not very accurate, however. [11] Adding the constant term leads to much better results, with the slight additional expense of the numerical integration required to find the longitudinal field of this current term; the radial component can be analytically expressed. Alternatively, use of a sinusoidal weight function [5] also gives much improved results and surprisingly requires numerical integration, at most, of sine and cosine integrals. The piecewise linear basis used with the scalar-vector potential equation cannot be analytically integrated, but good results are obtained with four-point rectangular integration of both the operator and inner-product integrals. In addition, instead of applying a numerical integration of the self-term, a series expansion that gives a closed-form expression is used. [15] When numerical integration is used, various adaptive routines and special techniques are available to improve efficiency. [16]

Wire Antenna Analysis

Examining the many options available to the analyst concerning the integral equation to be selected and its numerical treatment in developing a computer model for application to wire antennas would take this discussion beyond reasonable lengths. Accordingly our attention is primarily directed to an approach based on the Pocklington integral equation solved using a three-term subsectional basis (constant, sine, and cosine) and point-matching. Unless otherwise indicated, antenna sources are introduced as tangential electric fields, with the Yeh and Mei [12] form of current extrapolation used for simple junctions and the Curtis method for multiple junctions. Both the source model and junction (simple and multiple) treatment used in this code may exhibit deficiencies, but when applied with care (e.g., equal segment lengths near sources and at multiple junctions) the code has proven valid and reliable. A brief overview of the relevant equations and numerical treatment used for free space and various interface theories and some special topics is given in this section. Numerical results appear in a later section.

Infinite, Homogeneous, Isotropic Media

The Pocklington-type integral equation for a wire structure of contour $C(\bar{r})$ can be expressed in the form

$$\hat{s} \cdot \bar{E}^I(s) = \frac{i\omega\mu}{4\pi} \int_{C(\bar{r})} I(s') G_0(s,s')\, ds';\ s \in C(\bar{r}) , \tag{1}$$

where

$$G_0(s,s') = \left[\hat{s} \cdot \hat{s}' + \frac{1}{k^2} (\hat{s} \cdot \nabla)(\hat{s}' \cdot \nabla)\right] \times \left[g_0(\bar{r},\bar{r}')\right] ,$$

$$g_0(r,r') = \frac{e^{-ikR}}{R} ,$$

$$R = |\bar{r} - \bar{r}'| \geq a(\bar{r}) ,$$

$$\hat{s} = \frac{\nabla C(\bar{r})}{|\nabla C(\bar{r})|} ,$$

and

$$\hat{s} = \frac{\nabla C(r')}{|\nabla C(r')|} ;$$

where, as usual, k is the inifinite-medium wave member, the permeability and permittivity are denoted by μ and ϵ, $a(\bar{r})$ is the wire radius at $\bar{r}$, and $\bar{E}^I$ is the incident electric field.

Reduction of this equation to matrix form involves these seven steps:

(1) Approximating C(r) as a piecewise linear sequence of N segments of length Δ_i (i = 1, ..., N), so that

$$C(\bar{r}) \simeq \sum_{i=1}^{N} \Delta_i \hat{s}_i ,$$

with $\hat{s}_i$ the unit tangent vector to $C(\bar{r})$ at $\bar{r} = \bar{r}_i$ (use of straight segments is not mandatory, but it is very convenient in simplifying the current integration);

(2) Introducing the subsectional bases

$$I_i(s') = A_i + B_i \sin[k(s' - s_i)] + C_i \cos[k(s' - s_i)]$$

to represent the unknown current (the final unknowns will be the N sampled current values $I_i = A_i + C_i$ [i = 1, ..., N] at the center of each of the N segments);

(3) A current interpolation procedure whereby the individual A_i, B_i, and C_i constants are expressed in terms of the sampled current values;

(4) Use of the N delta-function weights $\delta(s - s_j)$ (j = 1, ..., N) to obtain an N^{th}-order impedance matrix of N independent field equations (note that the weight functions sample the field at the segment centers, and are thus "collocated" with the current sample locations);

(5) Specification of the N incident or primary field vector components $E_i = E^I(s_j) \cdot \hat{s}_j$ (j = 1, ..., N), which are the tangential fields at the N segment centers;

(6) Matrix manipulation to obtain an admittance equivalent of the impendance matrix; and

(7) Computation of the current distribution and whatever field components, if any, are desired.

The total computer solution time is well approximated by $AN^2 + BN^3$, where A corresponds to step (4) and B to step (6). For the code under consideration here and for a CDC 7600 computer, $A \approx 4 \times 10^{-4}$ s and $B \approx 2 \times 10^{-6}$ s.

Perfectly Conducting Half-Space

As written, Eq. (1) applies to wire structures excited as antennas or scatterers and located in infinite, isotropic, homogeneous media of arbitrary (possibly lossy) permittivity and permeability. It can easily be extended to permit the modeling of magnetic or electric image planes. For example, the perfectly conducting ground analog of Eq. (1) is, for an antenna elevated above a ground plane at z = 0,

$$\hat{s} \cdot \bar{E}^I(s) = \frac{i\omega\mu}{4\pi} \int_{C(\bar{r})} I(s') \, [G_0(s,s') + G_I(s,s'^*)] \, ds' , \qquad (2)$$

where

$$g_I = \frac{e^{-ikR^*}}{R^*}$$

$$R^* = |\bar{r} - \bar{r}'^*| ,$$

$$\bar{r}'^*(x,y,z) = \bar{r}'(x,y,-z) \ ,$$

$$\hat{s}'^* = \frac{\nabla C(\bar{r}'^*)}{|\nabla C(\bar{r}'^*)|} \ .$$

Similar forms can be written for a magnetic interface and for an interior right-angle corner. If the corner angle is otherwise arbitrary but related to π as an integer multiple, a discrete spectrum of angular images is obtained, but the essence of the integral equation form is preserved. Precisely the same line of approach can also be used for interior problems where the wire structure is located between two parallel magnetic or electric planes. [17]

Imperfectly Conducting Half-Space

A problem that is not so computationally simple, but that is of perhaps greater practical interest, is that of an antenna located (buried or elevated) near the ground-air interface. This is a topic of considerable longevity in electromagnetics; a formal solution to the problem was given in 1909 by Sommerfeld. [18] The numerical complexity of evaluating the Sommerfeld integrals (which appear in the integral equation kernel) for arbitrary source and observation-point locations and ground parameters, however, has prevented the Sommerfeld theory from being routinely used for such problems. Consequently, while some progress has been made in applying the Sommerfeld theory, alternative approaches to the antenna-ground problem have also been pursued. These various methods are briefly discussed below.

The Sommerfeld Theory

Details of the steps in deriving the Sommerfeld integrals may be found elsewhere. [19] Here we simply write one version of Eq. (1) that accounts for the interface reflected field via the Sommerfeld theory; alternative forms are also available, differing essentially in how the perfect-ground image terms are handled. It is

$$\hat{s} \cdot \bar{E}^I(s) = \frac{i\omega\mu}{4\pi} \int_{C(\bar{r})} I(s')ds' \times \Bigg\{ G_0(s,s') + G_I(s,s'^*)$$

$$+ \left(\cos\beta + \frac{1}{k^2} \frac{\partial^2}{\partial s \partial z}\right) \sin\beta' \, g_{Hz} - \cos\beta' \, g_{Vz}$$

$$+ \sin\beta' \left[\sin\beta \cos(\alpha - \alpha') + \frac{1}{k^2} \frac{\partial^2}{\partial s \partial t'}\right] g_{Nt} \Bigg\} , \qquad (3)$$

where $\alpha = \alpha(\bar{r})$ and $\beta = \beta(\bar{r})$ are the direction angles of the wire at $\bar{r}$, $\hat{t}'$ is the horizontal projection of $\hat{s}'$, J_n is the Bessel function of order n, and

$$g_{Ht} = 2 \int_0^\infty \frac{\lambda}{\gamma_0 + \gamma_1} J_0(\lambda\rho) \, e^{-\gamma_0(z+z')} \, d\lambda \ ,$$

$$g_{Hz} = -\cos(\phi - \alpha') \int_0^\infty \frac{\gamma_0 - \gamma_1}{k_0^2\gamma_1 + k_1^2\gamma_0} \times \left[J_1(\lambda\rho) \, e^{-\gamma_0(z+z')} \lambda^2 d\lambda\right] ,$$

$$g_{Vz} = 2 \int_0^{\infty} \frac{\gamma_1}{k_0^2\gamma_1 + k_1^2\gamma_0} \times \left[J_0(\lambda\rho)\, e^{-\gamma_0(z+z')}\, \frac{\lambda}{\gamma_0}\, d\lambda \right] ,$$

$$\rho = \sqrt{(x - x')^2 + (y - y')^2 + a^2} ,$$

$$\phi = \tan^{-1}[(y - y')/(x - x')] ,$$

$$\gamma_0 = \sqrt{\lambda^2 - k_0^2} ,$$

$$\gamma_1 = \sqrt{\lambda^2 - k_1^2} ,$$

where k_0 and k_1 are the propagation constant above and below the interface, respectively.

The presence of the double integral in Eq. (3), particularly the Sommerfeld portion, makes it quite time-consuming and sensitive to evaluate. In spite of that, the basic moment method can be used to solve it, but, in addition to the usual constraints imposed on current sampling, it is necessary to take into account the source distance from the interface.

Series Solution to Sommerfeld Integrals

In the study of antennas over lossy interfaces, the Sommerfeld integrals need a complex integral that has an infinite path of integration. There are three methods to evaluate these integrals. The first procedure is the asymptotic expansion of the integral developed by Norton. [20] In this expansion the fields are written in terms of the inverse powers of the field-point-source-point distance. The asymptotic expansions are accurate only for large field-point-source-point distances. The quasistatic method presented by Baños [1] is an approximation that sets $k_1 = 0$ in the integrand; the modification integrals are then evaluated in closed form. This procedure is supposed to work when the field points and source points are very close, but the accuracy of this method has never been established. The last method is the numerical integration of the Sommerfeld integrals. A numerical code using this procedure has been developed by Lytle and Lager. [21] This procedure gives accurate results for most values of field-point-source-point distance, but is is a very slow numerical procedure.

A general numerical procedure to evaluate the Sommerfeld integral for all values of field-point-source-point distance is discussed in a later section of this report. In this section we present a new series solution that is later used to evaluate the Sommerfeld integral when the source point and field point are near the interface. The fields from a source point and field point on the free-space side of the interface can be written in terms of two integrals:

$$\int_0^{\infty} \frac{1}{\gamma_0 + \gamma_1}\, e^{-\gamma_0 z}\, J_0(\rho\lambda)\, \lambda d\lambda , \tag{4a}$$

and

$$\int_0^{\infty} \frac{1}{k_1^2\gamma_0 + k_0^2\gamma_1}\, e^{-\gamma_0 z}\, J_0(\rho\lambda)\, \lambda d\lambda . \tag{4b}$$

An outline of the procedure to find the series expansion for the former integral is presented below. The development of a new series representation begins by writing $\gamma_0 = (\lambda^2 - k_1^2 + \Psi)^{1/2}$ in

$$\frac{1}{\gamma_0 + \gamma_1}$$

and

$$e^{-\gamma_0 z} ,$$

where $\Psi = k_1^2 - k_0^2$. Then these new terms are expanded by Taylor series in Ψ. The first Taylor series gives

$$\frac{1}{\gamma_0 + \gamma_1} = \sum_{m=0}^{\infty} G_m \left[k_1^2 - k_0^2\right]^m , \tag{5}$$

when the first coefficient $G_0 = 1/2$. The remaining G's can be found by a recursion procedure. Let the n^{th} term be expressible as

$$G_n = (-1)^n \sum_{m=1}^{n} g_m^n ; \tag{6}$$

then the $n+1^{th}$ term is

$$G_{n+1} = (-1)^{n+1} \sum_{m=1}^{n+1} g_m^{n+1} , \tag{7}$$

where

$$g_1^{n+1} = \frac{n + 1}{4(n + 1)} g_1^n \tag{8a}$$

$$g_m^{n+1} = \frac{n + (m - 2)}{2(n + 1)} g_{m-1}^n + \frac{n - (m - 2)}{4(n + 1)} g_m^n ,$$

$$\text{for } m = 2, 3, \ldots, n \tag{8b}$$

$$g_{n+1}^{n+1} = \frac{2n - 1}{2(n + 1)} g_n^n \tag{8c}$$

The first term in the above recursion is

$$g_1^1 = \frac{1}{8} .$$

The Taylor series for the exponential term gives

$$e^{-\gamma_0 z} = e^{-\gamma_1 z} \sum_{m=0}^{\infty} \mathfrak{G}_m \left(k_1^2 - k_0^2\right)^m , \tag{9}$$

where $\mathfrak{G}_0 = 1$. The remaining $\mathfrak{G}$'s can be found by a recursion procedure. Let the n^{th} term be expressed as

$$\mathfrak{G}_n = \sum_{p=1}^{n} g_n^p \frac{z^p}{\gamma_1^{2m-p}} , \tag{10}$$

then the $n+1^{th}$ term is

$$\mathfrak{G}_{n+1} = \sum_{p=1}^{n+1} g_p^{n+1} \frac{z^p}{\gamma_1^{2n-p}} , \tag{11}$$

where

$$g_1^{n+1} = -\frac{2n-1}{2(n+1)} g_1^n , \tag{12a}$$

$$g_p^{n+1} = -\frac{1}{2(n+1)} g_{p-1}^n - \frac{2n-p}{2(n+1)} g_p^n$$

$$\text{for} \begin{cases} p = 2, 3, \ldots, n \\ n = 2, 3, \ldots, n \end{cases} \tag{12b}$$

$$g_{n+1}^{n+1} = -\frac{1}{2(n+1)} g_n^n \tag{12c}$$

The first term in the recursion is

$$g_1^1 = -\frac{1}{2} .$$

The Taylor series represented in Eqs. (5) and (9) are then multiplied together to find a single expansion for the term $e^{-\gamma 0 z}/\gamma_0 + \gamma_0$ in the integrand of Eq. (4a). This new representation of the integrand is an infinite series. When the series and integration are interchanged, the integral in Eq. (4a) can be expressed as

$$\sum_{m=0}^{\infty} {}^{\alpha}D_m \left(k_1^2 - k_0^2\right)^m \ , \tag{13}$$

where

$${}^{\alpha}D_m = \sum_{p=1}^{m+1} D_p^m \ Z^{-1} \ L_{2m+2-p} \ (m=0,1, \ \ldots) \ . \tag{14}$$

The term L_m in Eq. (14) is the integral

$$2\int_0^{\infty} \frac{e^{-\gamma_1 z}}{\gamma_1 m} \ J_0(\lambda p) \ \lambda d\lambda \ . \tag{15}$$

To evaluate the series in Eq. (14), we must first find a method to evaluate the above integrals. To accomplish this we now introduce an operator

$$\Gamma = \frac{1}{k_1} \ \frac{\partial}{\partial k_1} \ .$$

When this operator is used on L_1 and L_2 it can be shown that

$$L_m = \sum_{p=1}^{\frac{m}{2}} H_p^m z^{2(p-1)} \left[\Gamma^{\frac{m}{2}-p} \ L_2\right] - \sum_{p=1}^{\frac{m}{2}-1} K_p^m z^{2p-1} \left[\Gamma^{\frac{m}{2}-p} - L_1\right] \ , \tag{16a}$$

$$L_{m+1} = - \sum_{p=1}^{\frac{m}{2}} H_p^{m+1} z^{2p-1} \left[\Gamma^{\frac{m}{2}-p} \ L_2\right] + \sum_{p=1}^{\frac{m}{2}} K_p^{m+1} z^{2(p-1)} \left[\Gamma^{\frac{m}{2}+1-p} - L_1\right] \ , \tag{16b}$$

where m is an even integer. In the above expression, Γ^m means that the operator Γ is applied m times to L_2 or L_1.

The integral L_1 is

$$L_1 = 2 \ \frac{e^{ik_1(\rho^2+z^2)^{1/2}}}{(\rho^2 + z^2)^{1/2}} \ . \tag{17}$$

By applying the Γ^m operator to L_1, we can show that

$$\mathcal{F}^{n+1}L_1 = 2(-1)^{n+1}\frac{e^{ik_1(\rho^2+z^2)^{1/2}}}{k_1^{2(n+1)}-1}\left\{1\cdot 3\cdot 5\cdots[2(n+1)-3]\right\}\sum_{p=1}^{n+1} I_p^{n+1} \quad . \tag{18}$$

The I's in the above equation can be generated from a recursion relationship.
The first two I's are

$$I_1^1 = (-i)$$

and

$$I_2^2 = (i)^2\left[(k_1\rho)^2 + (k_1 z)^2\right]^{1/2} \quad .$$

The remaining term can be generated for

$$I_1^{n+1} = I_1^n \quad , \tag{19a}$$

$$I_2^{n+1} = I_2^n \quad , \tag{19b}$$

$$I_p^{n+1} = \frac{(-i)\left[(k_1\rho)^2 + (k_1 z)^2\right]^{1/2}}{[2(n+1)-3]} I_{p-1}^n + \frac{[2(n+1)-(2+p)]}{[2(n+1)-3]} I_p^n \quad ,$$

$$\text{for } n \geqslant 3 \text{ and } p = 3, 4, \ldots, n \quad , \tag{19c}$$

$$I_{n+1}^{n+1} = \frac{(-i)\left[(k_1\rho)^2 + (k_1 z)^2\right]^{1/2}}{[2(n+1)-3]} I_n^n \quad . \tag{19d}$$

Now that we have a method to evaluate the $\mathcal{F}^n L_1$, we can turn our attention to the other terms that still need evaluation.

The integral L_2 can be shown to be

$$-2\int_0^z \frac{e^{ik_1(\rho^2+z'^2)^{1/2}}}{(\rho^2+z'^2)^{1/2}}\,dz' + i\pi H_0^{(1)}(k_1\rho) \quad . \tag{20}$$

When the $\mathcal{F}$ operator is applied to the above expression one finds

$$\mathcal{F}^m L_2 = -2\mathcal{F}^m \int_0^z \frac{e^{ik_1 (\rho^2 + z'^2)^{1/2}}}{(\rho^2 + z'^2)^{1/2}} dz' + i(-1)^m \frac{\rho^m}{k_1^m} H_m^{(1)} (k_1 \rho) . \tag{21}$$

The term $H_m^{(1)}$ is the Hankel function of first kind in the order. To find the integer in Eq. (21) we expand the integrand in terms of z' and then perform the integrand analytic. Then $\mathcal{F}^m$ operates on the new series representation for the integral.

NUMERICAL METHODS

In this section we discuss the numerical method used to evaluate Sommerfeld integrals in this study. This approach is unique in that, when the field point and source point are above an interface, all of the electrical field from the Sommerfeld integrals can be written in terms of two-dimensional space. To prove this, we need only look at the Sommerfeld integral

$$\int_0^\infty \frac{1}{\gamma_0 + \gamma_1} e^{-\gamma_0 (z+z')} J_p(\lambda\rho)\lambda d\lambda . \tag{22}$$

where $\rho = \sqrt{(x - x')^2 + (y - y')^2}$. The points (x,y,z) and (x', y', z') are the field point and source points, respectively. All values of the above integral can be described in terms of two variables ρ and $z + z'$. We now introduce a new two-dimensional space in ρ and $z + z'$; it is the solution space for Sommerfeld integrals. The solution space is shown in Fig. 2.

In the framework of the solution space we must now evaluate the Sommerfeld integrals. When the point in the solution space is described by $1.0 \leq \rho/\lambda_0$ or $1.0 \leq z + z'/\lambda_0$ the asymptotic series developed by Norton [20] is used to evaluate the fields. The asymptotic series is an expansion in inverse powers of the field-point-source-point distance; therefore, it provides a good method to evaluate the integrals when the distances are large. The asymptotic methods do not work well when the field point and source point are less than one wavelength. Figure 2 depicts the region in the solution space where the asymptotic method is used to evaluate the Sommerfeld integrals.

To gain some insight into the method used for evaluating the Sommerfeld integrals in other regions of the solution space, we evaluated the various components of the electric field for the horizontal and vertical dipoles in the solution space. The evaluation of the Sommerfeld integrals was obtained by using a code developed by Lytle and Lager [21] that performs the integration numerically. A three-dimensional plot in the solution space of the real-part of the electrical field produced by a vertical dipole is shown in Fig. 3, which plots the value of the function in terms of p, $z + z'$. The observation that the electric field value plotted in Fig. 3 is rather well-behaved, except near the origin, led us to a procedure known as the "bivariate interpolation of the electrical fields." This procedure begins with division of the solution space into a set of rectangular grids. The electrical field for a given f, ϵ_r, and σ is found at each grid point in the solution space prior to evaluating a given antenna. When the moment-method code needs a field value not on the grid, a four-point bivariate interpolation is used to evaluate the field from the four known field values at the corners of the grid. This procedure is outlined in Fig. 4. To demonstrate the accuracy of this approach, we show in Fig. 5 a three-dimensional plot of the error function when the bivariate interpolation is used to find the electrical field plotted in Fig. 3. In this test, a grid-spacing of 0.5λ produced a 10% agreement. In general, smaller grid spacing produces better agreement.

The bivariate interpolation of the electrical fields provides good answers in the solution space for values of ρ and $z + z'$ in the two regions where [$0.1 \leq \rho/\lambda_0 \leq 1.0$ and $0 \leq z + z'/\lambda_0 \leq 1$] and [$0 \leq \rho/\lambda_0 \leq 0.1$ and $0.1 \leq z + z'/\lambda_0 \leq 1.0$]. The size of the grids used in this calculation is shown in Fig. 6. Bivariate interpolation requires a computation time of about 100 μs on a CDC 7600 for a single set of field values, while the code that numerically integrates the Sommerfeld integrals correspondingly requires 0.1 s. (Note that after the solution-space grid has been evaluated for given f, ϵ_r, and σ, these values can be saved for future use; they are independent of the type of antenna studied.) The electric field determined from the Sommerfeld integrals has singularities when both $\rho = 0$ and $z + z' = 0$. The series representation of the Sommerfeld integrals discussed earlier isolates these singularities. Therefore, the series representation is used to evaluate the field near the

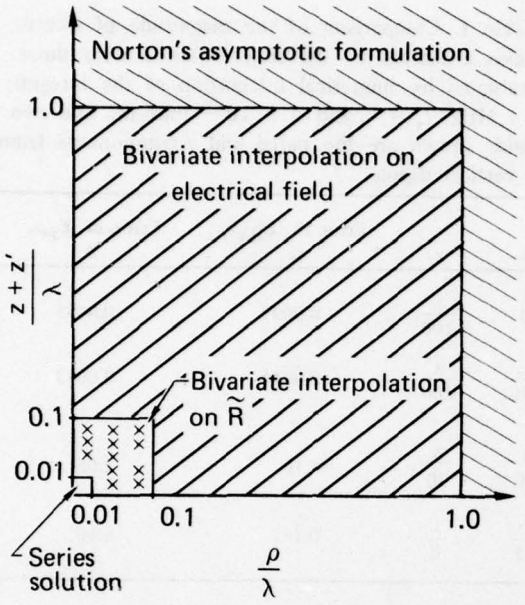

Fig. 2. Two-dimensional solution space used to evaluate the Sommerfeld integrals. The various methods of evaluating the integrals and their usable regions are also shown.

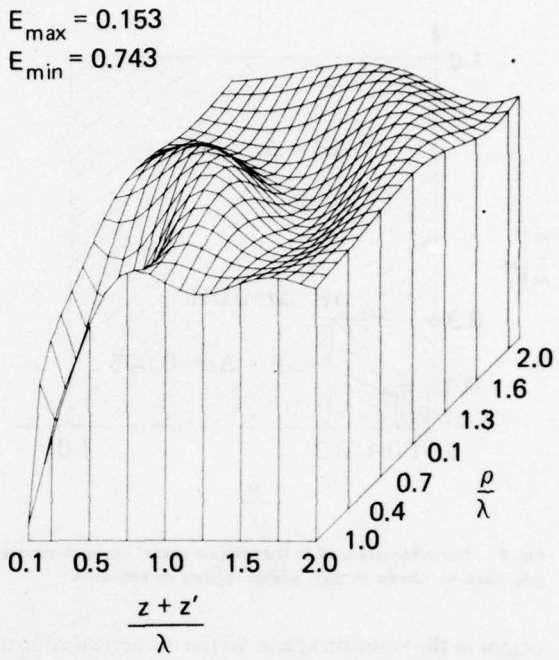

Fig. 3. Three-dimensional aspect plot of Sommerfeld-integral portion of radial electric field for vertical dipole. The real part of the electric field is plotted on the vertical axis as a function of $z + z'$ and ρ. The electric parameters are f = 10 MHz, $\epsilon_r = 9.0$, $\sigma = 10^{-2}$ mho/m, $0.1\lambda \leq \rho \leq 2.0\lambda$, and $0.1\lambda \leq (z + z') \leq 2.0\lambda$. The maximum and minimum field values are also shown.

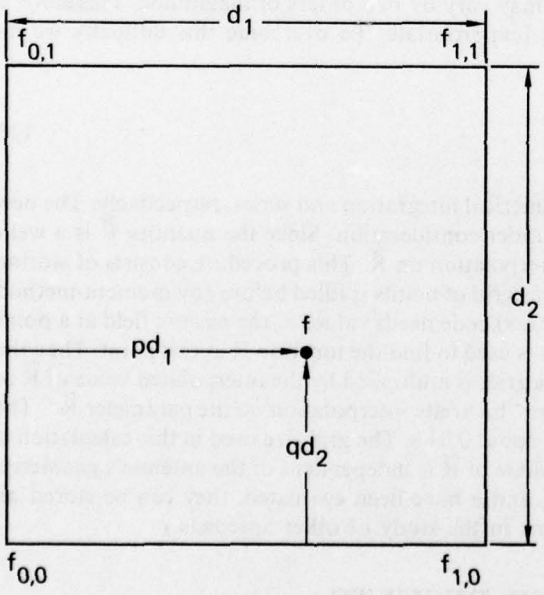

Fig. 4. The four-point, bivariate interpolation procedure. The function f is found in terms of its four known end-point values $f_{0,0}$, $f_{1,0}$, $f_{0,1}$, and $f_{1,1}$. $f = (1 - p)(1 - q)f_{0,0} + p(1 - q)f_{1,0} + q(1 - p)f_{0,1} + pqf_{1,1}$.

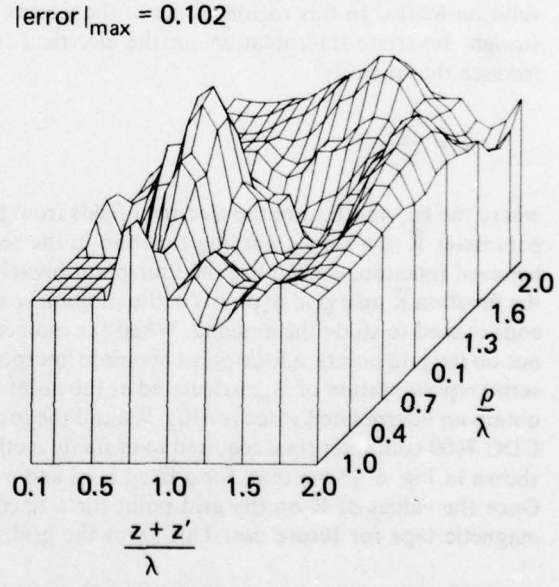

Fig. 5. Aspect plot of difference between the Sommerfeld-integral field values and interpolated values for real part of radial electric field of vertical electric dipole. The electric parameters are the same as those in Fig. 3. The separation between interpolation grid points is 0.5 λ. The interpolation was performed for the region defined by $0.1\lambda \leq (z + z') \leq 2.0\lambda$, excluding the small region $0.1\lambda \leq \rho \leq 0.5\lambda$ and $0.1\lambda \leq (z + z') \leq 0.5\lambda$.

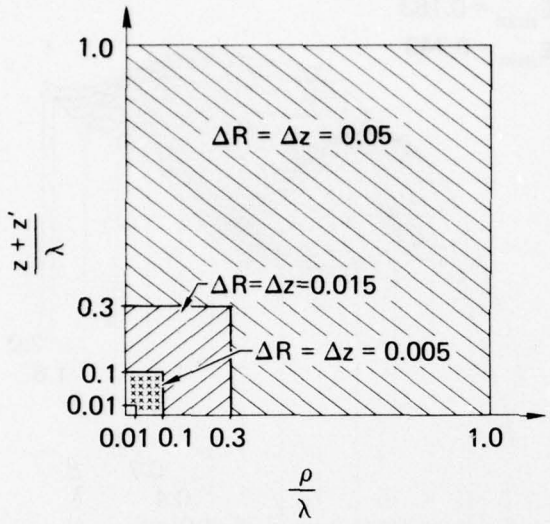

Fig. 6. The grid sizes used in the solution space. The appropriate grid sizes are shown in their usable regions as indicated.

Table 1. Comparison of the magnitude of electric fields evaluated by the series solution with those evaluated by numerical integration of the integral; f = MHz, $\epsilon_r = 9$, and $\sigma = 10^{-3}$ mho/m. The two fields shown are the radial and z-components from a vertical dipole.

ρ	z	Error in $\lvert E_{RV}\rvert$, %	Error in $\lvert E_{zv}\rvert$, %
0	$\frac{\lambda}{100}$	0.0099	0.0455
$\frac{\lambda}{100}$	$\frac{\lambda}{100}$	0.0944	0.0043
$\frac{\lambda}{30}$	$\frac{\lambda}{30}$	4.16	2.05
$\frac{\lambda}{15}$	$\frac{\lambda}{0}$	0.162	6.60

origin in the solution space. In the numerical code used to evaluate this field, the first ten series terms are used. Table 1 shows a comparison of electrical field magnitudes evaluated by the series method with those generated by numerical integration. From Table 1, it is obvious that the series solution works only when $0 \leqslant \rho/\lambda_0 \leqslant 0.01$ and $0 \leqslant z + z'/\lambda_0 \leqslant 0.01$. The CDC 7600 computer time required to evaluate the series is about 0.01 s while the numerical integration requires 0.1 s. The region in the solution space occupied by the series solution is shown in Fig. 2.

As Fig. 2 shows, a region exists where no reliable method is available to evaluate the Sommerfeld integral. It lies between the regions where the bivariate interpolation on the electrical field works and where the series solution works. In this region, some of the electric field may vary by two orders of magnitude. Therefore, a straight bivariate interpolation on the electrical field is inappropriate. To overcome this difficulty we introduce the quantity

$$\tilde{R} = \frac{E_{ex}}{E_{se}} , \tag{23}$$

where the E_{ex} and E_{se} are the electrical fields from the numerical integration and series, respectively. The new parameter $\tilde{R}$ is a slowly varying function in the region under consideration. Since the quantity $\tilde{R}$ is a well-behaved function, we can use the four-point bivariate interpolation on $\tilde{R}$. This procedure consists of storing the function $\tilde{R}$ on a grid of points in the solution space. This grid of points is filled before any moment-method code is used to study the antenna. When the moment-method code needs values of the electric field at a point not on the grid points, a four-point bivariate interpolation is used to find the function $\tilde{R}$ at this point. Then the series representation of E_{se}, calculated at the point off the grid, is multiplied by the interpolated value of $\tilde{R}$ to obtain an interpolated value for E_{ex}. We call the procedure "bivariate interpolation on the parameter $\tilde{R}$." The CDC 7600 computer time required to evaluate method is about 0.01 s. The grid size used in this calculation is shown in Fig. 6. (Note that, for a fixed f, ϵ_r, and σ, the value of $\tilde{R}$ is independent of the antenna's geometry. Once the values of $\tilde{R}$ on the grid point for a fixed f, ϵ_r, and σ have been evaluated, they can be stored on magnetic tape for future use. This saves the grid fill time in the study of other antennas.)

TEST CASES AND RESULTS

Three types of calculations are summarized in this section. The first type involves test cases to assess operation of the overall program; it is intended to provide a check on numerical accuracy. The second, by contrast, is intended to obtain some preliminary results prior to performing parametric calculations on the antennas of interest, which are covered in the third section.

Test Cases

One of the greatest uncertainties associated with using a new computer model is validating its results. Thus, much of our attention during the early stages of this work was focused on test calculations to check the Sommerfeld-integral routine, the interpolation procedure, and the overall computation itself. Calculations pertaining to the first two cases are reported in the previous section. Here we discuss results obtained in connection with the overall computational accuracy.

Ideally, experimental results provide probably the best and most convincing data for use in validating a computer model. Realistically, however, such data are neither extensive nor readily available; those that are obtainable are of limited scope and uncertain applicability. Therefore, while our ultimate goal remains that of validating the computer model using experimental data, the test cases presented here are, instead, of a numerical nature.

Several kinds of numerical tests might be performed to check the computer model's accuracy. One of the more obvious is simply to examine the trend of the numerical results for obviously incorrect behavior as a function of the various parameters. An example of this is shown in the preceding section, where the interpolated fields are found to exhibit anomalous behavior along the $z + z' = 0$ and $\rho = 0$ lines. This kind of test may be regarded generally as a necessary, but not sufficient, condition to be met by a valid calculation. It can be especially useful in the preliminary stages of code development or as a diagnostic when judgmentally invalid results are obtained as the overall computational output.

Another useful numerical test is to compare results from the new code with those obtained from the earlier Lawrence Livermore Laboratory (LLL) Sommerfeld code, which did not use interpolation. This was done for several cases, for example, horizontal dipole and Beverage antennas. SOMINT produced results that generally are numerically indistinguishable from these alternate calculations at LLL, [21] as shown in Figs. 7-10.

Numerical tests can also be based on limiting cases of the associated parameters where the answers are known analytically. For example, when the relative permittivity and conductivity of the ground approach their free-space values, the antenna current should be independent of height above the interface. The Sommerfeld-integral fields must then also exactly cancel the perfect-ground image fields, so that only the free-space contributions remain. It is convenient to check this by examining the input impedance of an antenna as it is lowered towards the now fictitious interface. Results obtained from this kind of calculation are shown in Fig. 11. Such tests proved very useful in correcting numerical inconsistencies originally present in the program, especially those that were important only where $z + z' \to 0$.

Preliminary Results

Antennas operated in the HF range and located near the earth's surface generally are excited and/or terminated with respect to ground potential. This may be accomplished in several ways; for example, a ground stake, counterpoise, ground screen, or ground-return wire may be used. The first two methods involve wires that penetrate the interface, the treatment of which is somewhat uncertain. In addition, modeling them requires computing the fields transmitted across the interface, to which the interpolation procedure developed here does not directly apply.

Our approach has thus been to concentrate performing computations for antenna models whose wires lie entirely on the free-space side of the interface. Given this constraint, we can model configurations which incorporate ground-return wires or ground screens so long as their height h above the ground equals or exceeds that previously shown to be necessary (Fig. 11). As observed in connection with Fig. 11, the minimum height for valid results ($\lesssim 3 \times 10^{-4} \lambda_0$) is small enough that, for practical purposes, the wires are at the interface.*

One other situation can also be modeled (albeit only approximately): the ground stake excitation/termination mode. In this case, the antenna wire is terminated at the interface and the effect of the ground stake is approximated in two ways. First, the current at the end of the wire is constrained to have zero slope, a condition rigorously correct only for a perfect ground, but a behavior approximately simulated by an actual ground stake. Second, the fields due to the ground-stake current are ignored.

*Besides the limit imposed by Sommerfeld-field accuracy, there is also a minimum-height limit due to the thin-wire approximation. This implies that for $h \lesssim 10a$, the problem must be reformulated if questionable results are to be avoided. Of course, if a bare wire is lowered to $h = a$ and thus comes into contact with a possibly lossy ground, still further reformulation is required to account for their ohmic contact. These aspects of the problem are beyond the scope of the present work.

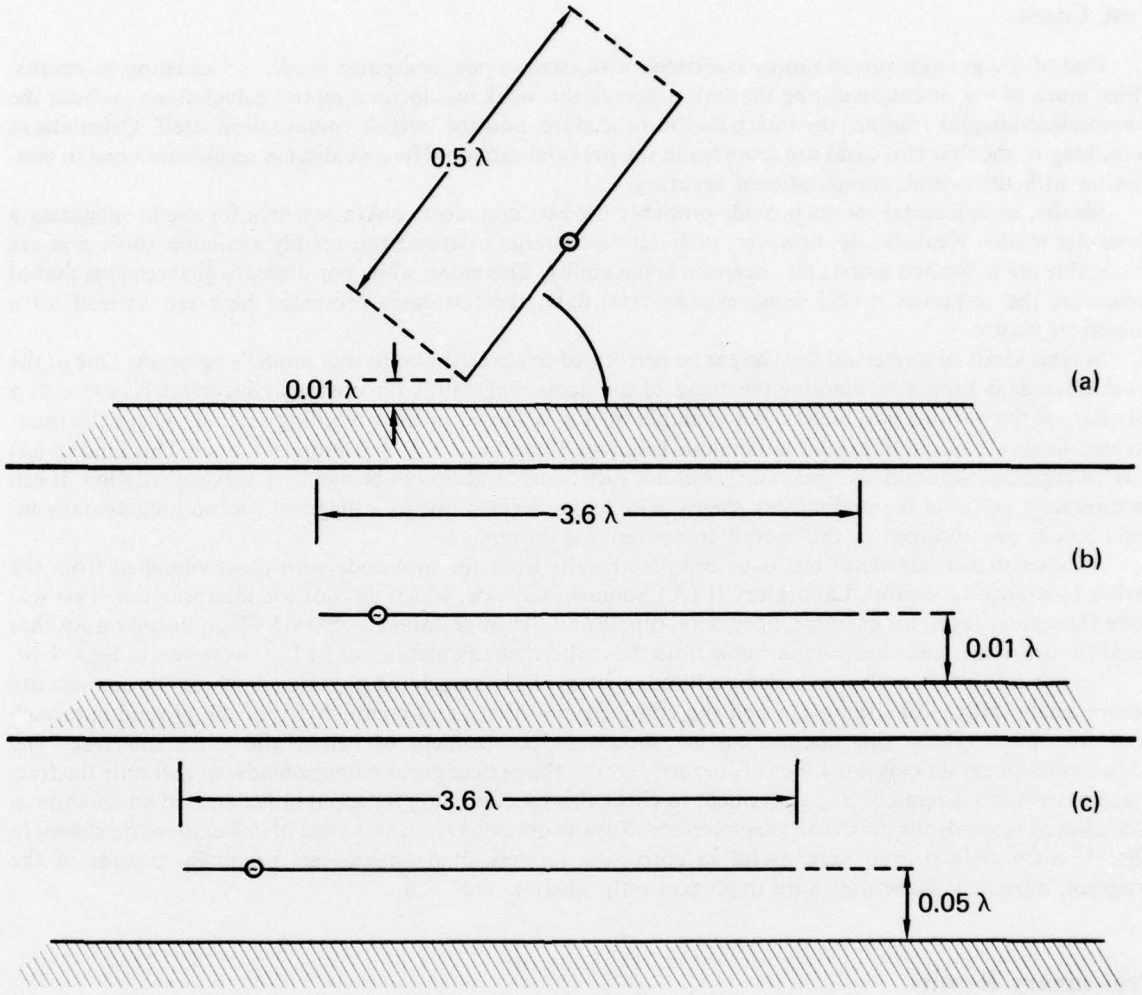

Fig. 7. Three antennas used to compare the numerical performance of the interpolation approach with the orginial Sommerfeld mode: (a) slanted dipole above interface; (b) horizontal wire 0.01 λ above interface loaded near the end; (c) horizontal wire 0.05 λ above interface loaded near the end. The current distributions are presented in the following figures. Small differences are observable between results obtained from the two approaches, but the basic behavior is the same.

We performed calculations pertaining to these issues for monopole and vertical half-rhombic antennas. Some of the results are presented in Figs. 12-22. Based on the outcome of these preliminary calculations, we chose the ground-stake approximation to model the grounded ends of the antennas selected for parametric study. At this point of development in the program, it represents the least certain element in the calculations.

Parametric Results

We performed parametric calculations to evaluate ground-screen effects and to characterize two antenna types, the slanted V and vertical half-rhombic. The results obtained are summarized below.

Ground-Screen Effects

Ground screens can provide a terminal against which to drive or terminate an antenna. More importantly, they can provide impedance and pattern control. Impedance is controlled when variations due to changes in local ground conditions can be reduced or eliminated, permitting the feedpoint current to become a function of the screen parameters. Pattern control is possible because the ground-screen currents add their

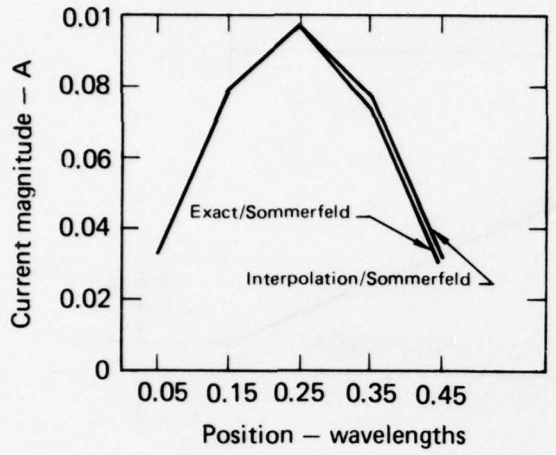

Fig. 8. Magnitude of the current on the antenna shown in Fig. 7a. The interpolation solution to the problem is compared to the exact solution. The electrical parameters are f = 10 MHz, $\sigma = 10^{-2}$ mho/m, and $\epsilon_r = 9$.

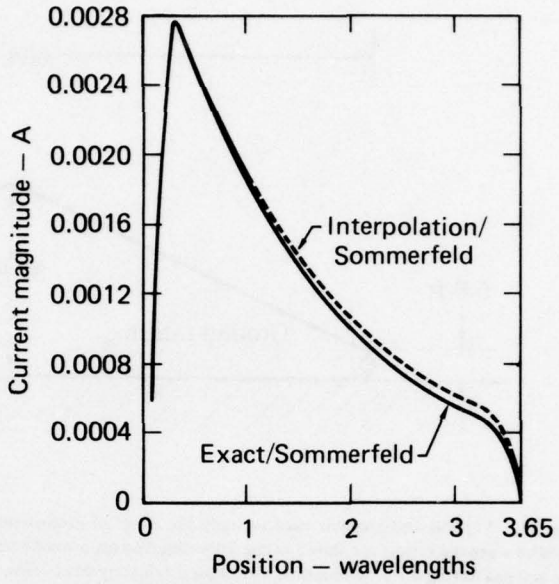

Fig. 9. Magnitude of the current on the antenna shown in Fig. 7b. The interpolation solution to the problem is compared to the exact solution. The electrical parameters are f = 10 MHz, $\sigma = 10^{-2}$ mho/m, and $\epsilon_r = 9$.

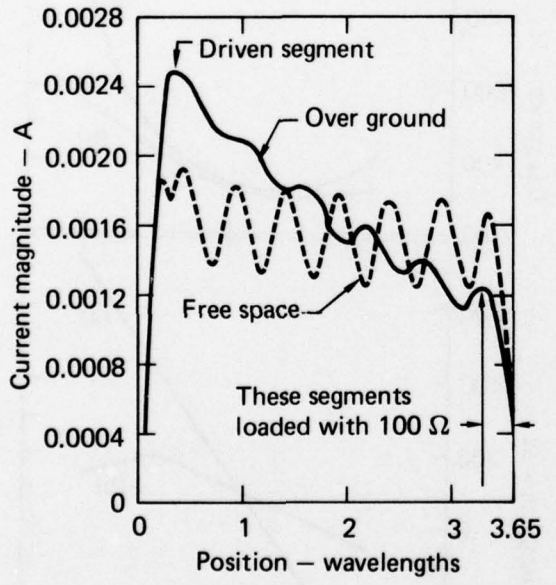

Fig. 10. Magnitude of the current on the antenna shown in Fig. 7c. The interpolation solution to the problem is compared with the exact solution. The electrical parameters are f = 10 MHz, $\sigma = 10^{-2}$ mho/m, and $\epsilon_r = 9$. Note that the two solutions are indistinguishable. In order to demonstrate the effect of the ground the results from the same antenna in free space are also presented.

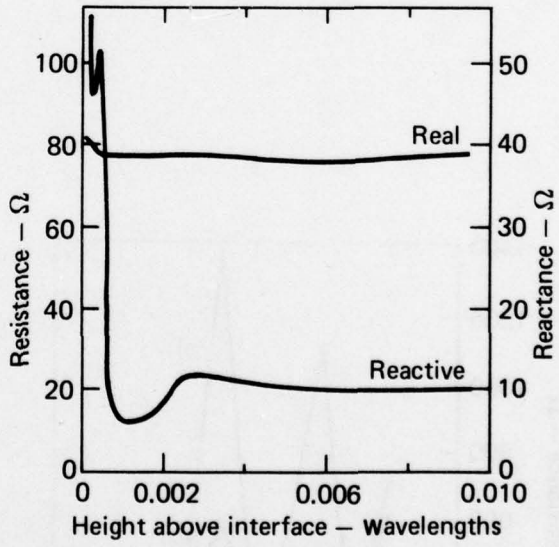

Fig. 11. The Sommerfeld intergral fields must exactly cancel the perfect-ground image fields when the lower half-space has the same properties as the upper half-space, thus providing a good check on the numerical results. Results are presented here for the case where a half-wave horizontal dipole at a frequency of 13 MHz is lowered toward such a pseudo-half-space to check the Sommerfeld integral and interpolation portions of the program. The input impedance is seen to be effectively independent of height to within 0.003 wavelengths, demonstrating the consistency of the overall numerical treatment.

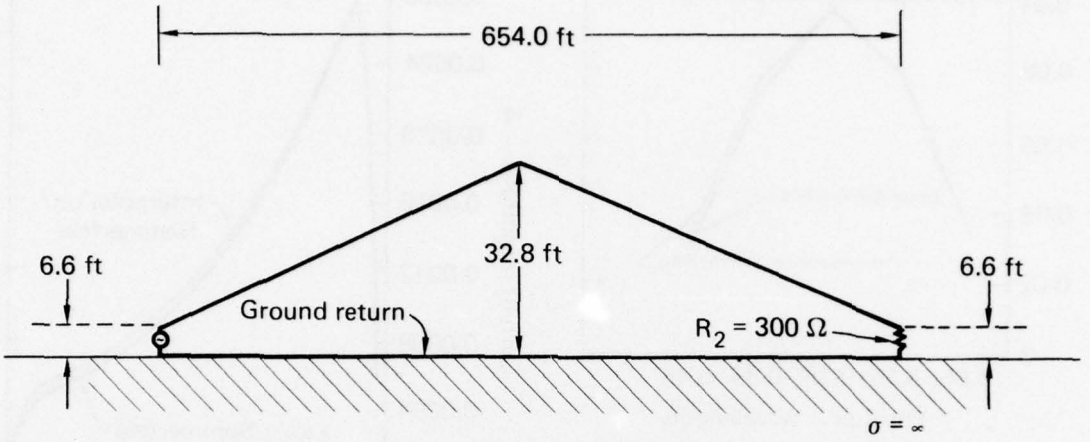

Fig. 12. Vertical half-rhombic used to study the effect of ground returns. (The input impedance behavior over a perfect ground with and without a ground return are shown in the following figures, ground return wire on interface.) The impedance variations are much greater for the antenna having the ground-return wire. This is evidently due to return wire and its image acting as a transmission line to transform the open circuit (with respect to ground) at the termination end to a frequency-dependent load at the input. It might be expected that over a lossy ground, this effect would be much reduced. We have not been able to examine that possibility in this study, but it is a topic that should be pursued further, because of the practical implications and to establish more definitively the limitations of the numerical model.

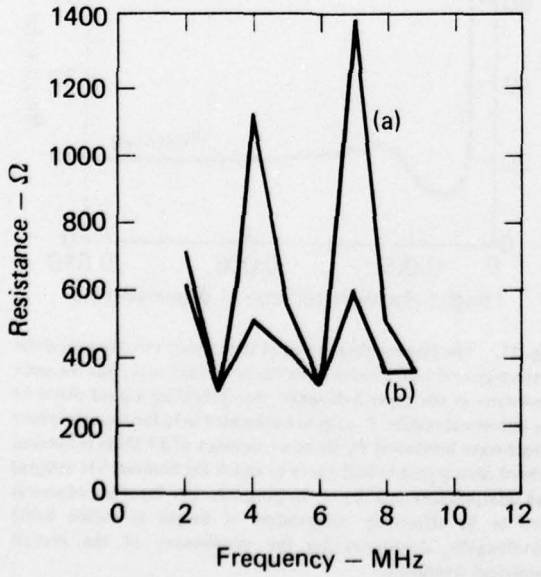

Fig. 13. Input resistance for antenna shown in Fig. 12. One set of data (a) has a ground-return wire and the other set (b) does not.

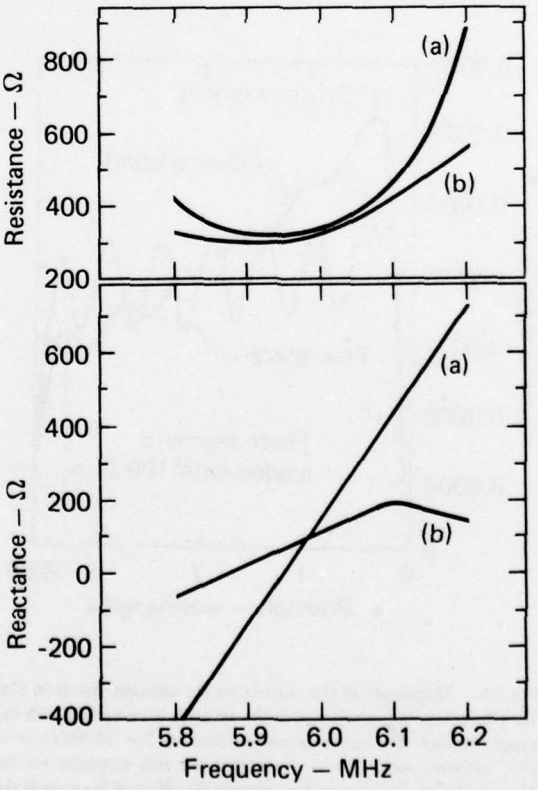

Fig. 14. Input impedance for the antenna shown in Fig. 12, on an expanded frequency scale. One set of data (a) has a ground-return wire and the other set (b) does not.

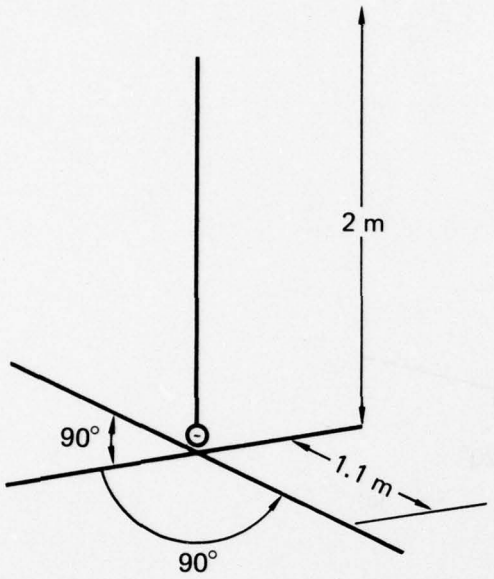

Fig. 15. Several sets of calculations were performed at 13 MHz for a monopole antenna having various ground arrangements. The antenna and four wire grounds are shown above. The input impedance of the antenna was studied as a function of frequency in free space and as a function of height over a perfect ground. These results are shown in the following figures. Its resistance is seen to vary smoothly with height between a free-space value of about 1.55 Ω and asymptotic value near ground of 3.20 Ω. For comparison, the resistance of the same monopole without counterpoise wires and driven against ground is 3.14 Ω.

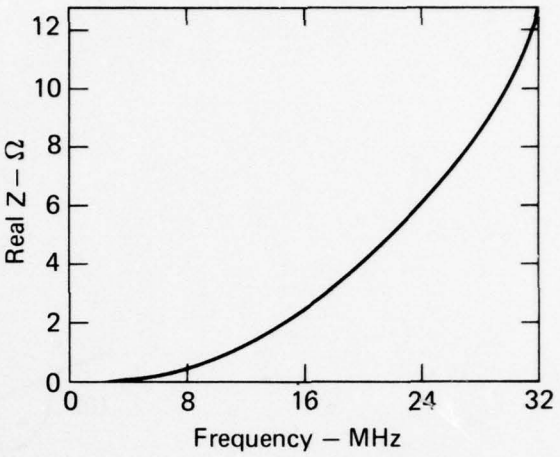

Fig. 16. Input resistance of the antenna shown in Fig. 15 in free space.

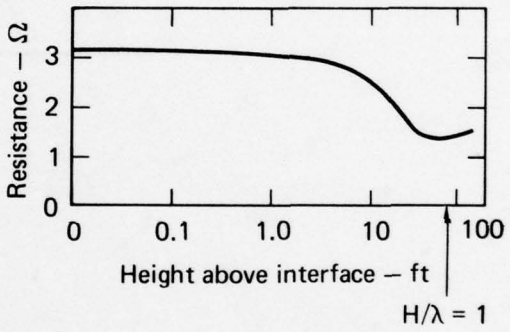

Fig. 18. Input resistance of the antenna shown in Fig. 15 as a function of the height above a perfect ground.

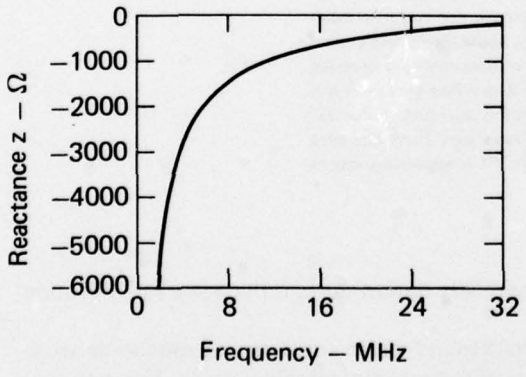

Fig. 17. Input reactance of the antenna shown in Fig. 15 in free space.

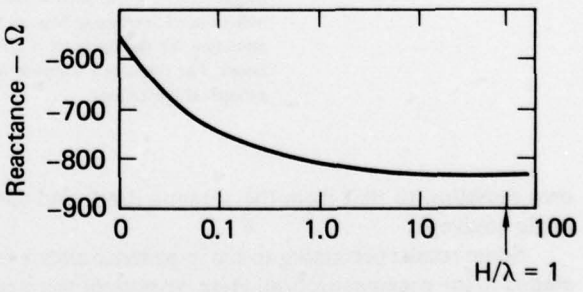

Fig. 19. Input reactance of the antenna shown in Fig. 15 as a function of the height above a perfect ground.

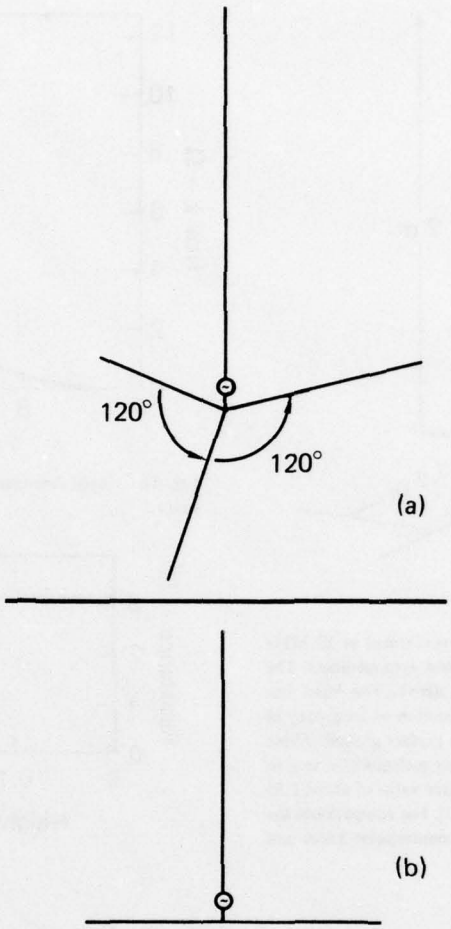

Fig. 20. Monopole antenna with (a) three-wire and (b) two-wire counterpoise. The inputs for the four-, three-, and two-wire counterpoise are plotted as a function of height above the perfect ground in the following figures. The increase in resistance with decreasing height relative to the perfect ground case with a four-wire system is indicative of increasing loss as the ground is approached. No explanation for the bump at ~2 ft in the resistance curve has been found. The resistance decrease below ~0.3 ft is apparently due to numerical limitations.

own radiation to that from the antenna itself, and can be especially important in influencing low-elevation-angle coverage.

Some results pertaining to the impedance effects of a radial ground screen and a vertical monopole are included in the previous section. Here we present some examples of pattern-control calculations. The antenna is again a vertical monopole, with the ground-screen wires. The system was driven at the points between the antenna and screen. Calculations were performed with two-wire ground systems as a function of ground-wire length and angles between the ground wires. Note that the presence of the ground wires greatly enhances the radiation in a direction away from the ground wire (see Figs. 23-25).

This problem in particular was explored to demonstrate the feasibility of using our approach to evaluate ground screen influence on pattern behavior, and not as an extensive parametric excerise *per se*. (It should be noted that a computational capability to do this has not heretofore existed.) While recognizing that more aspects of pattern behavior deserve attention (e.g., although we present here only azimuthal pattern results, the elevation behavior is at least of equal importance), we believe those results are indicative both that the

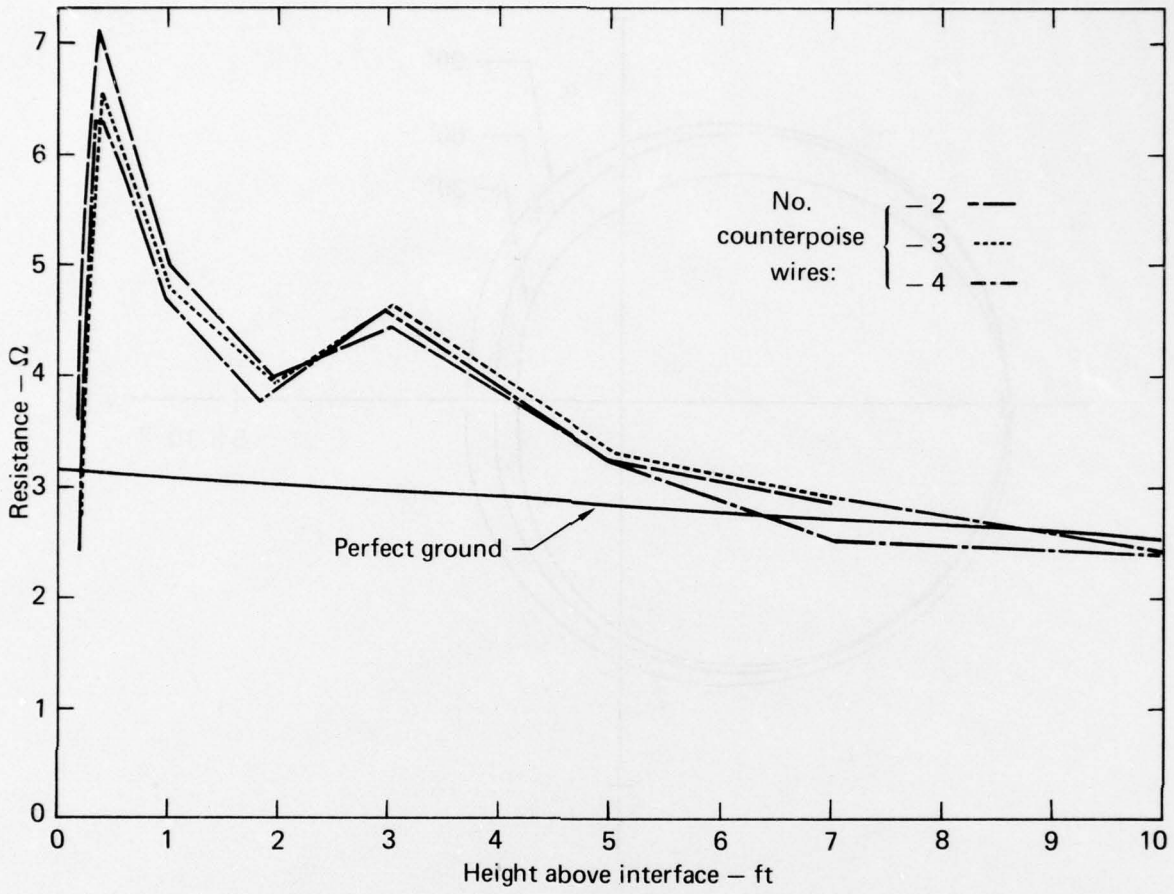

Fig. 21. Input reistance as a function of height above a conducting ground for the antennas in Figs. 15 and 20. The electrical parameters are f = 13 MHz, $\sigma = 10^{-3}$ mho/m, and $\epsilon_r = 9.0$. The data for a monopole on a perfectly conducting ground are also shown.

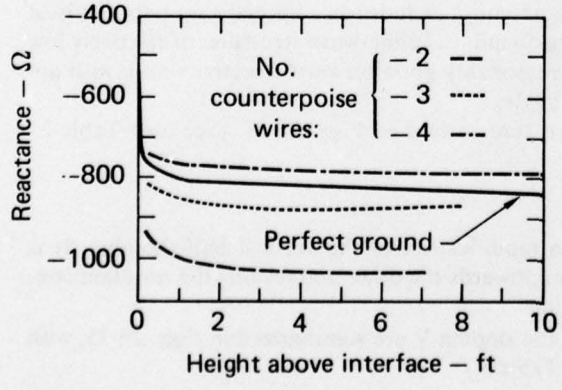

Fig. 22. Input reactance as a function of height above a conducting ground for the antennas given in Fig. 21.

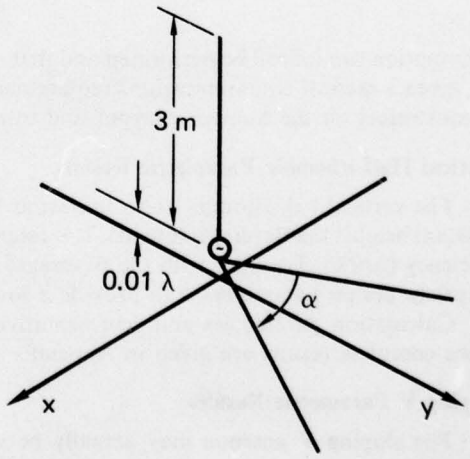

Fig. 23. Vertical monopole antenna with a two-wire horizontal ground screen above a lossy half-space. The two horizontal elements are connected to the base of the monopole. The electrical parameters are f = 10 MHz, $\sigma = 10^{-3}$ mho/m, and $\epsilon_r = 4$. The radiation patterns are shown in Figs. 24 and 25. Note that the wires enhance the radiation very significantly. This increased radiation is in the direction opposite to the ground wires.

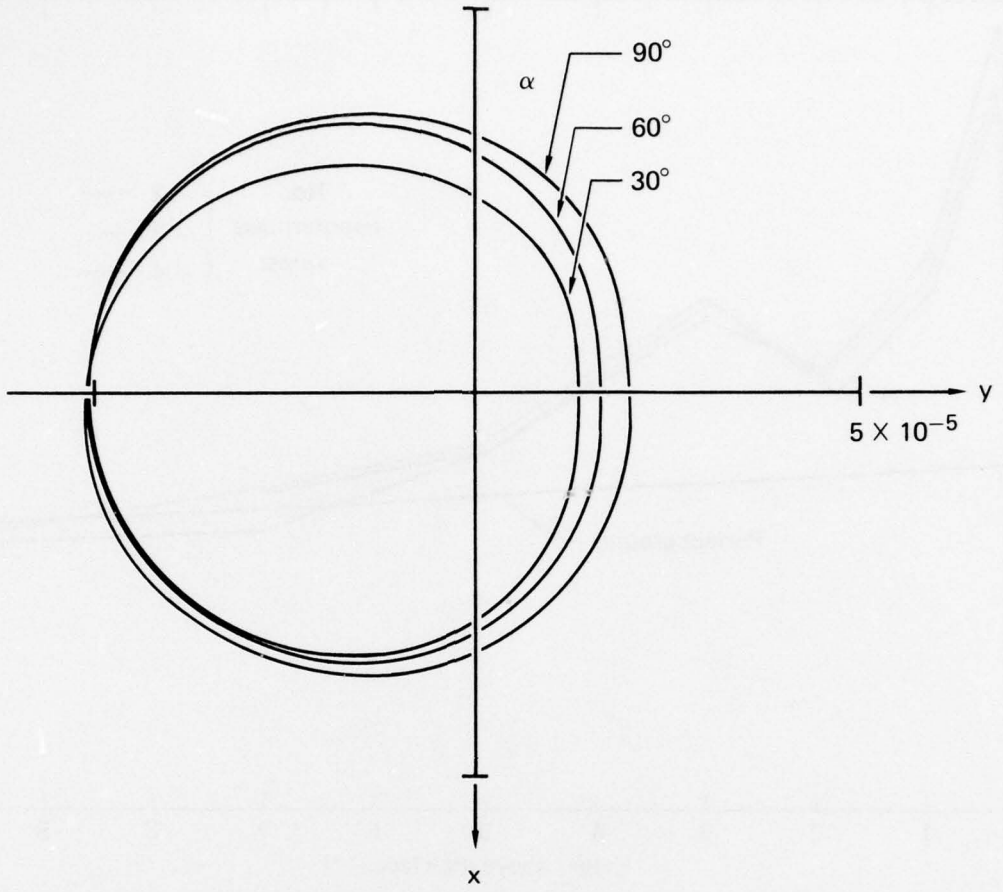

Fig. 24. Azimuthal radiation patterns at 45° elevation angle for the antenna shown in Fig. 23, when the screen-wire length is 3 m. These data are the theta component of the electric field and the angle α is a parameter as shown.

computation can indeed be performed and that it provides invaluable guidance for antenna design. For example, given a tactical communications requirement, an approach like this could optimize performance subject to constraints on the numbers, layout and total ground-wire length, antenna height and geometry, etc.

Vertical Half-Rhombic Parametric Results

The vertical half-rhombic (also known as the lambda antenna) includes as a special case (when it is of constant height) the Beverage antenna. It is essentially a broadband, traveling-wave structure, of relatively low efficiency ($\lesssim$10%). Together with the Beverage, it exhibits reasonably good forward directivity and, with appropriate design parameters, can provide a low take-off angle.

Calculation parameters and representative results are summarized in Figs. 26-28. (See also Table 2.) More complete results are given in Appendix A.

Sloping V Parametric Results

The sloping V antenna may actually be viewed as a modification of the vertical half-rhombic. It is derivable from the latter by rotating one arm of the antenna towards the other and feeding the resultant configuration at its apex rather than at one ground connection.

Calculation parameters and representative results for the sloping V are summarized in Figs. 29-35, with more complete data presented in Appendix B. (See also Table 3.)

A thorough comparison of the sloping V and vertical half-rhombic antennas is impractical with the limited amount of data available from these calculations. We can observe, however, that for equal wire lengths

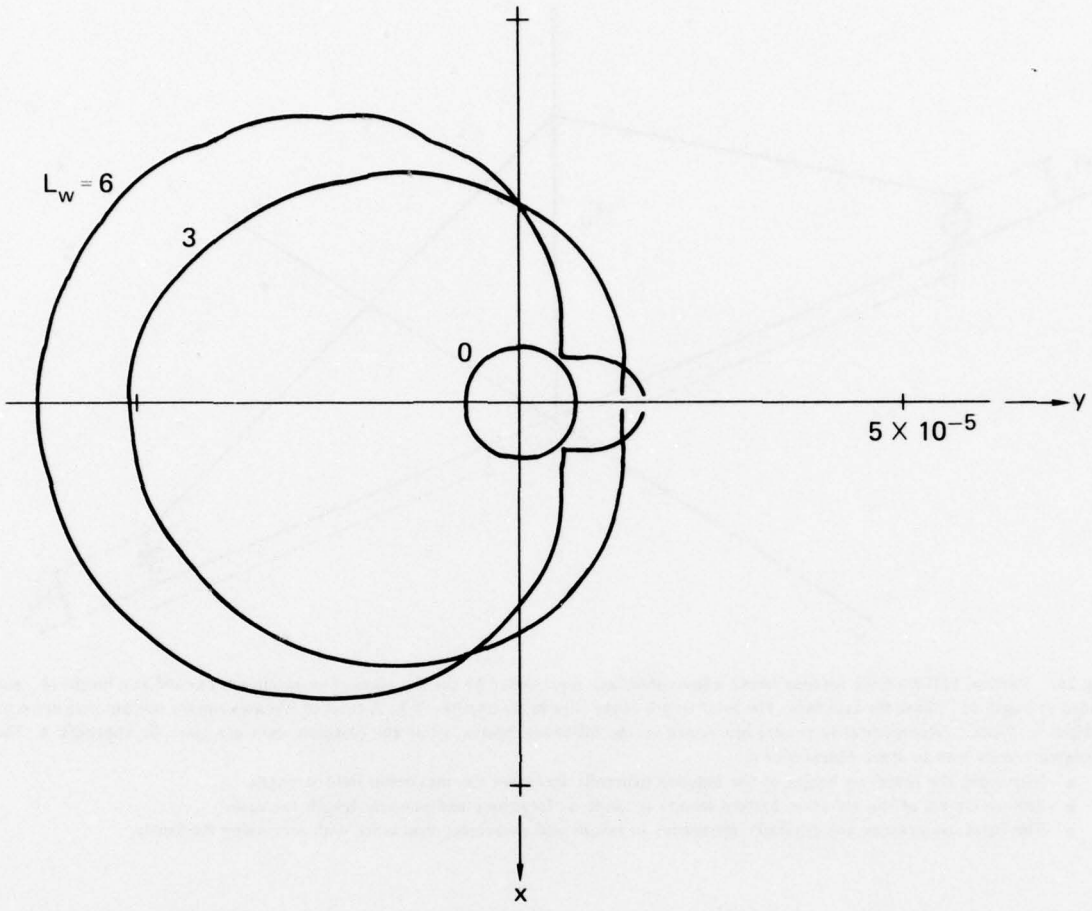

Fig. 25. Azimuthal radiation patterns at 45° elevation angle for antennas in Fig. 23, when the angle between the two ground wires is 60°. These data are the theta component of the electric field with the length of the ground wires a parameter.

and frequencies the vertical half-rhombic produces a maximum field strength roughly twice that of the sloping V. The location of their elevation pattern maxima are relatively similar. Furthermore, the vertical half-rhombic typically has a lower input resistance.

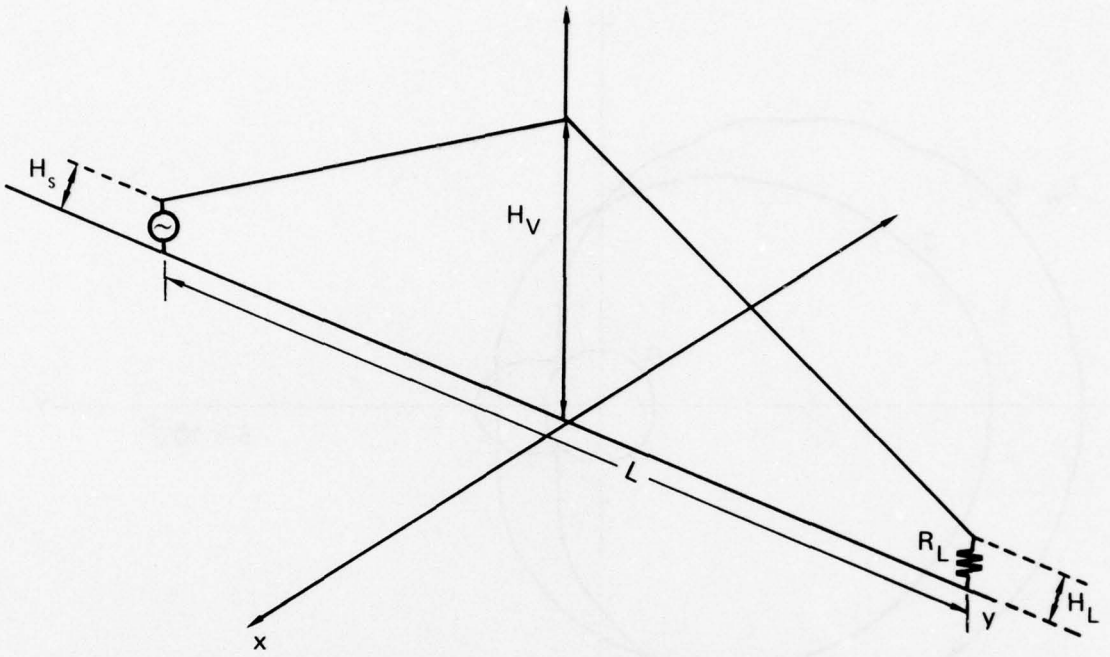

Fig. 26. Vertical half-rhombic antenna above a lossy interface represented by the x-y plane. The antenna is excited at a height H_S and loaded at height H_L above the interface. The total length of the wire in the antenna is L. A total of 33 cases run for this antenna are summarized in Table 2. Representative results are shown on the following figures, while the complete data are given in Appendix A. The tabulated results lead to three observations:

- Increasing the length or height of the antenna generally increases the maximum field strength.
- The maximum of the elevation pattern lowers in angle as frequency and antenna length increase.
- The input impedances are generally insensitive to height and decreasing reactance with increasing frequency.

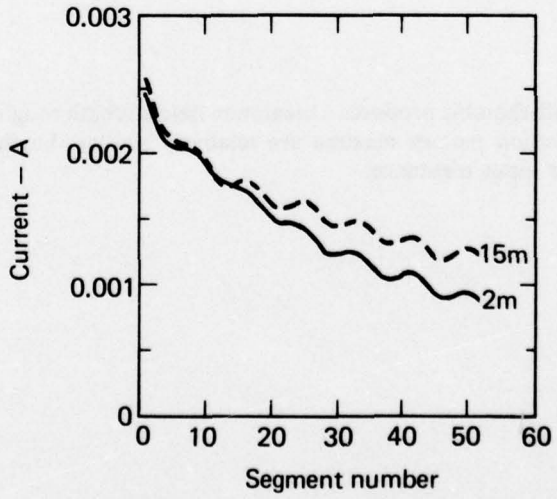

Fig. 27. Comparison of current magnitude on the vertical half-rhombic antenna shown in Fig. 26, when $H_S = 2.0$ m $= H_L$, $R_L = 300\ \Omega$, L = 100 m, f = 10 MHz, $\sigma = 10^{-3}$ mho/m, and $\epsilon_r = 4.0$ for 1-W input. The height H_V is marked by each curve.

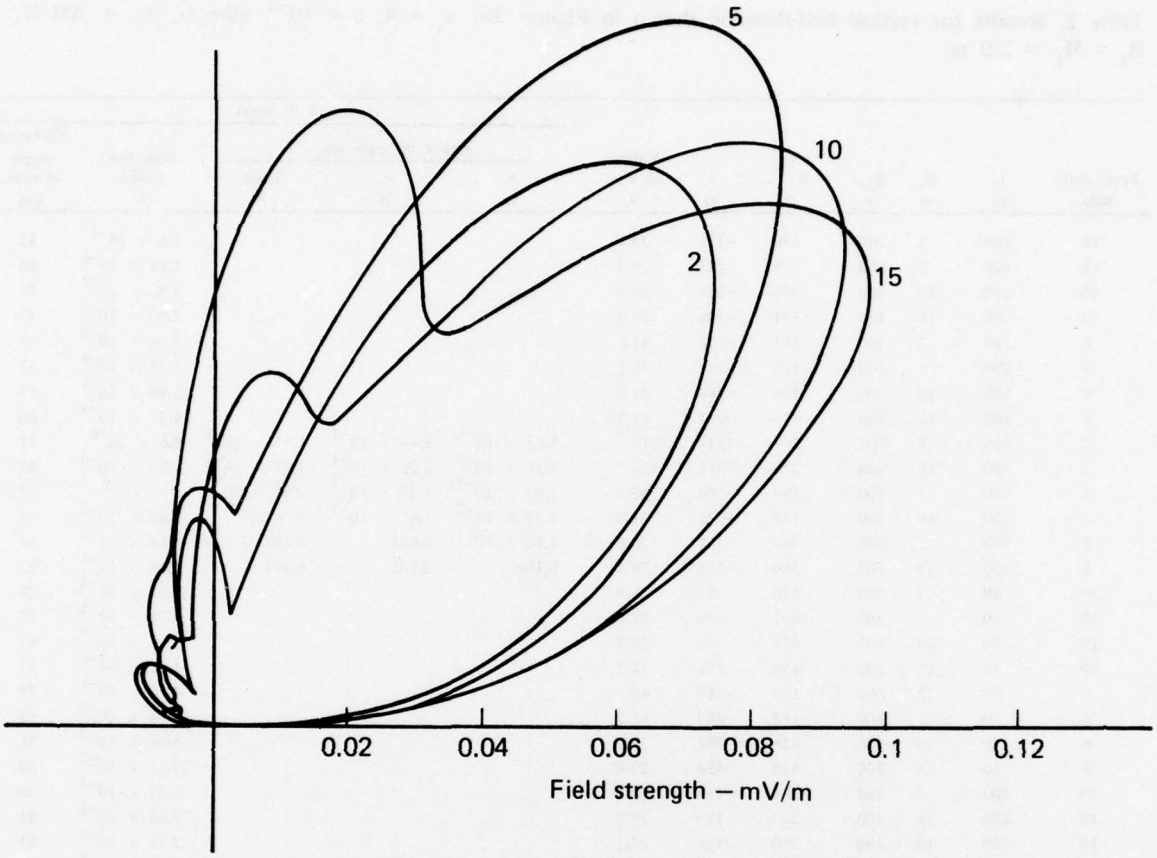

Fig. 28. Plot of the radiation pattern in the plane containing the antenna for the same antenna and electrical parameters used in Fig. 27. The height H_v is marked by each curve.

Table 2. Results for vertical half-rhombic shown in Figure 26; $\epsilon_r = 4$, $\sigma = 10^{-3}$ mho/m, $R_L = 300\ \Omega$, $H_S = H_L = 2.0$ m.

							For 1 W input				
							Power in space wave				
Frequency, MHz	L, m	H_v m	R_L, Ω	Z_{in} R, Ω	I, Ω	Voltage at 1 W, V	θ, W	φ, W	Total, W	Max field (RIEI), V	Elevation angle of max, deg
10	100	2	300	386	−121	29.1				1.4×10^{-4}	33
10	100	5	300	389	−125	29.3				1.64×10^{-4}	36
10	100	10	300	384	−129	29.2				1.88×10^{-4}	37
10	100	15	300	374	−126	28.9				1.90×10^{-4}	37
6	100	2	300	317	−240	31.6				1.04×10^{-4}	57
6	100	5	300	315	−242	31.7				1.21×10^{-4}	57
6	100	10	300	316	−244	31.8				1.40×10^{-4}	59
6	100	15	300	313	−247	31.9				1.45×10^{-4}	60
2	100	5	300	277	−1320	115	9.85×10^{-4}	5.46×10^{-4}	1.53×10^{-3}	6.6×10^{-6}	55
2	100	10	300	276	−1340	116	1.34×10^{-3}	6.26×10^{-4}	1.97×10^{-3}	7.39×10^{-6}	49
4	100	5	300	194	−566	60.7	1.03×10^{-2}	1.27×10^{-2}	2.31×10^{-2}	3×10^{-5}	82
4	100	10	300	195	−571	61.0	1.33×10^{-2}	1.67×10^{-2}	3×10^{-2}	3.42×10^{-5}	83
8	100	5	300	361	−167	29.6	1.42×10^{-1}	0.055	0.197	1.46×10^{-5}	44
8	100	10	300	360	−165	29.5	0.196	0.101	0.297	1.69×10^{-4}	45
10	50	2	300	336	−93	26.9				1.08×10^{-4}	50
10	50	5	300	337	−96	27.0				1.31×10^{-4}	53
10	50	10	300	424	−83	29.7				1.24×10^{-4}	42
10	50	15	300	466	−156	32.2				1.21×10^{-4}	37
6	50	2	300	150	−359	45				4.81×10^{-5}	79
6	50	5	300	152	−359	44.7				5.74×10^{-5}	81
6	50	10	300	526	−291	37.1				8.91×10^{-5}	56
6	50	15	300	418	−334	37.0				9.14×10^{-5}	52
10	200	2	300	384	−113	28.9				1.83×10^{-4}	30
10	200	5	300	387	−113	29.0				2.23×10^{-4}	31
10	200	10	300	390	−116	29.1				2.55×10^{-4}	31
10	200	15	300	389	−119	29.2				2.61×10^{-4}	31
6	200	2	300	326	−238	31.6				1.29×10^{-4}	55
6	200	5	300	325	−239	31.6				1.52×10^{-4}	55
6	200	10	300	328	−244	31.9				1.76×10^{-4}	55
6	200	15	300	329	−246	32.0				1.84×10^{-4}	55
10	50	5	100	390	−145	29.8	0.153	0.087	0.24	1.31×10^{-4}	52
10	50	5	200	358	−115	28.1	0.145	0.082	0.227	1.31×10^{-4}	52
10	50	5	300	337	−96.2	27.0	–	–	–	1.31×10^{-4}	53
10	50	5	400	323	−83.0	26.2	0.142	0.081	0.223	1.31×10^{-4}	52

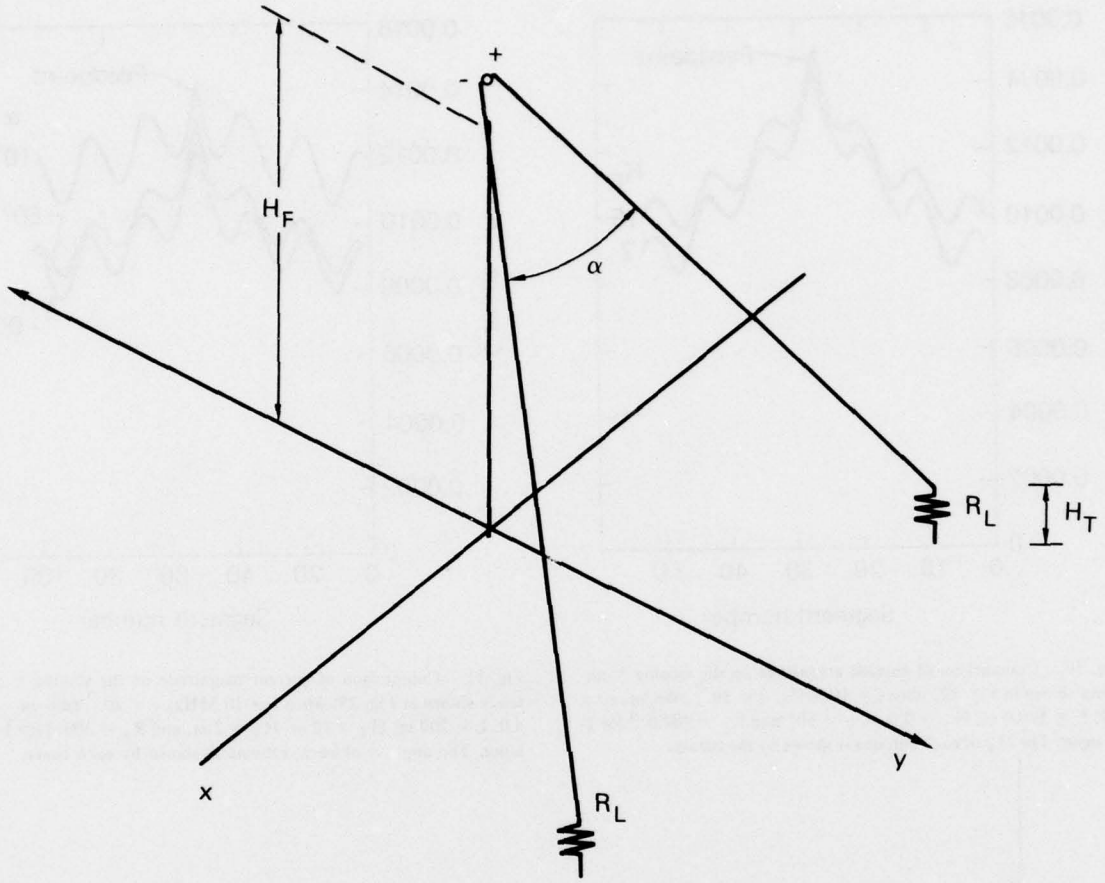

Fig. 29. Sloping V antenna over a lossy interface represented by the x-y plane. The antenna is excited and terminated at a height H_F and H_T above the interface, respectively. The elements of the antenna are separated by an angle α. The total length of the antenna is L. A total of 22 cases were run for the sloping V antenna, as summarized in Table 3. Representative results are shown on the following figures, with more complete data given in Appendix B. The tabulated data prompt three observations:

- o Increasing the wire length, the frequency, and the included angle (up to $\approx 70°$) increases the maximum field strength.
- o The maximum in the elevation pattern lowers with increasing frequency, included angle and height.
- o Input impedance tends to be primarily resistive, except at the lower frequencies.

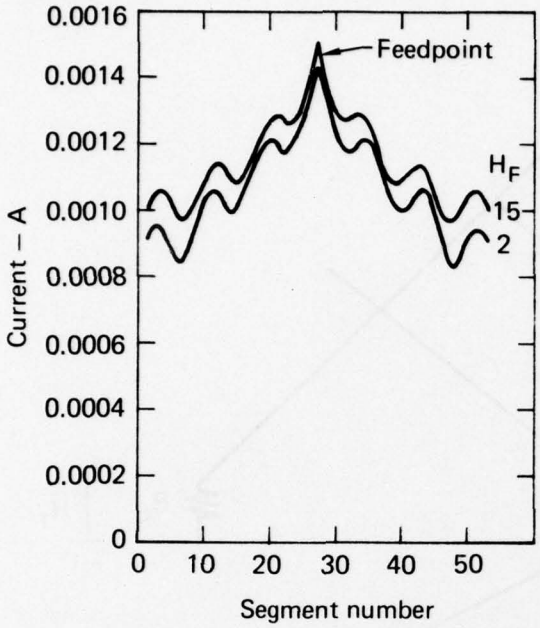

Fig. 30. Comparison of current magnitude on the sloping V antenna shown in Fig. 29, when f = 10 MHz, $\sigma = 10^{-3}$ mho/m, ϵ_r = 4.0, L = 100.0 m, H_T = 2.0 m, $\alpha = 60°$ and R_L = 300.0 Ω for 1-W input. The H_F of each antenna is shown by the curves.

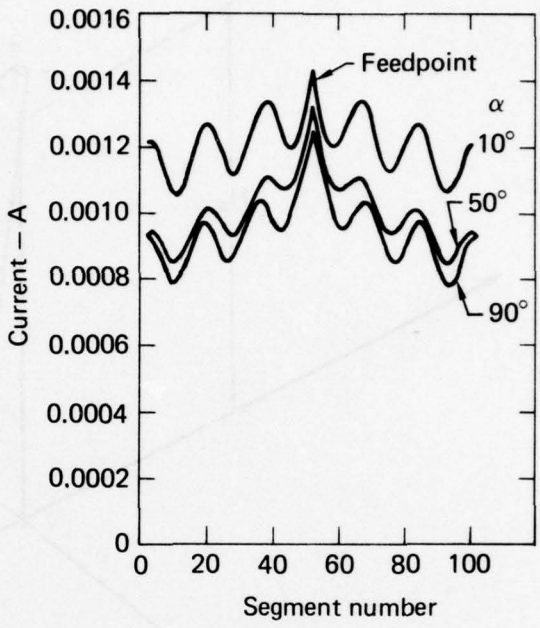

Fig. 31. Comparison of current magnitude on the sloping V antenna shown in Fig. 29, when f = 10 MHz, $\sigma = 10^{-3}$ mho/m, ϵ = 4.0, L = 200 m, H_F = 10 m, H_T = 2 m, and R_L = 300 Ω for 1-W input. The angle α of each antenna is shown by each curve.

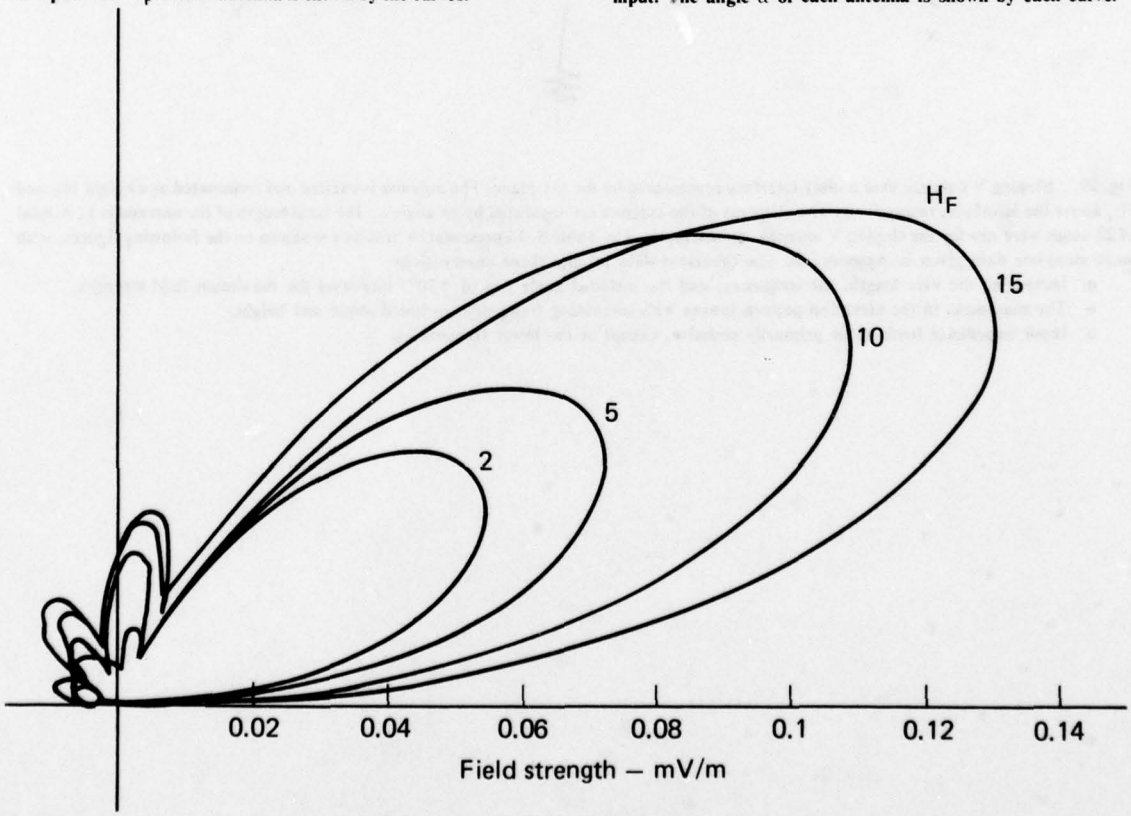

Fig. 32. Radiation pattern for the antenna shown in Fig. 29, when f = 10 MHz, $\sigma = 10^{-3}$ mho/m, ϵ_r = 4, L = 100 m, H_T = 2 m, $\alpha = 60°$, and R_L = 300 Ω for 1-W input. The height H_F of each antenna is shown by each curve.

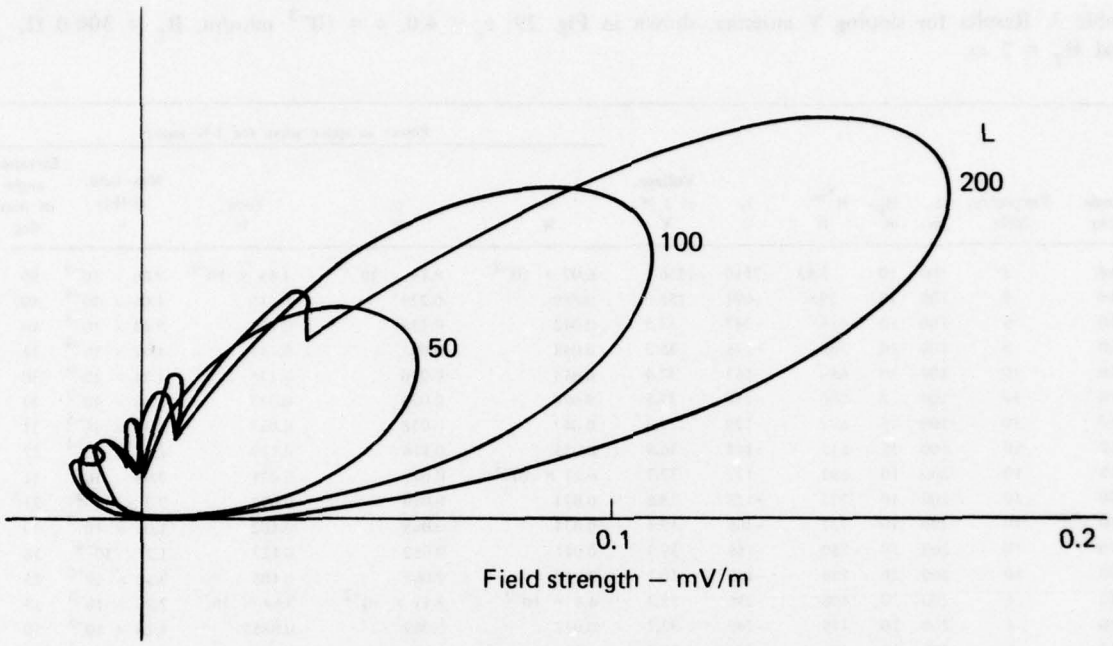

Fig. 33. Radiation pattern for the antenna shown in Fig. 29, when f = 10 MHz, $\sigma = 10^{-3}$ mho/m, $\epsilon_r = 4.0$, $H_F = 10$ m, $H_T = 2$ m, $\alpha = 60°$ and $R_L = 300\ \Omega$ for 1-W input. The length L is shown by each curve.

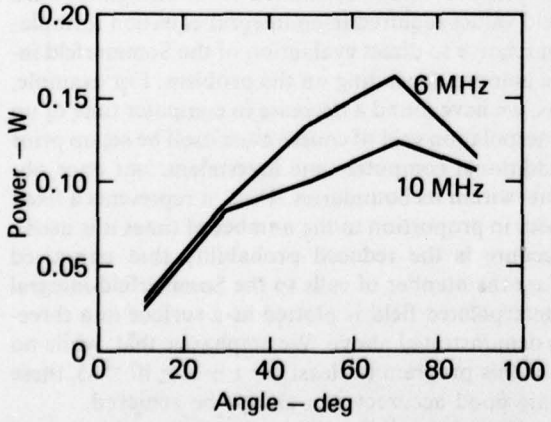

Fig. 34. Plot of the total power in the far field as a function of angle α for the antenna shown in Fig. 29, when $\sigma = 10^{-3}$ mho/m, $\epsilon_r = 4$, L = 200 m, $H_T = 2$ m, $H_F = 10$ m, and $R_L = 300\ \Omega$ for 1-W input. The frequencies are shown by each curve.

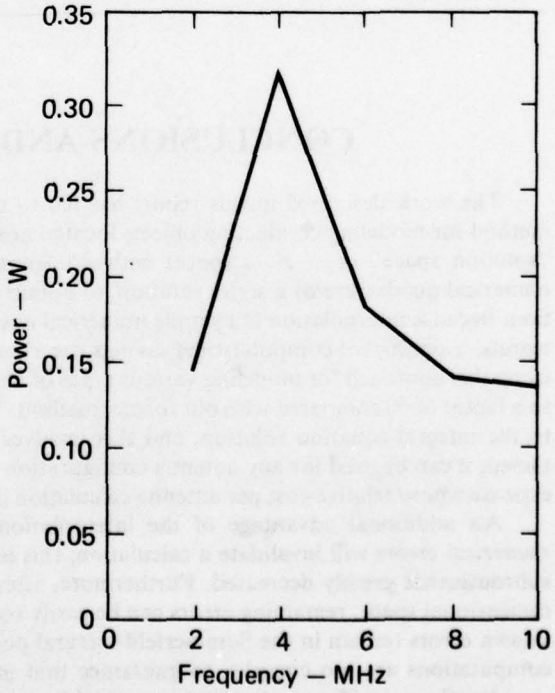

Fig. 35. Plot of total power in the far field as a function of frequency for the antenna shown in Fig. 29, when $\sigma = 10^{-3}$ mho/m, $\epsilon_r = 4$, L = 100 m, $H_T = 2$ m, $H_F = 10$ m, $R_L = 300$, and $\alpha = 60°$ for 1-W input.

Table 3. Results for sloping V antenna, shown in Fig. 29; $\epsilon_r = 4.0$, $\sigma = 10^{-3}$ mho/m, $R_L = 300.0\ \Omega$, and $H_T = 2$ m.

Angle, deg	Frequency, MHz	L, m	H_F, m	$R^{Z_{in}}$, Ω	I, Ω	Voltage, at 1 W, V	Power in space wave for 1-W input: θ, W	φ, W	Total, W	Max field, (RIEI) V	Elevation angle of max, deg
60	2	100	10	5.83	−2110	1236	6.07×10^{-2}	8.44×10^{-2}	1.45×10^{-1}	7.06×10^{-5}	90
60	4	100	10	39.6	−691	156	0.089	0.229	0.318	1.05×10^{-4}	80
60	6	100	10	414	−247	33.5	0.042	0.139	0.182	9.43×10^{-5}	50
60	8	100	10	569	−178	35.3	0.048	0.093	0.141	1.07×10^{-4}	37
60	10	100	10	659	−163	37.4	0.044	0.090	0.135	1.24×10^{-4}	30
60	10	100	2	686	−110	37.5	0.050	0.023	0.073	6.36×10^{-5}	33
60	10	100	5	671	−129	37.3	0.047	0.038	0.085	8.32×10^{-5}	31
60	10	100	15	645	−144	36.8	0.033	0.116	0.149	1.45×10^{-4}	27
10	10	200	10	692	−117	37.7	6.24×10^{-3}	0.015	0.021	2.98×10^{-5}	31
30	10	200	10	723	−128	38.6	0.023	0.049	0.072	7.3×10^{-5}	31
50	10	200	10	737	−166	39.4	0.034	0.068	0.102	1.05×10^{-4}	30
70	10	200	10	750	−186	39.9	0.041	0.082	0.123	1.2×10^{-4}	28
90	10	200	10	786	−118	40.1	0.037	0.068	0.105	9.58×10^{-5}	25
10	6	200	10	408	−296	35.3	4.4×10^{-3}	2.17×10^{-2}	2.61×10^{-2}	2.26×10^{-5}	53
30	6	200	10	419	−249	33.7	0.017	0.069	0.0858	5.28×10^{-5}	50
50	6	200	10	466	−282	35.7	0.031	0.104	0.135	7.71×10^{-5}	50
70	6	200	10	500	−296	36.8	0.043	0.118	0.161	9.65×10^{-5}	47
90	6	200	10	907	−97.1	42.8	0.047	0.654	0.113	8.61×10^{-5}	39
60	6	50	10	781	−468	46.1	7.92×10^{-3}	3.68×10^{-2}	4.49×10^{-2}	4.33×10^{-5}	52
60	10	50	10	795	−246	41.7	0.022	0.0478	0.0694	6.88×10^{-5}	35
60	6	200	10	455	−161	32.0	0.119	0.206	0.325	1.51×10^{-4}	46
60	10	200	10	690	−151	38.0	0.095	0.128	0.223	1.88×10^{-4}	24

CONCLUSIONS AND RECOMMENDATIONS

The work described in this report has led to development of a simple, but highly effective numerical method for modeling conducting objects located near an interface. The procedure is based on interpolating a "solution space" ($z + z'$, ρ space) between Sommerfeld-integral values calculated from straightforward numerical quadrature or a series solution, to obtain the field values required in an integral-equation formulation. Because interpolation is a simple numerical operation relative to direct evaluation of the Sommerfeld integrals, a significant computer-time savings can result, the amount depending on the problem. For example, using this approach for modeling various types of antennas, we have found a decrease in computer time of up to a factor of 60 compared with our former method. The interpolation grid of course must itself be set up prior to the integral-equation solution, and this involves an additional computer-time investment, but once obtained, it can be used for any antenna configuration that fits within its boundaries. Thus, it represents a fixed expense whose relative cost per antenna calculation decreases in proportion to the number of times it is used.

An additional advantage of the interpolation procedure is the reduced probability that unnoticed numerical errors will invalidate a calculation; this is because the number of calls to the Sommerfeld-integral subroutines is greatly decreased. Furthermore, after the interpolated field is plotted as a surface in a three-dimensional space, remaining errors can be easily seen, as demonstrated above. We emphasize that, while no known errors remain in the Sommerfeld-integral portion of this program (at least for $z + z' \gtrsim 10^{-4}\lambda$), these computations are too complex to guarantee that uniformly good accuracy can always be achieved.

Another significant development in this work has been extending and improving our numerical procedures to permit locating objects within $10^{-3}\lambda$ (or even less) of the interface. This feature allows us to model such closely coupled conductors as the wires in a ground screen, without resorting to the approximations usually employed.

We have demonstrated the capabilities of the new program, SOMINT, by performing some limited parametric calculations for several antennas. These initial applications are by no means intended to be conclusive or complete, but rather to illustrate the kinds of information that are derivable and the kinds of problems that can be handled with the programs. It should be recognized that antennas located near the earth may experience perturbations due to a laterally and vertically inhomogeneous and undulating ground that the idealized model employed here (a flat, uniform half-space) does not include. Whether such features can ever be, or even should be, modeled is not obvious. In any case, the current capability should allow antenna designers to optimize antenna performance while including the dominant ground effect (i.e., direct reflection from the interface) in a way heretofore neither analytically nor experimentally possible.

Most of the effort in this program has been directed towards implementing the basic numerical procedures. Much remains to be done to improve the program and expand its applicability. Some possibilities for improvement and various applications are discussed below.

Ground-Screen Models

Ground screens (or counterpoises) are used either to control antenna impedance or pattern. Of necessity, their analysis has been approximate and based primarily upon using an effective surface impedance. The most obvious limitations of this approach are its failure to handle screens containing few or widely spaced wires, its inapplicability to predict low-angle radiation, and its inability to account for the finite extent of the screen on the antenna's current distribution. The surface-impedance approximation, furthermore, does not lend itself to inclusion in an otherwise rigorous Sommerfeld-based approach.

A really useful and realistic analysis of ground screens and counterpoises requires, instead, that the currents in the ground-screen wires be found in a self-consistent fashion. This approach could not have been seriously considered without the means to evaluate Sommerfeld integrals efficiently and accurately. But the techniques developed in the current work make this not only feasible, but practicable. We therefore recommend that SOMINT be extended specifically to handle problems involving antennas that interact with sparse systems of wires near (0.001 λ) the interface, and to which they may be attached. The use of ground screens below tactical antennas could provide a significant improvement in their performance. With the new method described above, it is now feasible to study antennas currently in use to see how ground screens might best be used or whether present designs can be replaced by newer antennas with ground screens.

Dielectric Sheaths

A recurring problem, especially with respect to buried conductors, is how a dielectric or insulating sheath changes the behavior of a metallic object. This is especially important in conducting media where a sheath prevents the direct flow of conduction current between the object and the medium. It is thus necessary to include the dielectric coating in the model if realistic results are to be obtained. Particular attention should also be paid to the end conditions where the conduction current on the wire may not vanish as it does in free space. Several approaches are worth considering here, with perhaps the most promising one based on a displacement current model for the sheath.

Two-Half-Space Problem

The current work deals with wire objects located wholly on one side or the other of the interface, so that the Sommerfeld integrals are functions only of z' (source height) + z (observation height), and ρ (radial separation). Many applications occur where two objects are on opposite sides of the interface. The self-fields of these objects can be handled efficiently with the present code. However, interaction of these objects across the interface involves Sommerfeld integrals of the three space variables, z', z and ρ. Using an interpolation scheme for this problem may not be practicable because it would then involve three dimensions. Thus, schemes other than interpolation should be considered, including the transmission-coefficient approximation and various asymptotic expansions. These and the interpolation technique could then be compared to find the approach best suited to this problem in terms of efficiency and accuracy.

Effect of Nonuniform Currents

Associated with the development of ground-screen models above is the validity of the thin-wire approximation as the wire approaches the interface. Specifically, we must assess the degree of validity of the assumption that the current is uniformly distributed around the wire's circumference as the wire approaches the interface. Within a few wire radii of the ground, this assumption appears questionable, and its effect on the accuracy of the ground-screen model is uncertain. We might expect that whether a thin wire is lying on the ground or a few radii above, the difference would be small in any case. That however, should be studied to validate the model.

Penetrating Wires

A logical extension to the two-half-space problem above is the case where the object(s) is cut by the interface. This occurs, for example, when an antenna is driven against a ground rod that serves as a counterpoise.

Many small mobile antennas used by the Army currently employ ground stakes for connecting the transmitter to one end of the antenna and sometimes for termination as well. Although ground stakes must obviously affect the input impedance and radiation patterns of the antenna, their placement and design have never been studied rigorously. Computer modeling of this problem would permit studying the effects of ground-staked antennas with the goals of improving the present performance achievable with mobile antennas.

In this case, we must be concerned not only with the field evaluation but also with determining what special current conditions, if any, are needed at the interface. For example, the reflection of a plane wave from a half-space requires continuity of tangential fields that can result in discontinuities in their derivatives. On a penetrating conductor, continuous tangential fields (tangential H and normal E to the wire) at the interface could result only if the charge density is discontinuous. This suggests the need for deriving a current-slope condition different from that used at junctions in free space.

Antenna Efficiency

Previous work done at LLL has demonstrated that the efficiency of antennas like the Beverage and horizontal dipole can be significantly improved by arraying them. Efficiency increases of 300% and more appear readily achievable, without the use of ground screens. This increased efficiency has been studied computationally and found to occur because the multiple elements in an array increase the rate at which the antenna current radiates, thus reducing the power loss into the ground. Increasing the size of the antenna wires has a similar effect. Thus, antennas like the Beverage, heretofore considered too inefficient for tactical communications, might be made competitive in this respect with the vertical half-rhombic and slanted V, for example. This may mean that ease of deployment and efficiency are not necessarily incompatible. In this application of the SOMINT code, existing antennas as well as alternate designs could be evaluated to determine the extent to which multi-element arrays would be effective in increasing efficiency, and thus reducing power requirements of portable communications systems.

Frequency Domain Interpolation

Although the SOMINT code operates nearly as fast as Antenna Modeling Program (AMP), which uses the reflection-coefficient approximation, the cost of filling the solution-space interpolation matrix is not small. Therefore, in evaluating the frequency dependence of an antenna, it is desirable to minimize the number of frequencies at which the matrix is needed. One method is to interpolate between the frequencies at which the matrix is calculated. This leads, in essence, to a three-dimensional interpolation scheme whose storage requirements could be prohibitive. However, if a linear interpolation in frequency is used, only the two solution-space interpolation matrices that lie on either side of the desired frequency need be used. A solution-space matrix at the intermediate frequency can then be obtained from them; following that, the procedure is identical to that now used. This new matrix could, of course, be saved for subsequent reuse, further reducing the required computer time. It is worth noting that a similar approach could be used for varying the permittivity and conductivity.

Nonwire Integral Equations

The SOMINT code is currently implemented in an electric-field, thin-wide, integral-equation code. But many objects of interest are surfaces rather than wires. While they may be modeled with a measure of success using wire grids, they can be more efficiently and accurately handled with an integral equation applicable to surfaces. The same interpolation procedure for obtaining the Sommerfeld integrals applies irrespective of the form of the integral equation, so that the improvements now available in SOMINT could also be realized for surfaces.

User-Oriented Improvements

The Numerical Electromagnetics Code (NEC) is probably the most user-oriented and thoroughly documented code available for modeling wire, surface, and hybrid objects. It would thus be very desirable to add to it the newly developed Sommerfeld-integral capability now included only in SOMINT, and to provide the necessary documentation. At the same time, it would be worthwhile to incorporate further needed improvements into NEC that have been identified as a result of our ongoing interaction with the AMP-NEC user community. These should include, but not be limited to, improvement of the input data generation routine to minimize user errors; modification of the appropriate routines to eliminate the small-argument errors that occur when segment sizes less than 0.001 λ are used; and development of a routine to more accurately assess impedance-loss effects by integrating the loss term. Actually, this should be a modest continuing effort to respond to problems as they arise and to provide the information to the user community.

User-Experience Data Base

One problem that often occurs, especially when either new users first attempt to employ a code such as NEC, or even when experienced NEC users apply it to a significantly different problem, is that several iterations are required before physically realistic results are obtained. It would be extremely beneficial, by reducing wasted effort and providing more timely results, to concisely document these learning experiences. If a description; a given antenna type; the approach taken; results obtained; problems encountered; etc., were written in a common format and made available to those involved in antenna modeling, greater efficiency would surely follow. As it evolves, this user-experience data base would provide guidance for modeling a growing variety of applications and thus reduce the difficulties mentioned above. It would also provide guidance concerning problem areas needing attention concerning computer code improvements.

ACKNOWLEDGMENTS

This work was funded by the U.S. Army Communication Electronic Installation Agency, Fort Huachuca, Arizona. The authors are grateful for valuable discussions with individuals at Fort Huachuca, particularly Ed Bramel and George Lane.

REFERENCES

1. A. Bănos, *Dipole Radiation in the Presence of a Conducting Half-Space* (New York, Pergamon Press, 1966).
2. A. J. Poggio and E. K. Miller "Integral Equation Solutions of Three-Dimensional Scattering Problems," in *Computer Techniques for Electromagnetics*, R. Mittra, Ed. (New York Peragmon Press, 1973).
3. K. K. Mei, "On the Integral Equation of Thin Wire Antennas," *IEEE Trans. Antennas Propagat.* **AP-13,** 374 (1965).

4. R. F. Harrington, *Field Computation by Moment Methods* (New York Macmillan, 1968).
5. J. H. Richmond, *Computer Analysis of Three-Dimensional Wire Antennas*, Ohio State University, Department of Electronics Engineering, ElectroScience Laboratory, Tech. Rept. 2708-4 (1969).
6. E. K. Miller and F. J. Deadrick *Some Computational Aspects of Thin-Wire Modeling*, Lawrence Livermore Laboratory, Rept. UCRL-74818 (1973).
7. C. M. Butler "Currents Induced on a Pair of Skewed Crossed Wires," *IEEE Trans. Antennas Propagat.* **AP-20,** 731, (1972).
8. J. H. Richmond, "Digital Computer Solutions of the Rigorous Equations for Scattering Problems," *Proc. IEEE* **53,** 796 (1965).
9. W. L. Curtis, Boeing Space Center, Seattle, Wash., private communication (1972).
10. H. H. Chao and B. J. Strait, *Computer Programs for Radiation and Scattering by Arbitrary Configurations of Bent Wires*, Syracuse University, Scientific Rept. No. 7 on Contract No. F19628-68-C-0180; AFCRL-70-0374 (September 1970).
11. E. K. Miller, A. J. Poggio, and G. J. Burke, "An Integro-Differential Equation Technique for the Time Domain Analysis of Thin Wire Structures, Part I. The Numerical Method," *J. Computational Phys.* **12,** 24 (1973).
12. Y.S. Yeh and K. K. Mei, "Theory of Conical Equiangular Spiral Antennas: Part I — Numerical Techniques," *IEEE Trans. Antennas Propagat.* **AP-15,** 634 (1967).
13. S. Gee, *et al.*, "Computer Techniques for Electromagnetic Scattering and Radiation Analyses," invited paper presented at the *The Electromagnetic Compatibility Meeting*, Philadelphia, Pa., (1971).
14. M. G. Andreasen and F. B. Harris, Jr., *Analysis of Wire Antennas of Arbitrary Configuration by Precise Theoretical Numerical Techniques*, Granger Associates, Palo Alto, Calif., Contract DAAB07-67-C-0631, Tech. Rept. ECOM 0631-F (1968).
15. R. F. Harrington, "Straight Wires with Arbitrary Excitation and Loading," *IEEE Trans. Antennas Propagat.* **AP-15,** 502, (1967).
16. E. K. Miller and G. J. Burke, "Numerical Integration Methods," *IEEE Trans. Antennas Propagat.* **AP-17,** 669 (1969).
17. C. D. Taylor, "Thin Wire Receiving Antenna in a Parallel Plate Waveguide," *IEEE Trans. Antennas Propagat.* **AP-15,** 572 (1967).
18. A. Sommerfeld, "Uber der Ausbreitung der Willen in der drahtlosen Telegraphic," *Ann. Physik* **28,** 663 (1909).
19. A. Sommerfeld, *Partial Differential Equations in Physics* (New York, Academic Press, 1964).
20. K. A. Norton, "The Propagation of Radio Waves Over the Surface of the Earth and in the Upper Atmosphere," *Proc. IRE* **25** (9) (1937), p. 1203.
21. R. J. Lytle and D. L. Lager, *Numerical Evaluation of Sommerfeld Integrals*, Lawrence Livermore Laboratory, Rept. UCRL-51628 (1974).

APPENDIX A. RESULTS FOR A VERTICAL HALF-RHOMBIC ANTENNA

The vertical half-rhombic antenna is shown in Fig. A1. All data shown in this appendix are for $\sigma = 10^{-3}$ mho/m, $\epsilon_r = 4$, $R_L = 300\ \Omega$, $H_T = 2$ m. Figures A2-A35 contain plots of the radiation pattern (at a distance of 10^5 meters) in a vertical plane that contains the antenna and the magnitude of the current on the antenna.

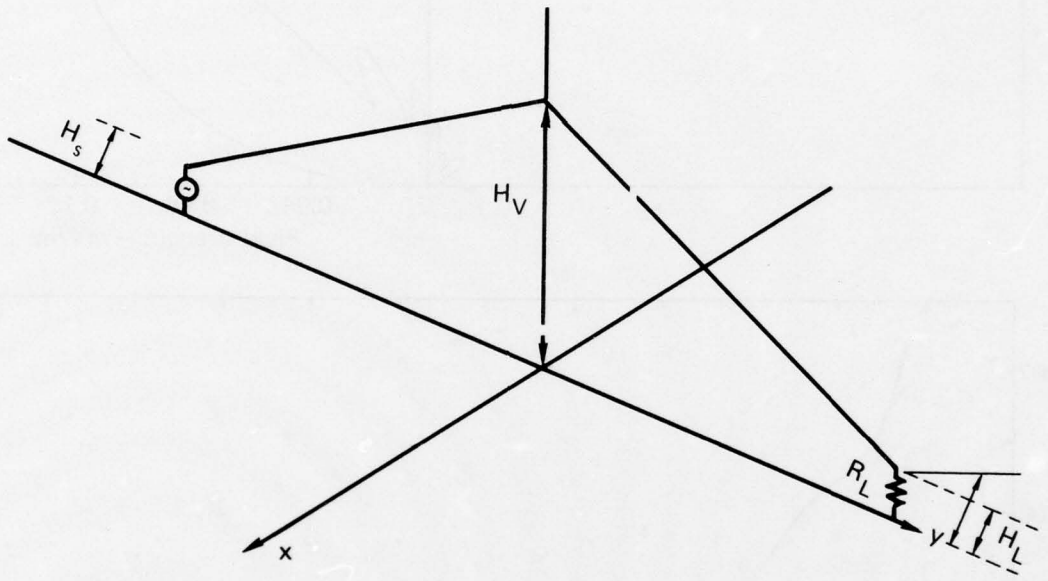

Fig. A1. Vertical half-rhombic antenna above a lossy interface represented by the x-y plane. The antenna is excited by a 1-W source at height H_S loaded at height H_L, both above the interface. The total length of wire in the antenna is L.

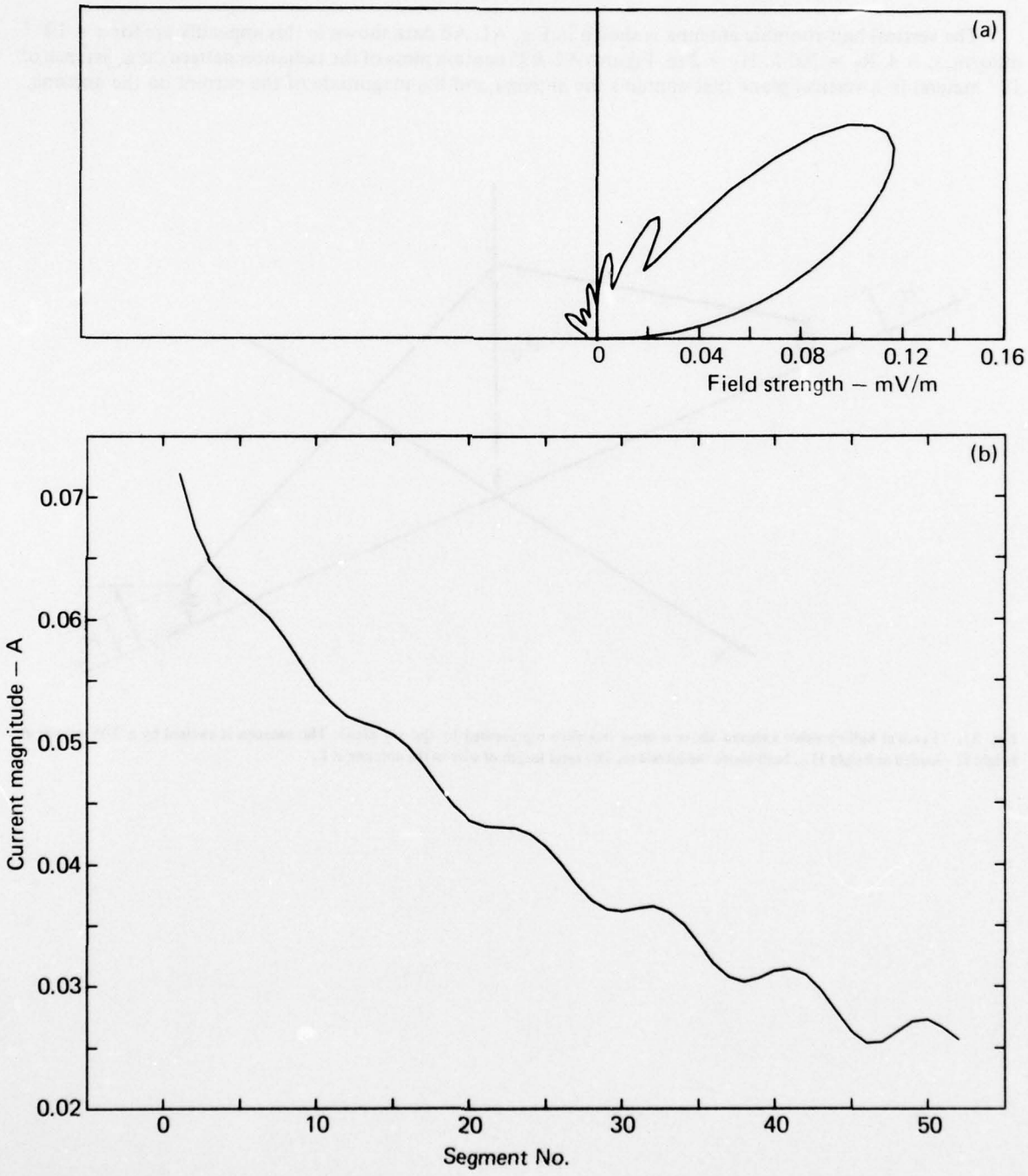

Fig. A2. Results from a vertical half-rhombic antenna: (a) radiation pattern; (b) magnitude of the current on the antenna. L = 100 m; H_v = 2 m; freq = 10 MHz; R_{LOAD} = 300 Ω.

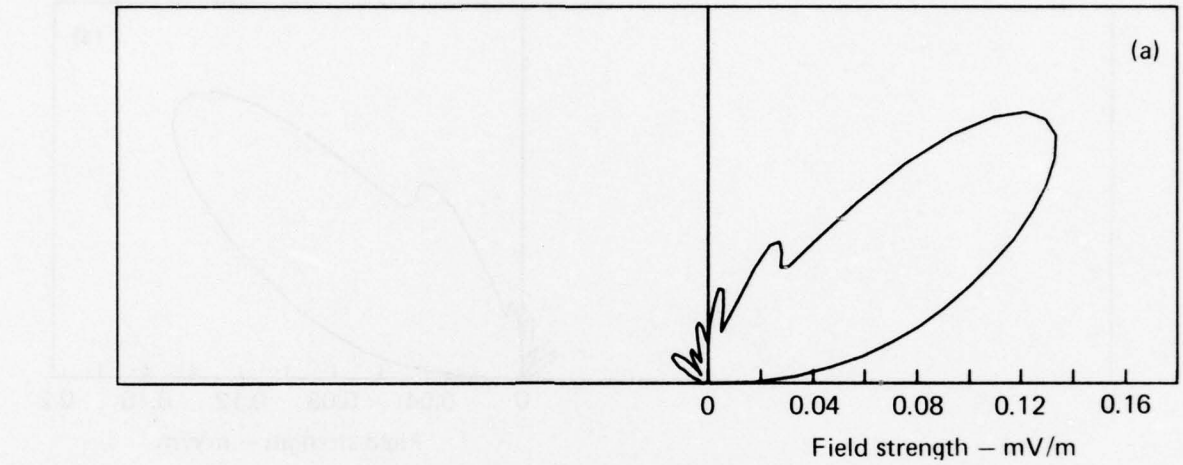

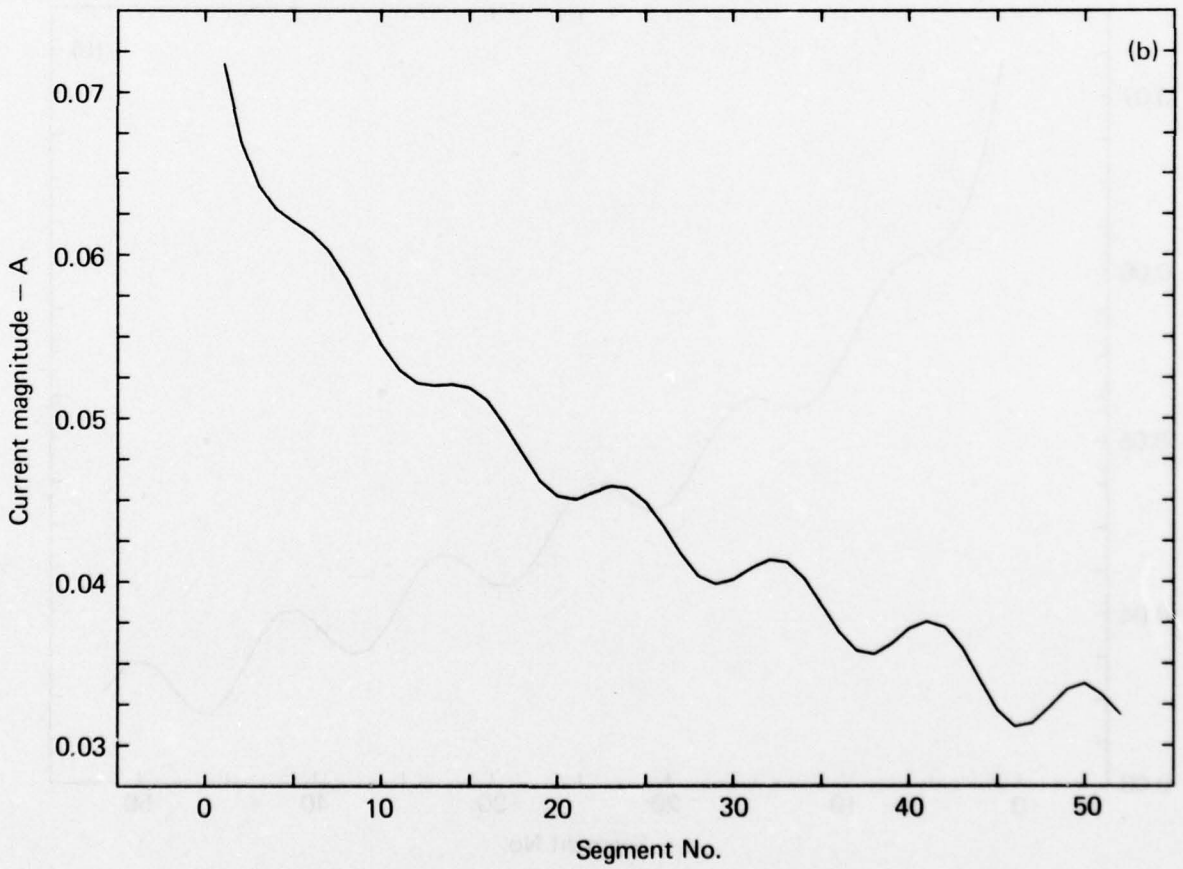

Fig. A3. Results from a vertical half-rhombic antenna: (a) radiation pattern; (b) magnitude of the current on the antenna. L = 100 m; H_v = 5 m; freq = 10 MHz; R_{LOAD} = 300 Ω.

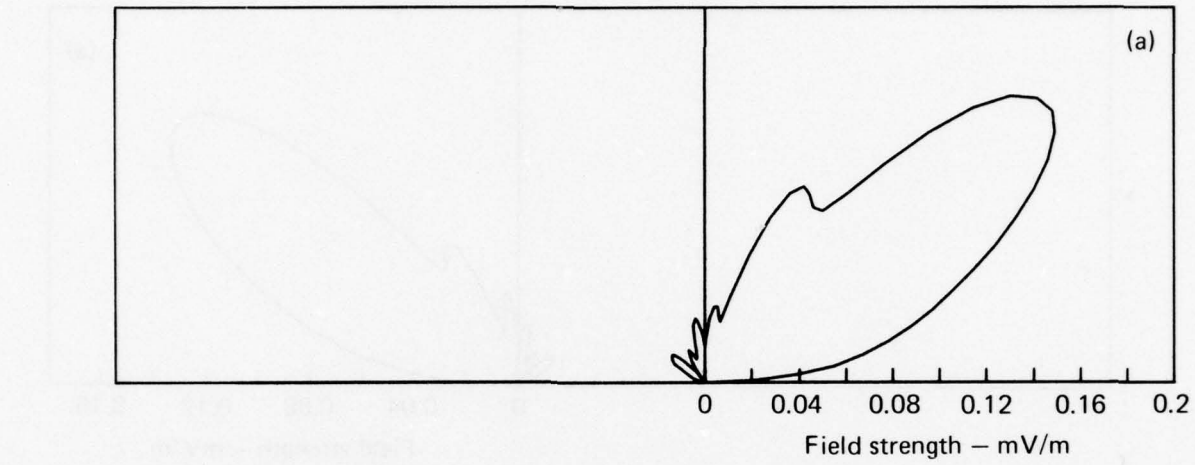

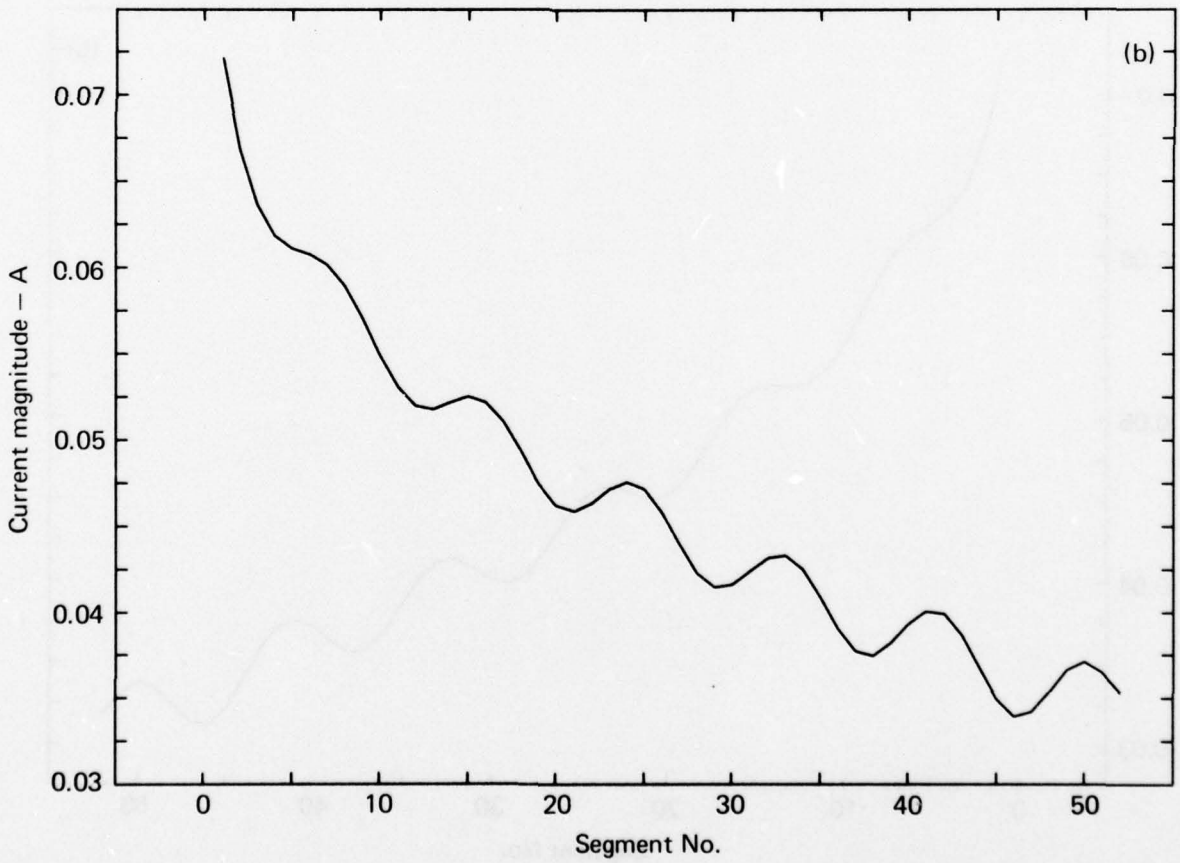

Fig. A4. Results from a vertical half-rhombic antenna: (a) radiation pattern; (b) magnitude of the current on the antenna. L = 100 m; H_v = 10 m; freq = 10 MHz; R_{LOAD} = 300 Ω.

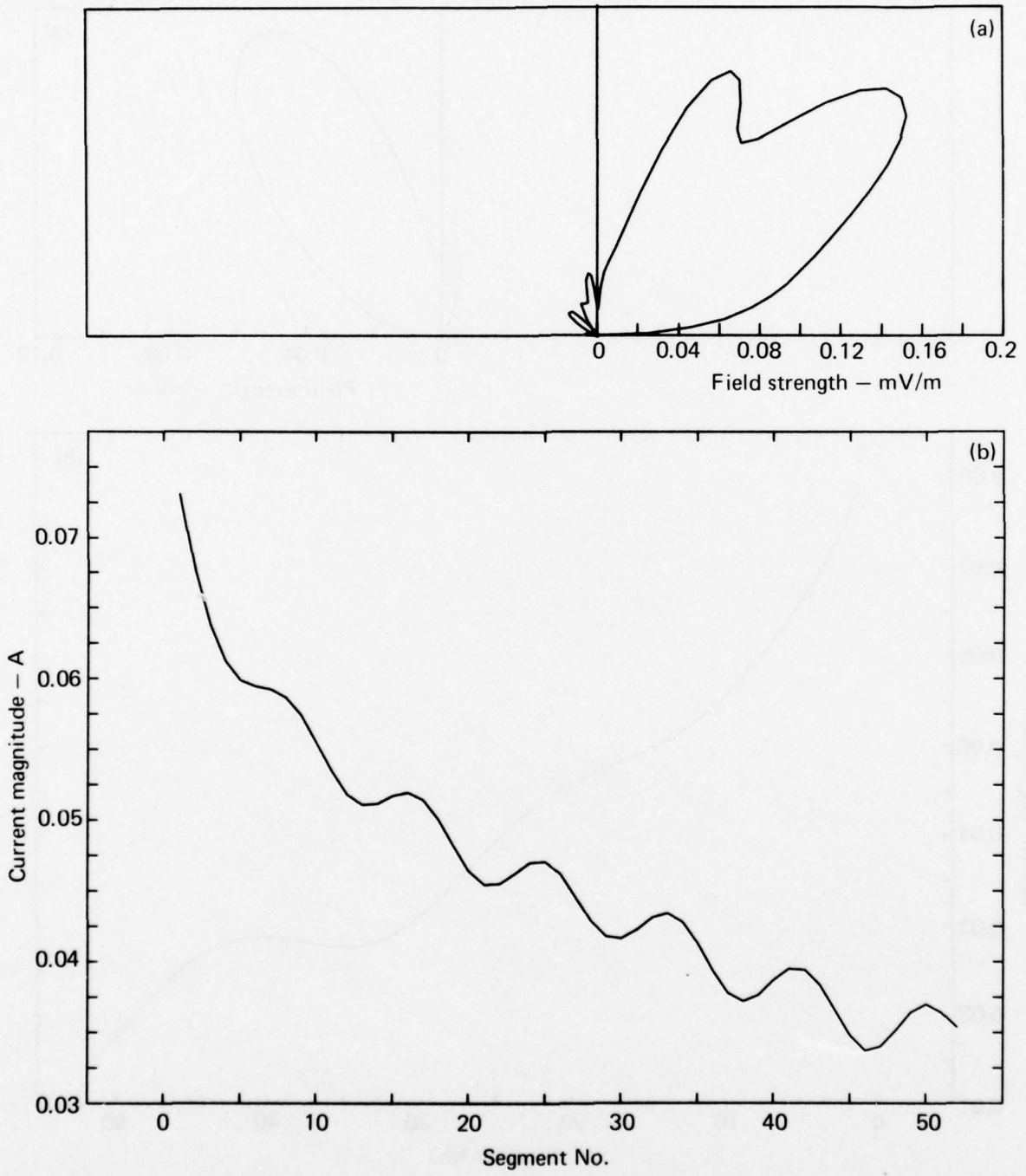

Fig. A5. Results from a vertical half-rhombic antenna: (a) radiation pattern; (b) magnitude of the current on the antenna. L = 100 m; H_v = 15 m; freq = 10 MHz; R_{LOAD} = 300 Ω.

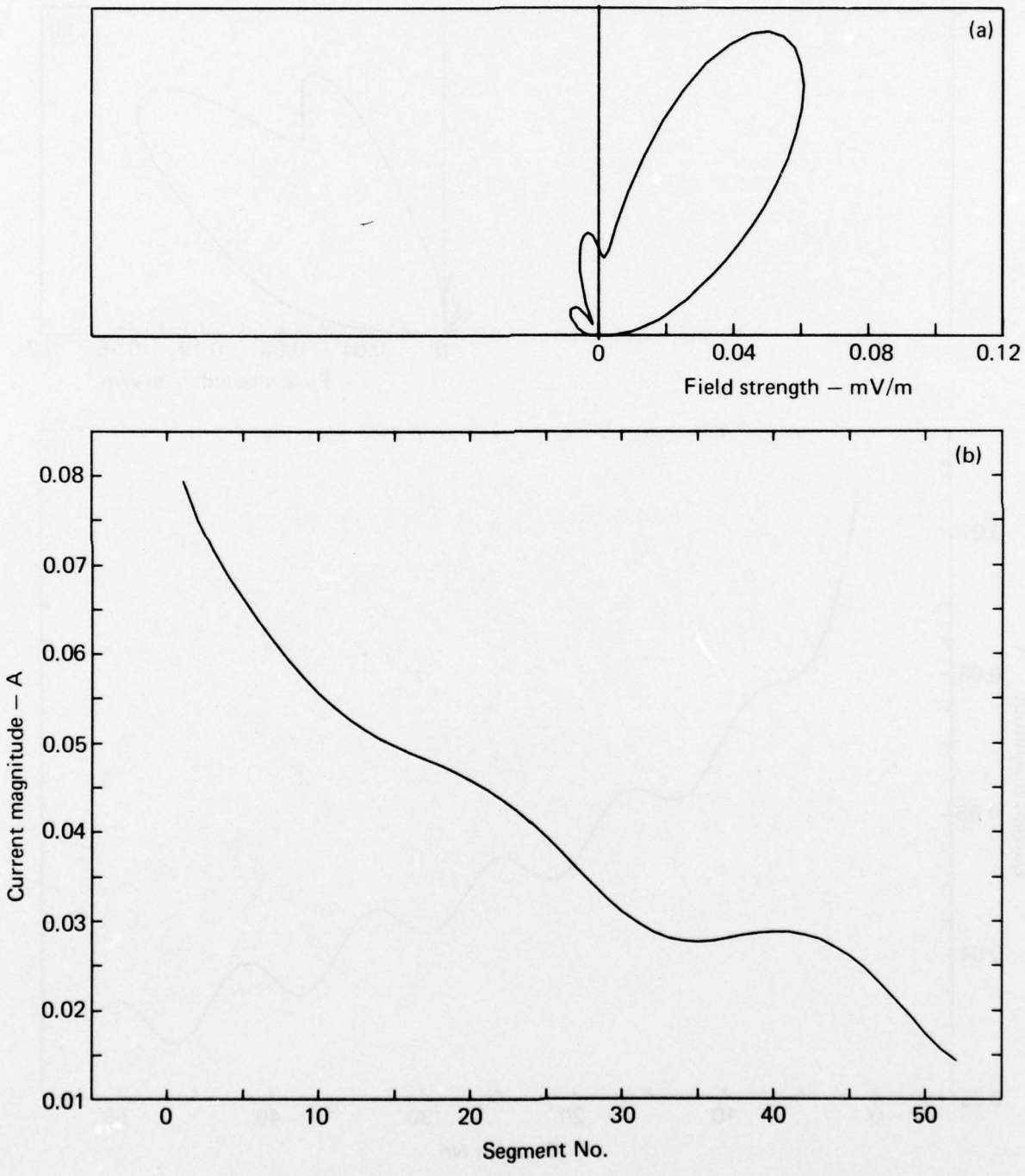

Fig. A6. Results from a vertical half-rhombic antenna: (a) radiation pattern; (b) magnitude of the current on the antenna. L = 100 m; H_v = 2 m; freq = 6 MHz; R_{LOAD} = 300 Ω.

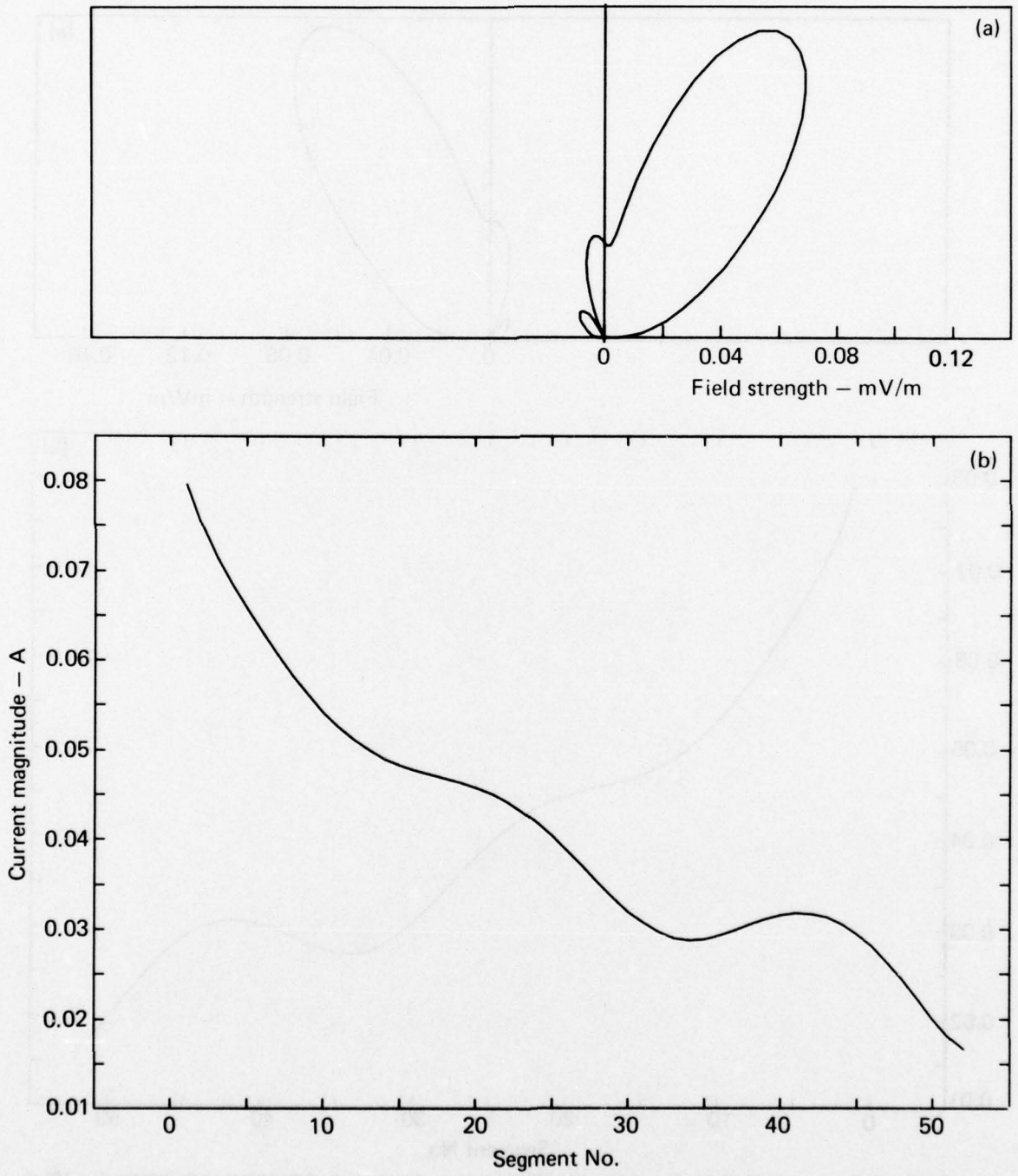

Fig. A7. Results from a vertical half-rhombic antenna: (a) radiation pattern; (b) magnitude of the current on the antenna. L = 100 m; H_v = 5 m; freq = 6 MHz; R_{LOAD} = 300 Ω.

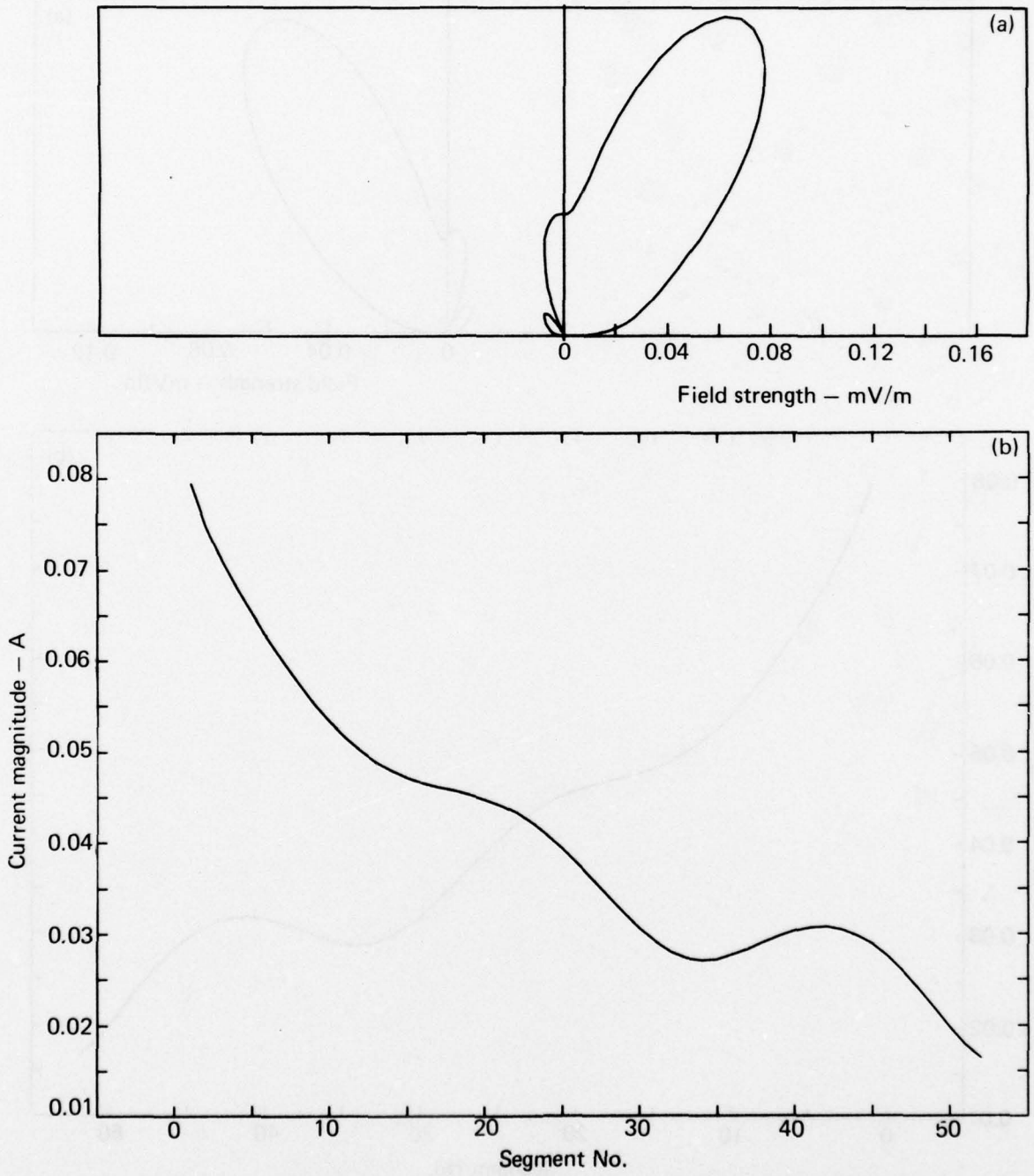

Fig. A8. Results from a vertical half-rhombic antenna: (a) radiation pattern; (b) magnitude of the current on the antenna. L = 100 m; H_v = 10 m; freq = 6 MHz; R_{LOAD} = 300 Ω.

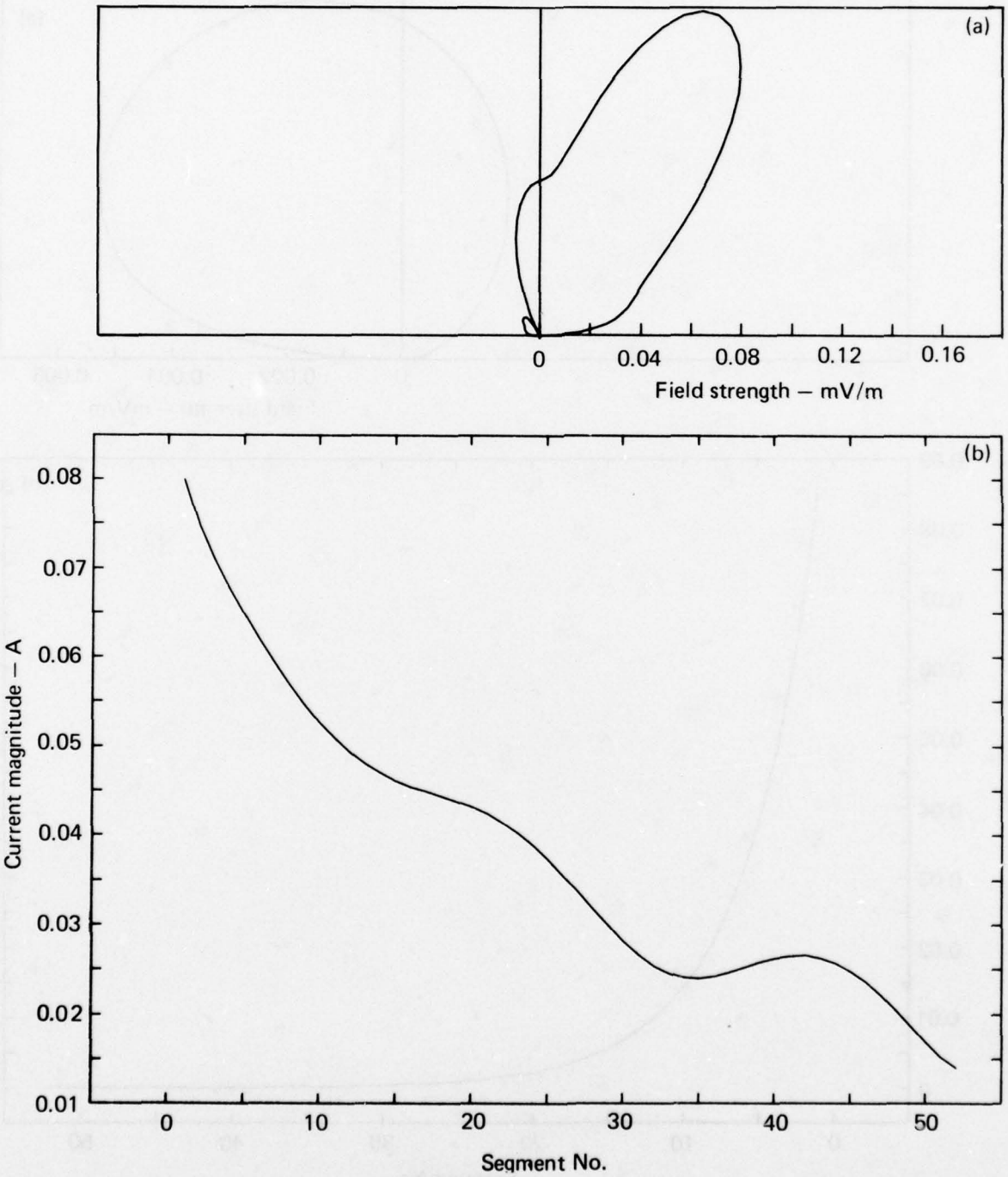

Fig. A9. Results from the vertical half-rhombic antenna: (a) radiation pattern; (b) magnitude of the current on the antenna. L = 100 m; H_v = 15 m; freq = 6 MHz; R_{LOAD} = 300 Ω.

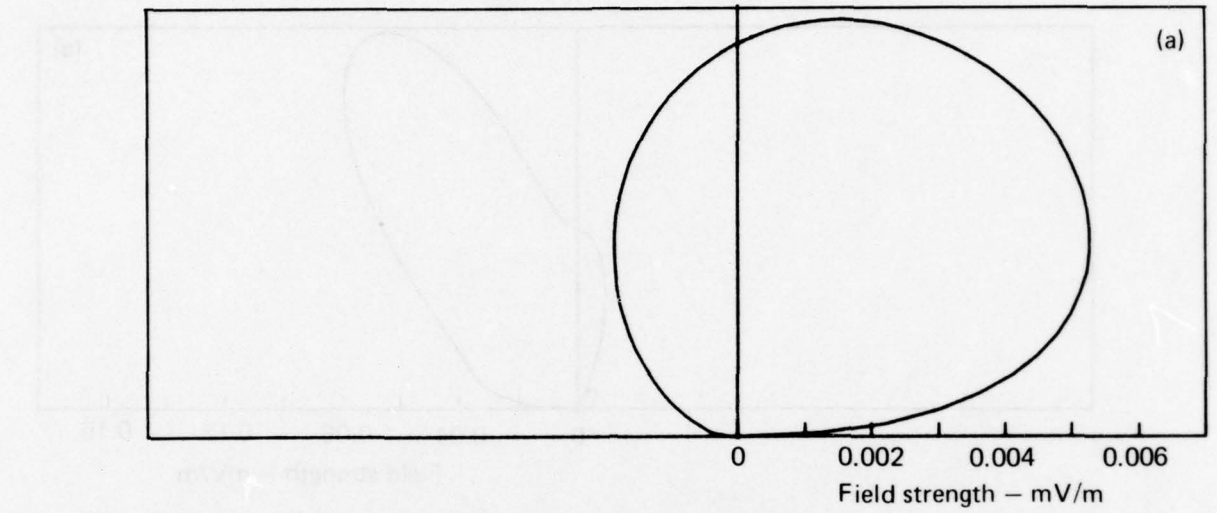

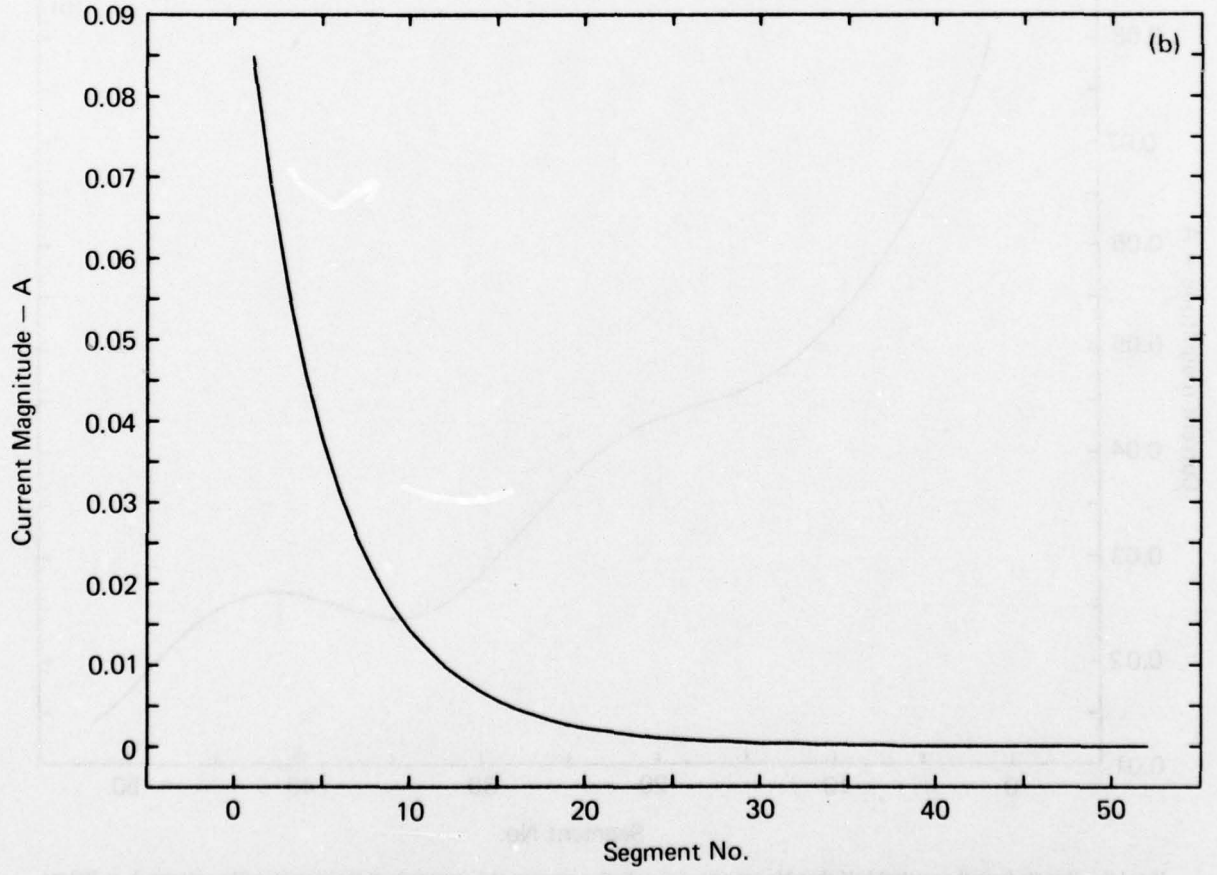

Fig. A10. Results from a vertical half-rhombic antenna: (a) radiation pattern; (b) magnitude of the current on the antenna. L = 100 m; H_v = 5 m; freq = 2 MHz; R_{LOAD} = 300 Ω.

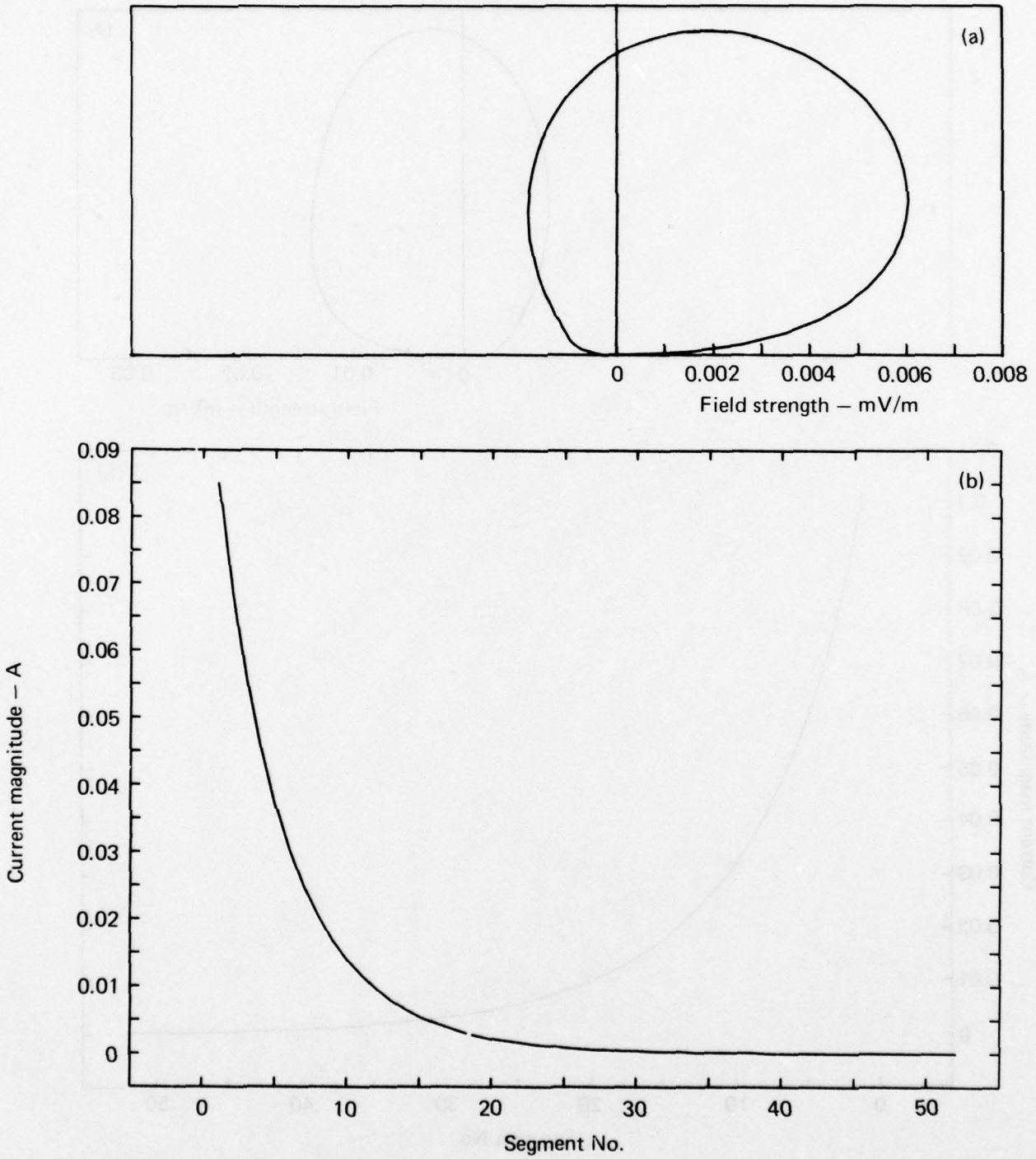

Fig. A11. Results from a vertical half-rhombic antenna: (a) radiation pattern; (b) magnitude of the current on the antenna. L = 100 m; H_v = 10 m; freq = 2 MHz; R_{LOAD} = 300 Ω.

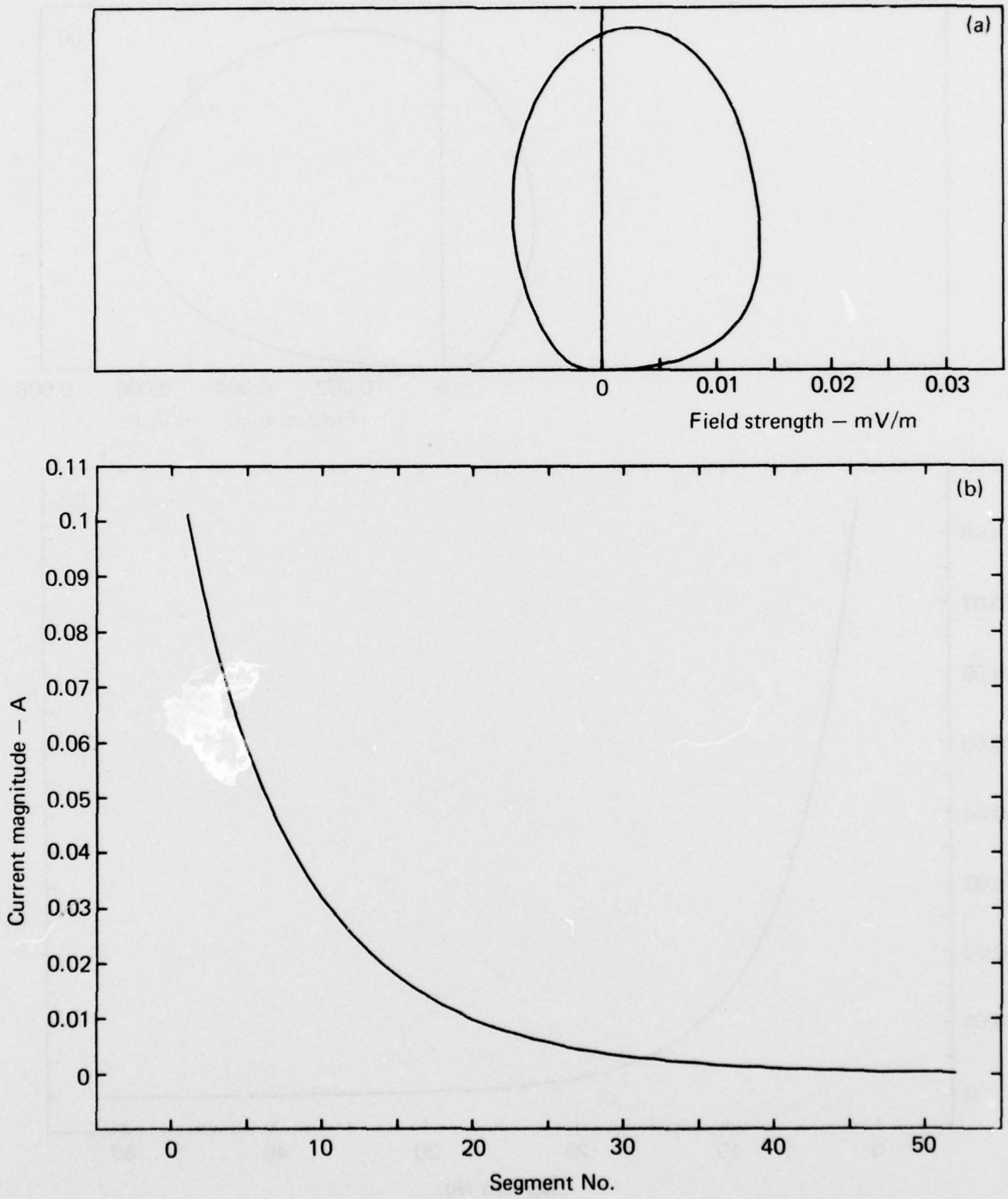

Fig. A12. Results from a vertical half-rhombic antenna: (a) radiation pattern; (b) magnitude of the current on the antenna. L = 100 m; H_v = 5 m; freq = 4 MHz; R_{LOAD} = 300 Ω.

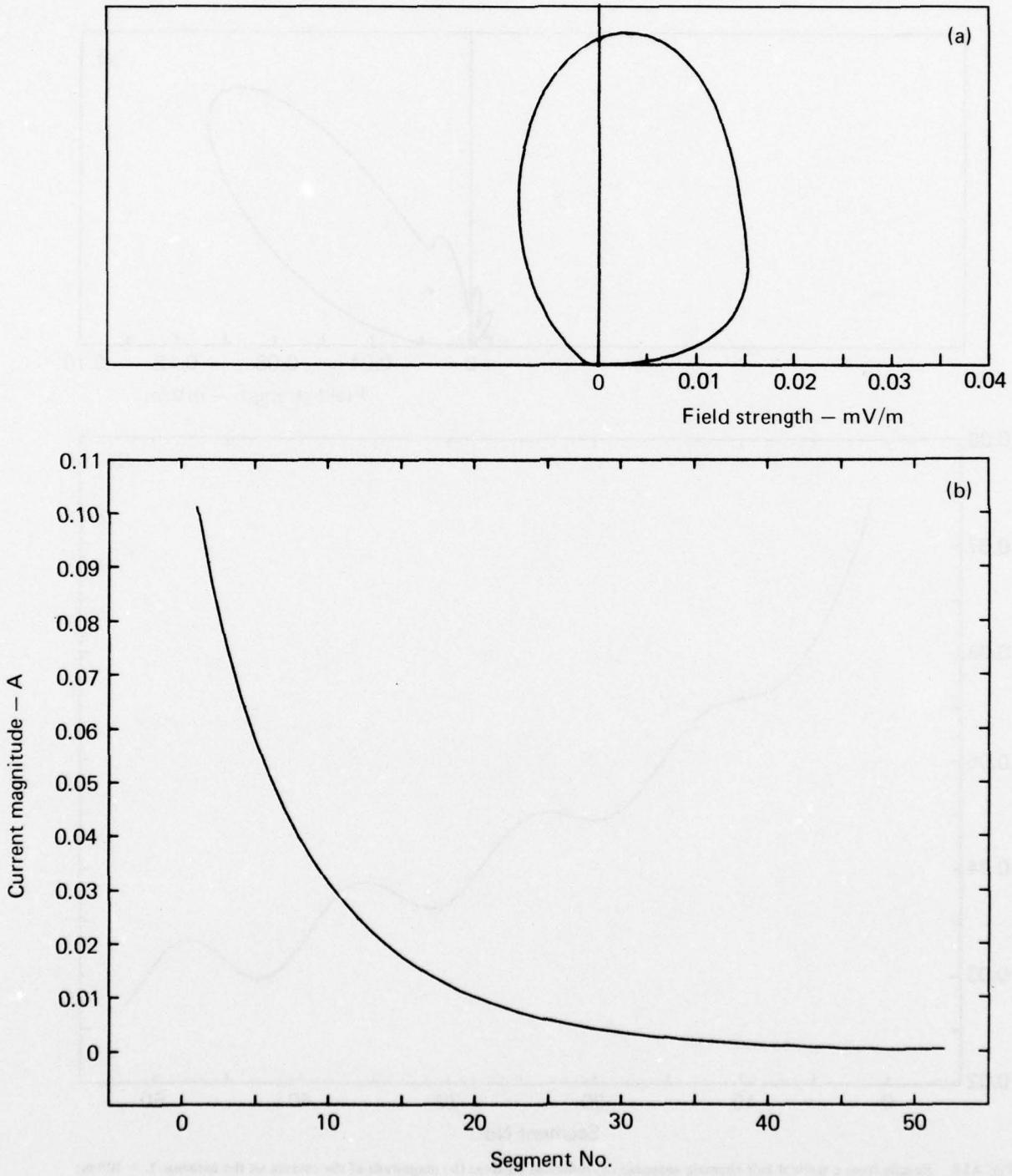

Fig. A13. Results from a vertical half-rhombic antenna: (a) radiation pattern; (b) magnitude of the current on the antenna. L = 100 m; H_v = 10 m; freq = 4 MHz; R_{LOAD} = 300 Ω.

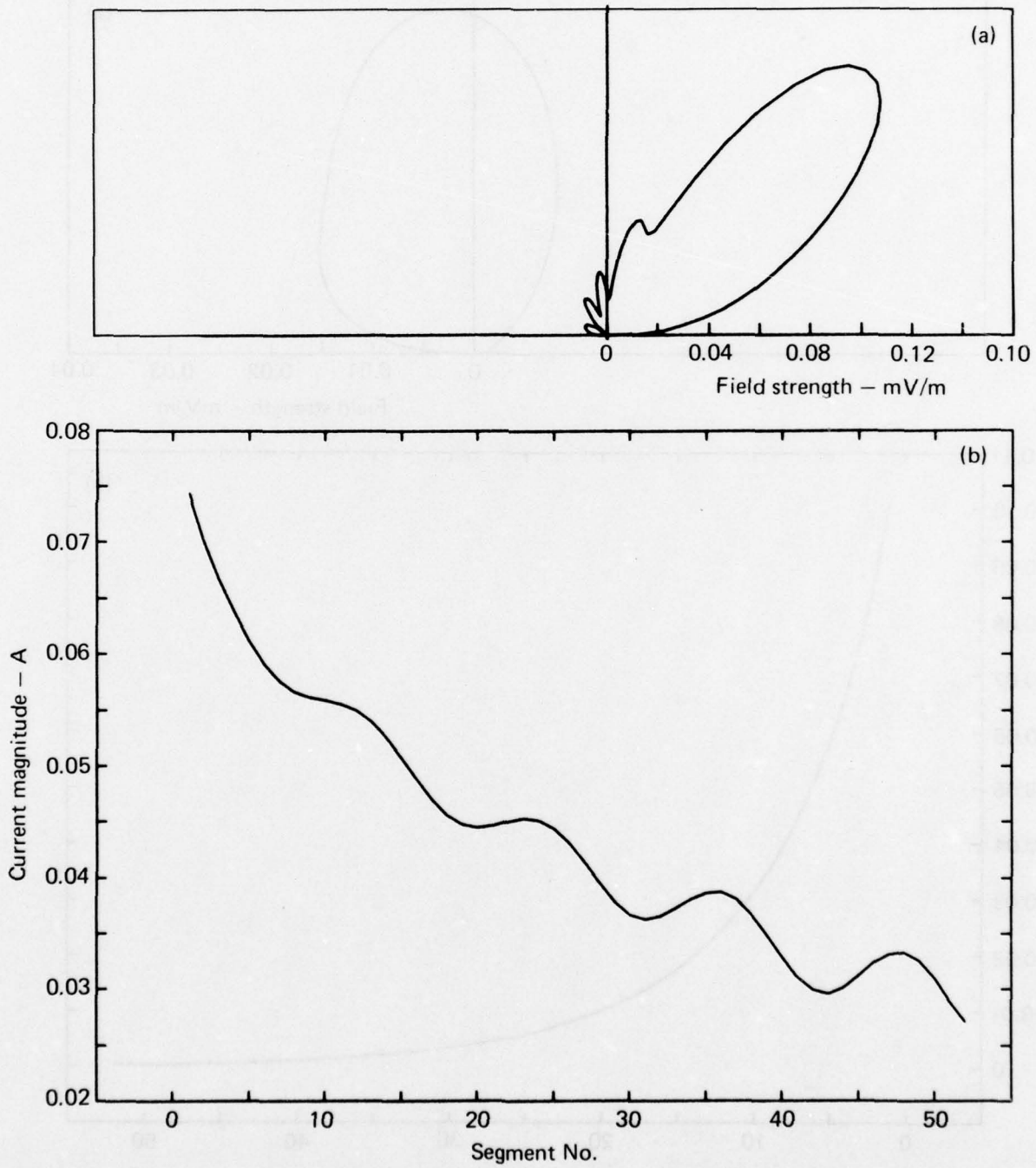

Fig. A14. Results from a vertical half-rhombic antenna: (a) radiation pattern; (b) magnitude of the current on the antenna. L = 100 m; H_v = 5 m; freq = 8 MHz; R_{LOAD} = 300 Ω.

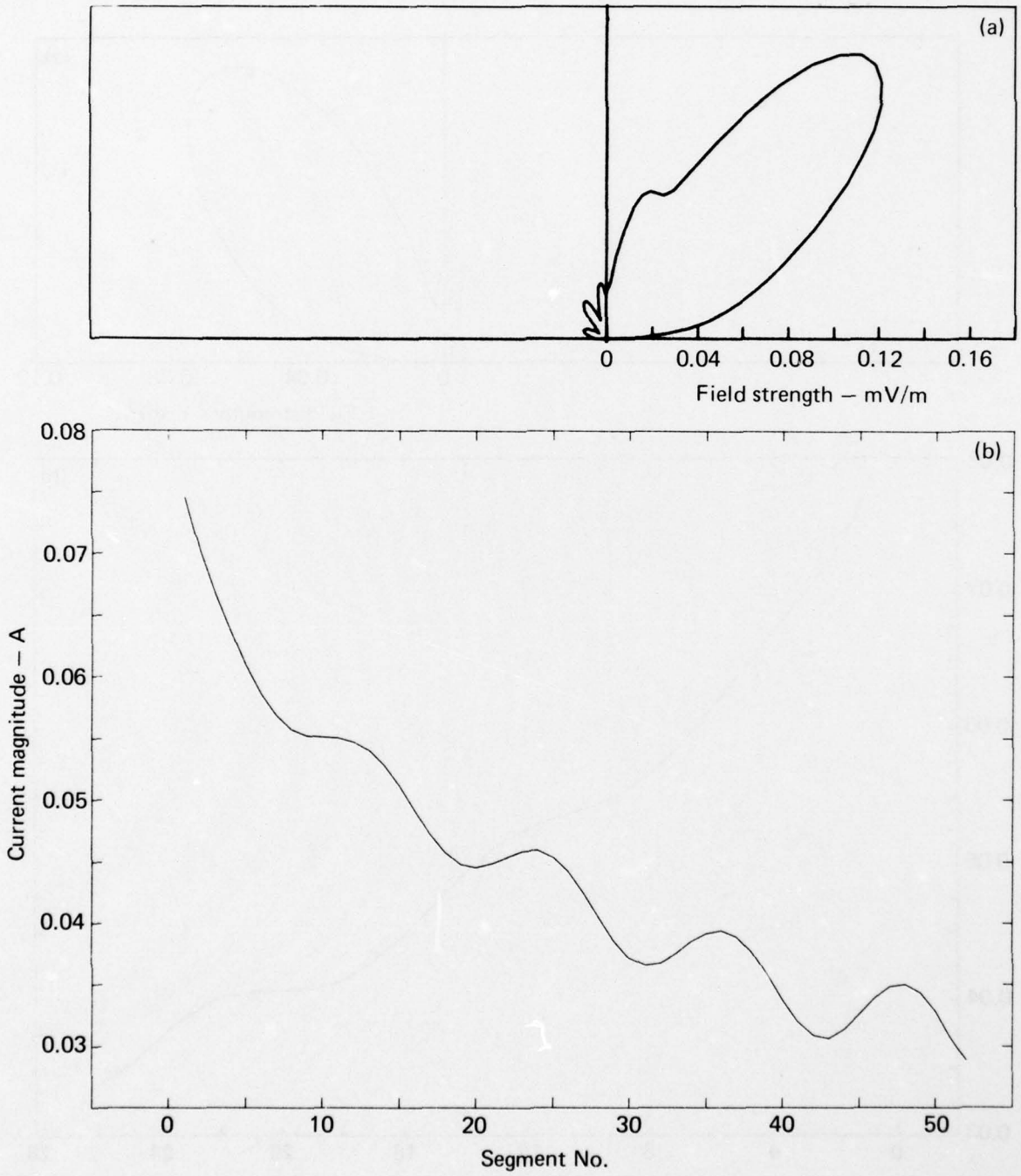

Fig. A15. Results from a vertical half-rhombic antenna: (a) radiation pattern; (b) magnitude of the current on the antenna. L = 100 m; H_v = 10 m; freq = 8 MHz; R_{LOAD} = 300 Ω.

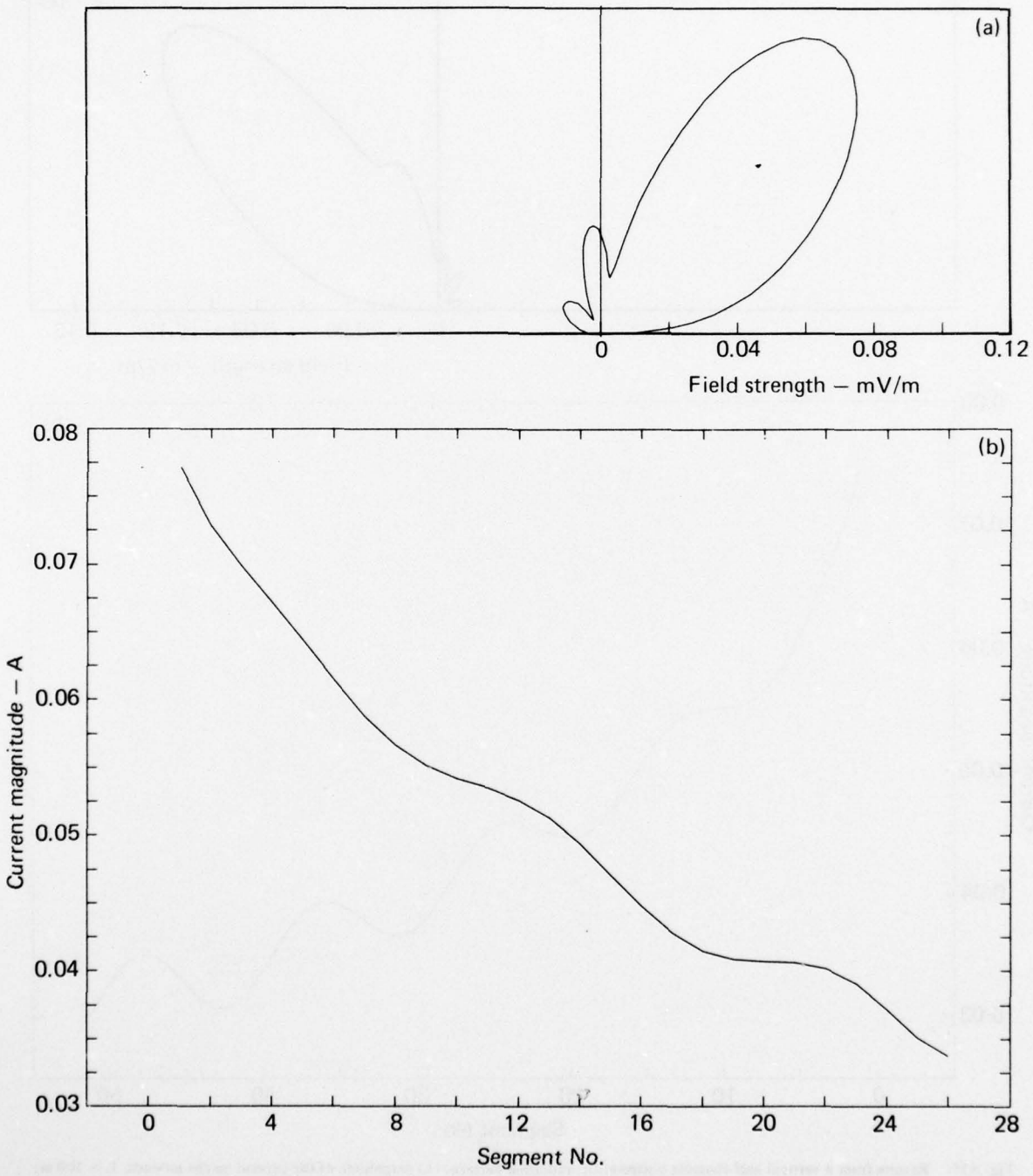

Fig. A16. Results from a vertical half-rhombic antenna: (a) radiation pattern; (b) magnitude of the current on the antenna. L = 50 m; H_v = 2 m; freq = 10 MHz; R_{LOAD} = 300 Ω.

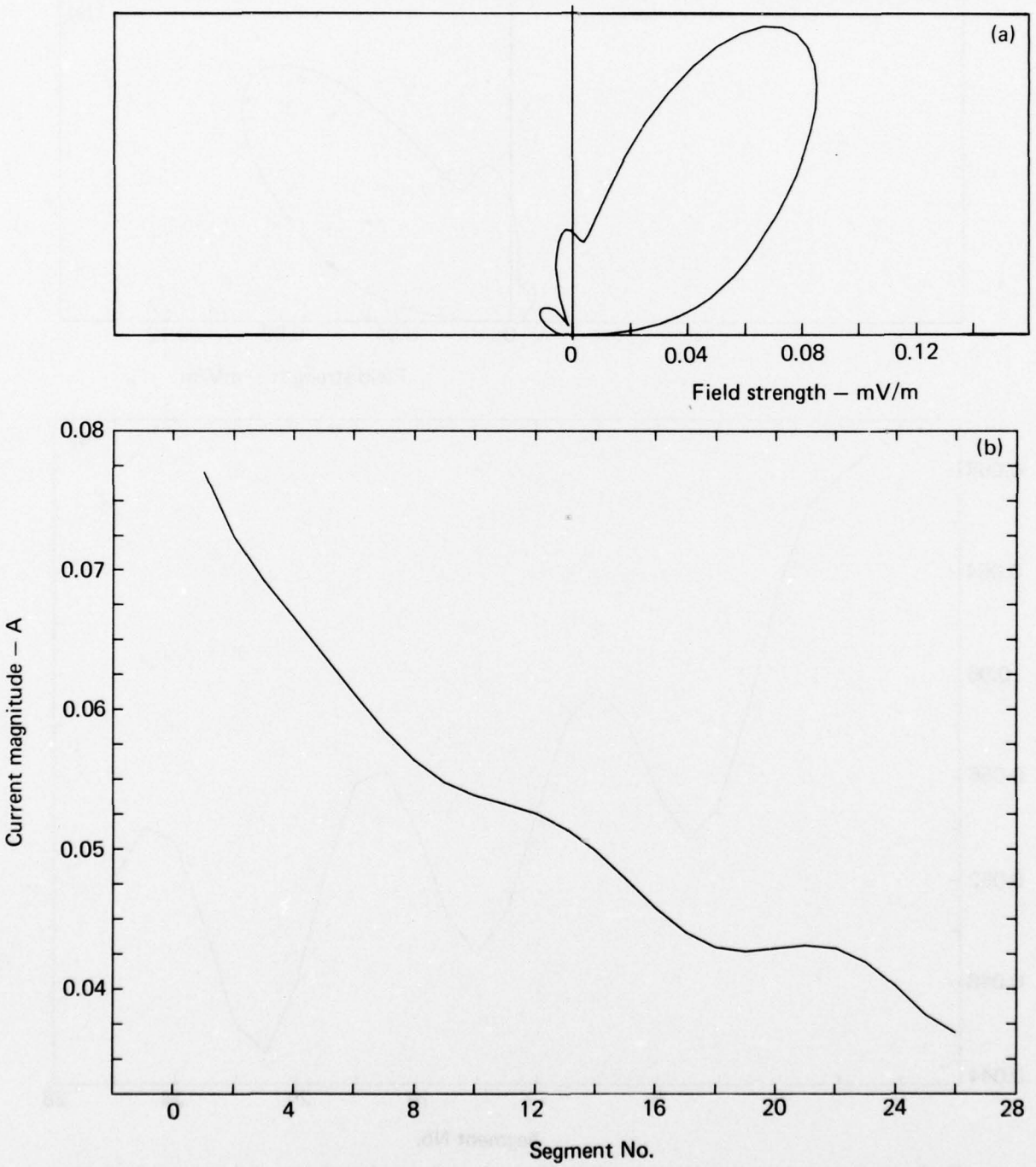

Fig. A17. Results from a vertical half-rhombic antenna: (a) radiation pattern; (b) magnitude of the current on the antenna. L = 50 m; H_v = 5 m; freq = 10 MHz; R_{LOAD} = 300 Ω.

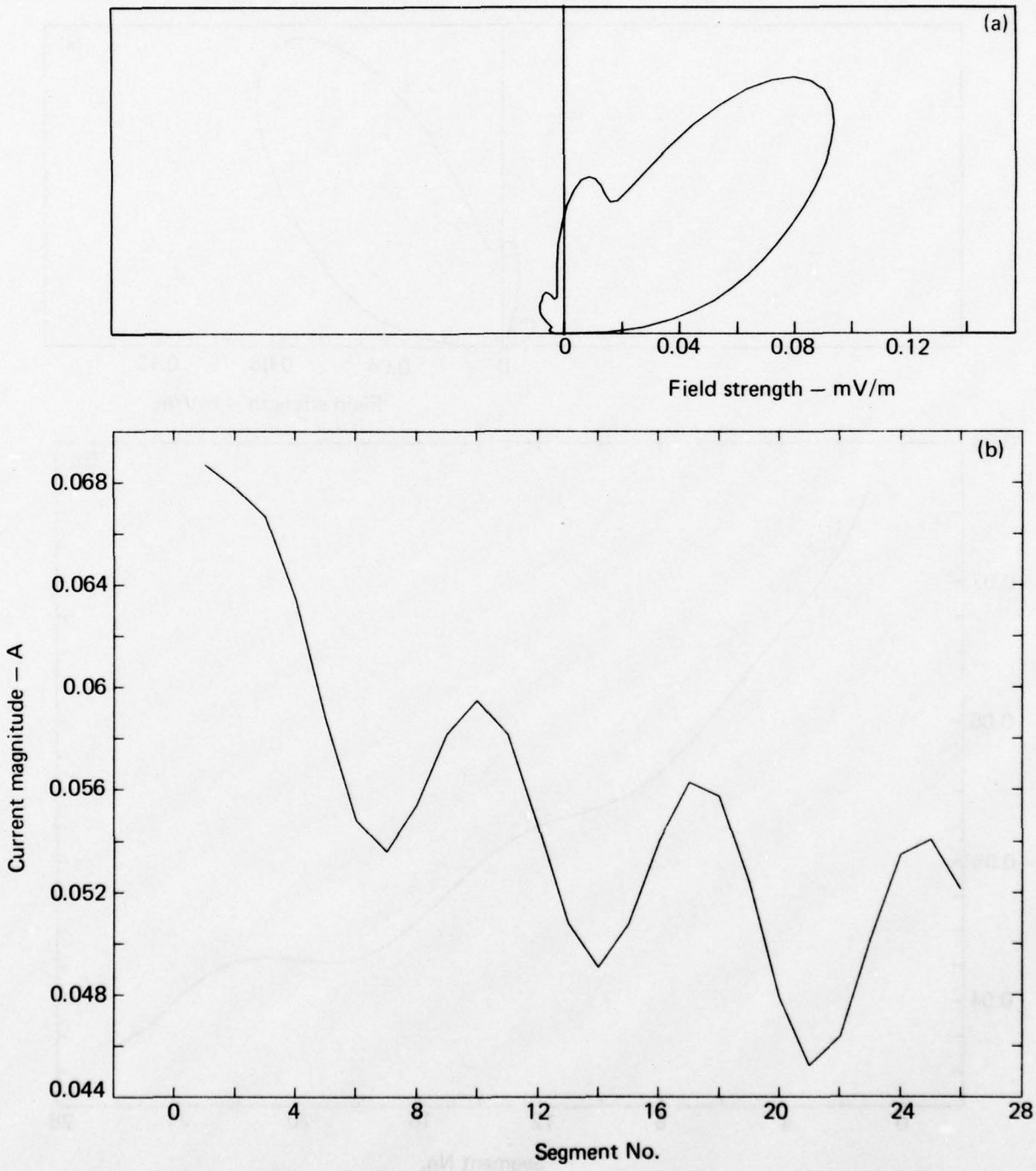

Fig. A18. Results from a vertical half-rhombic antenna: (a) radiation pattern; (b) magnitude of the current on the antenna. L = 50 m; H_v = 10 m; freq = 10 MHz; R_{LOAD} = 300 Ω.

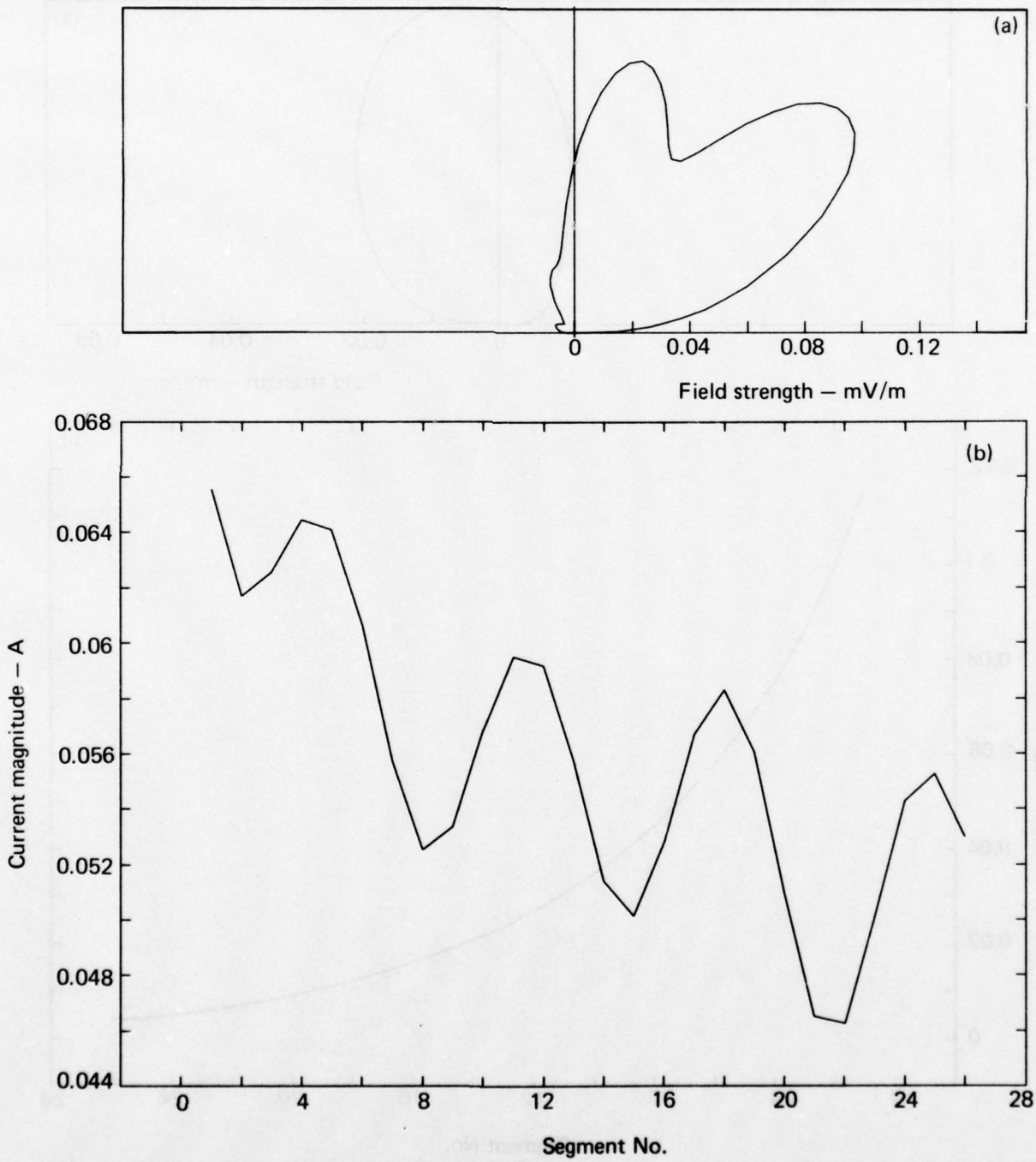

Fig. A19. Results from a vertical half-rhombic antenna: (a) radiation pattern; (b) magnitude of the current on the antenna. L = 50 m; H_v = 15 m; freq = 10 MHz; R_{LOAD} = 300 Ω.

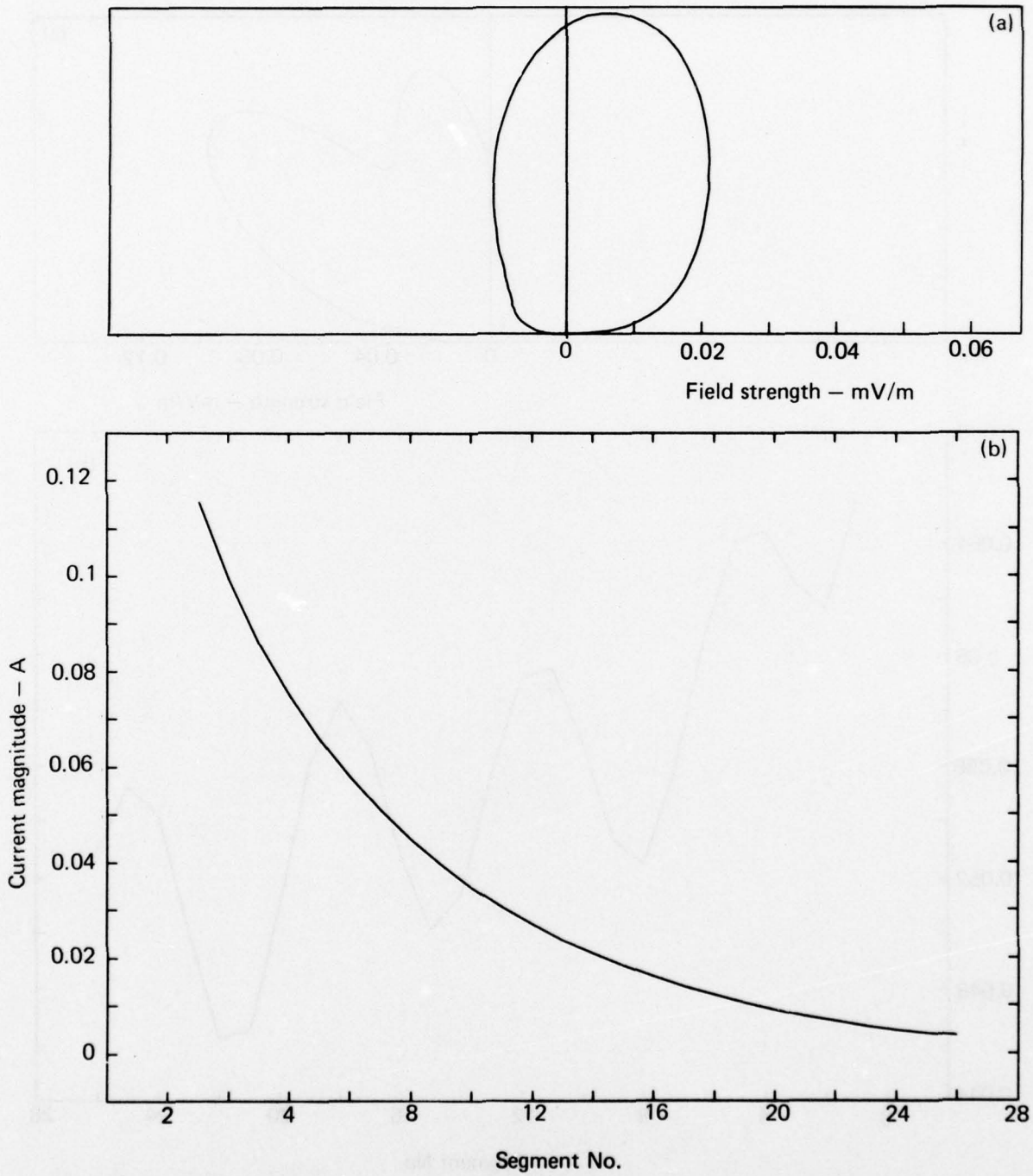

Fig. A20. Results from a vertical half-rhombic antenna: (a) radiation pattern; (b) magnitude of the current on the antenna. L = 50 m; H_v = 2 m; freq = 6 MHz; R_{LOAD} = 300 Ω.

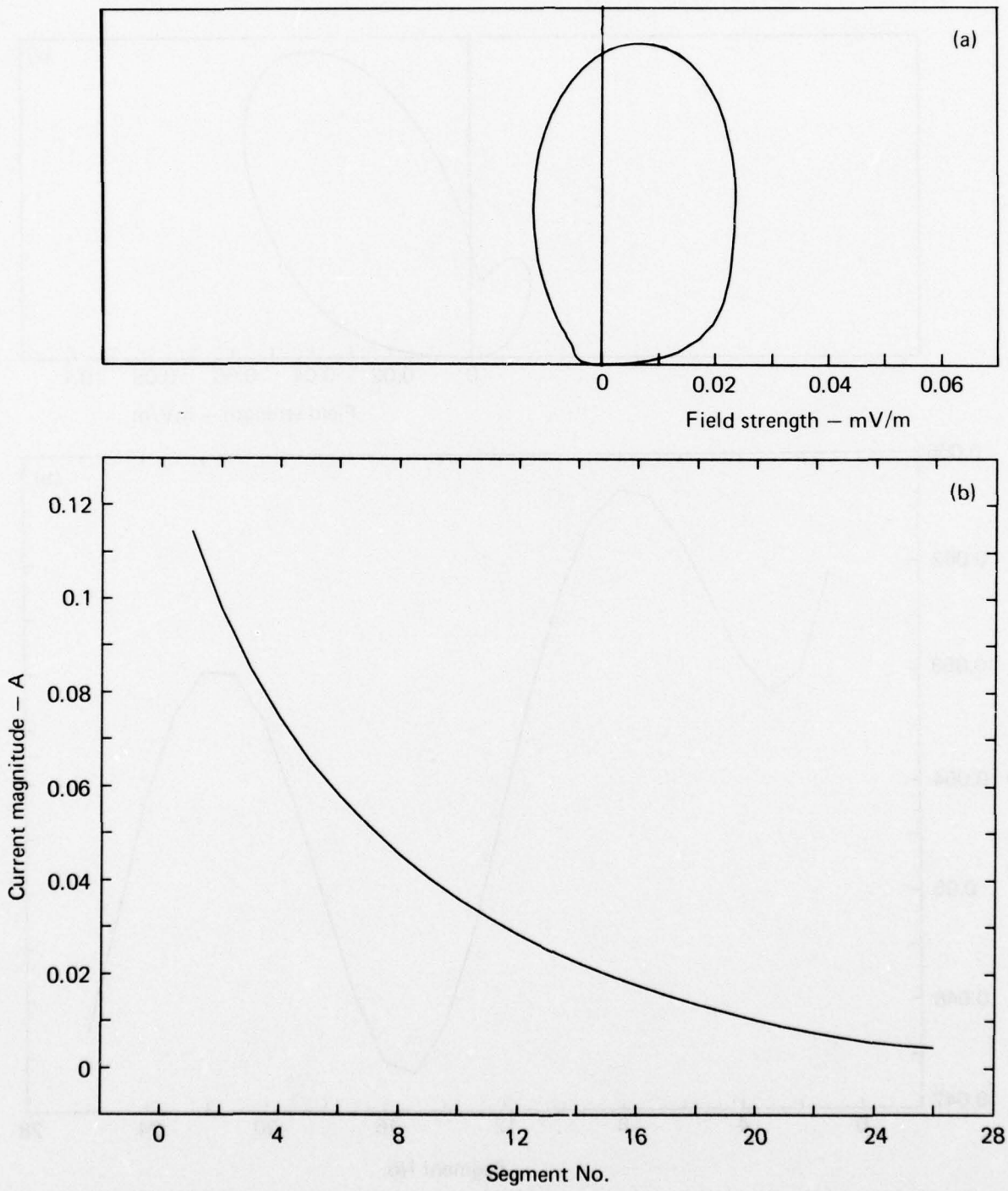

Fig. A21. Results from a vertical half-rhombic antenna: (a) radiation pattern; (b) magnitude of the current on the antenna. L = 50 m; H_v = 5 m; freq = 6 MHz; R_{LOAD} = 300 Ω.

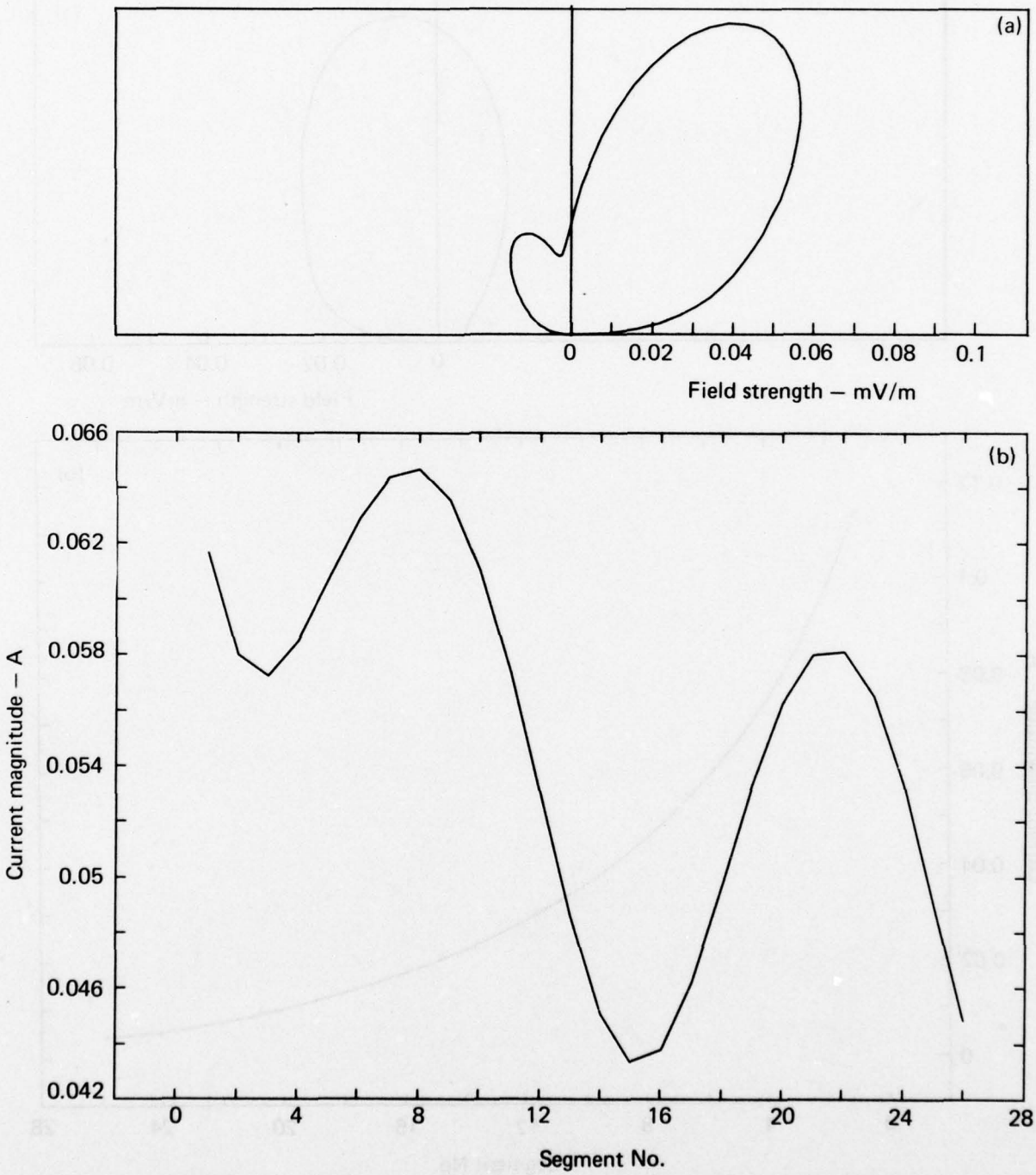

Fig. A22. Results from a vertical half-rhombic antenna: (a) radiation pattern; (b) magnitude of the current on the antenna. L = 50 m; H_v = 10 m; freq = 6 MHz; R_{LOAD} = 300 Ω.

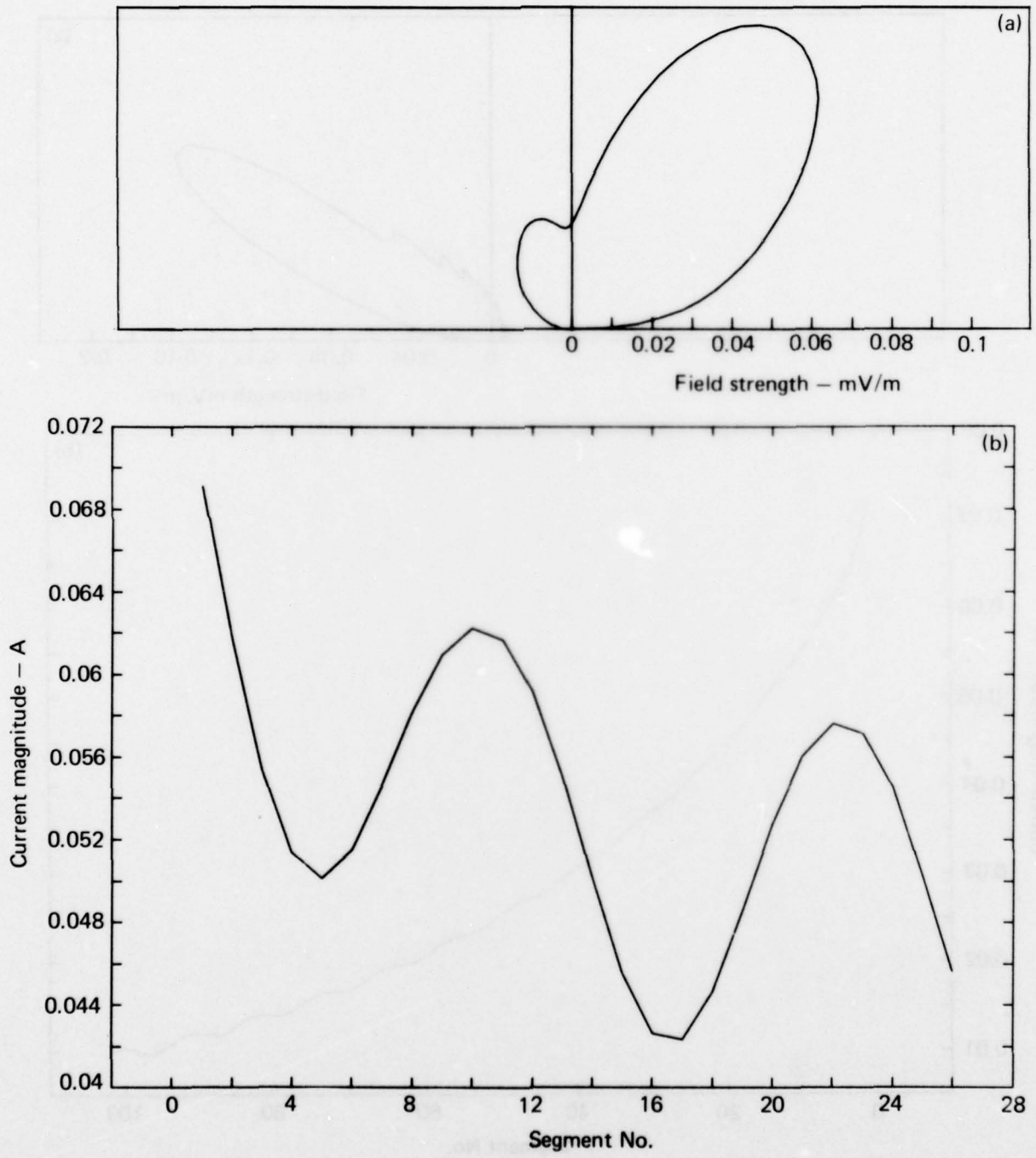

Fig. A23. Results from a vertical half-rhombic antenna: (a) radiation pattern; (b) magnitude of the current on the antenna. L = 50 m; H_v = 15 m; freq = 6 MHz; R_{LOAD} = 300 Ω.

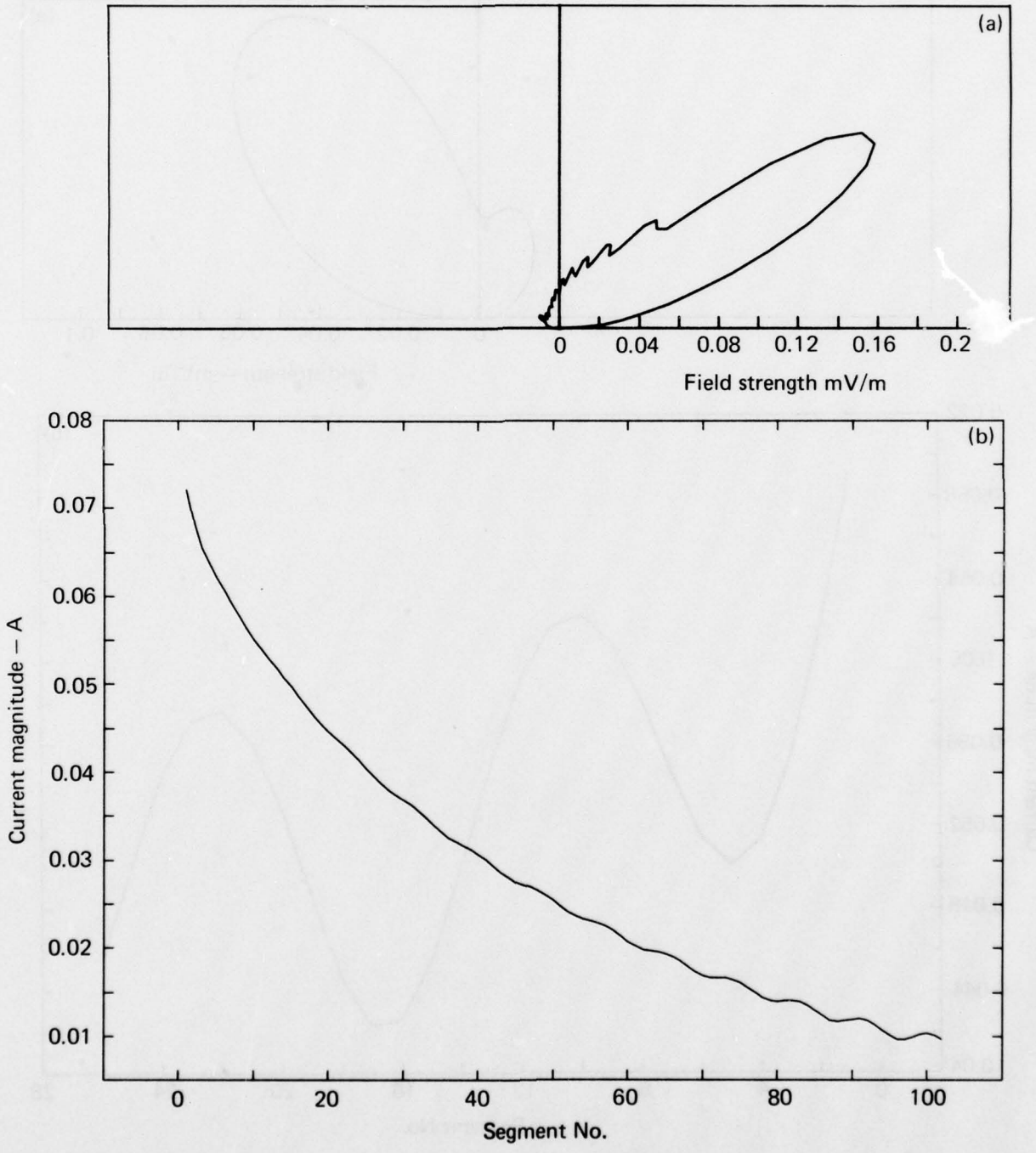

Fig. A24. Results from a vertical half-rhombic antenna: (a) radiation pattern; (b) magnitude of the current on the antenna. L = 200 m; H_v = 2 m; freq = 10 MHz; R_{LOAD} = 300 Ω.

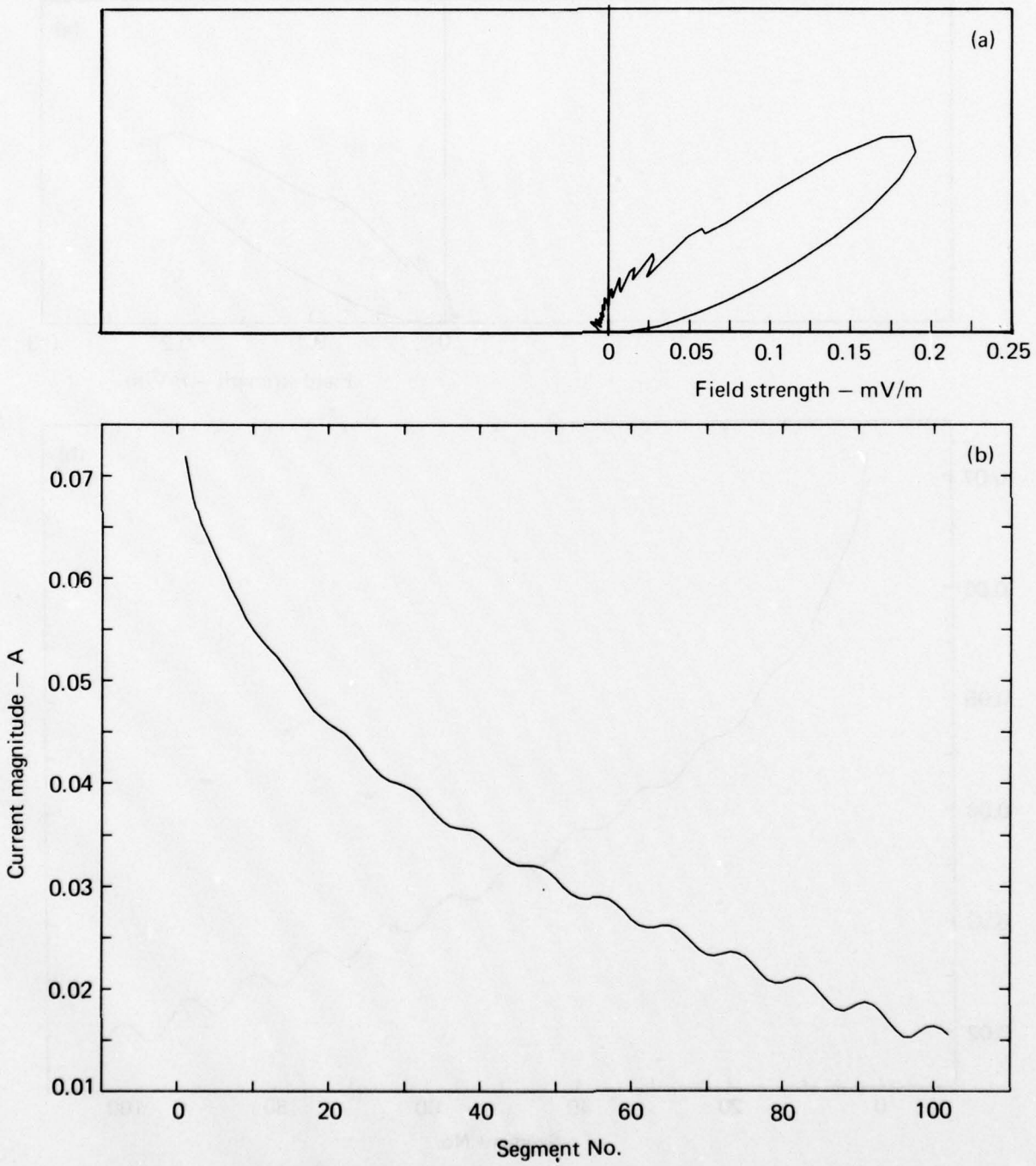

Fig. A25. Results from a vertical half-rhombic antenna: (a) radiation pattern; (b) magnitude of the current on the antenna. L = 200 m; H_v = 5 m; freq = 10 MHz; R_{LOAD} = 300 Ω.

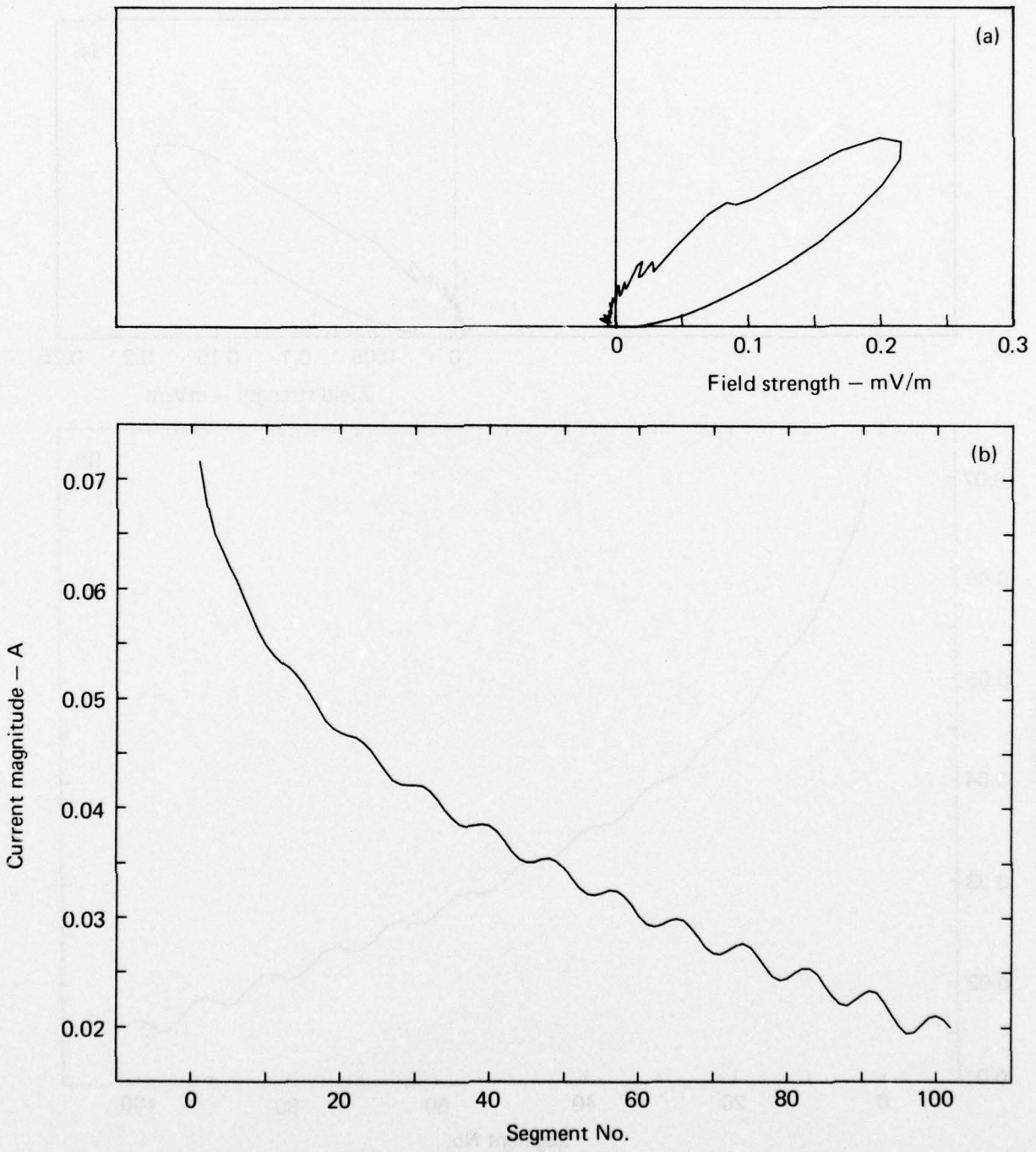

Fig. A26. Results from a vertical half-rhombic antenna: (a) radiation pattern; (b) magnitude of the current on the antenna. L = 200 m; H_v = 10 m; freq = 10 MHz; R_{LOAD} = 300 Ω.

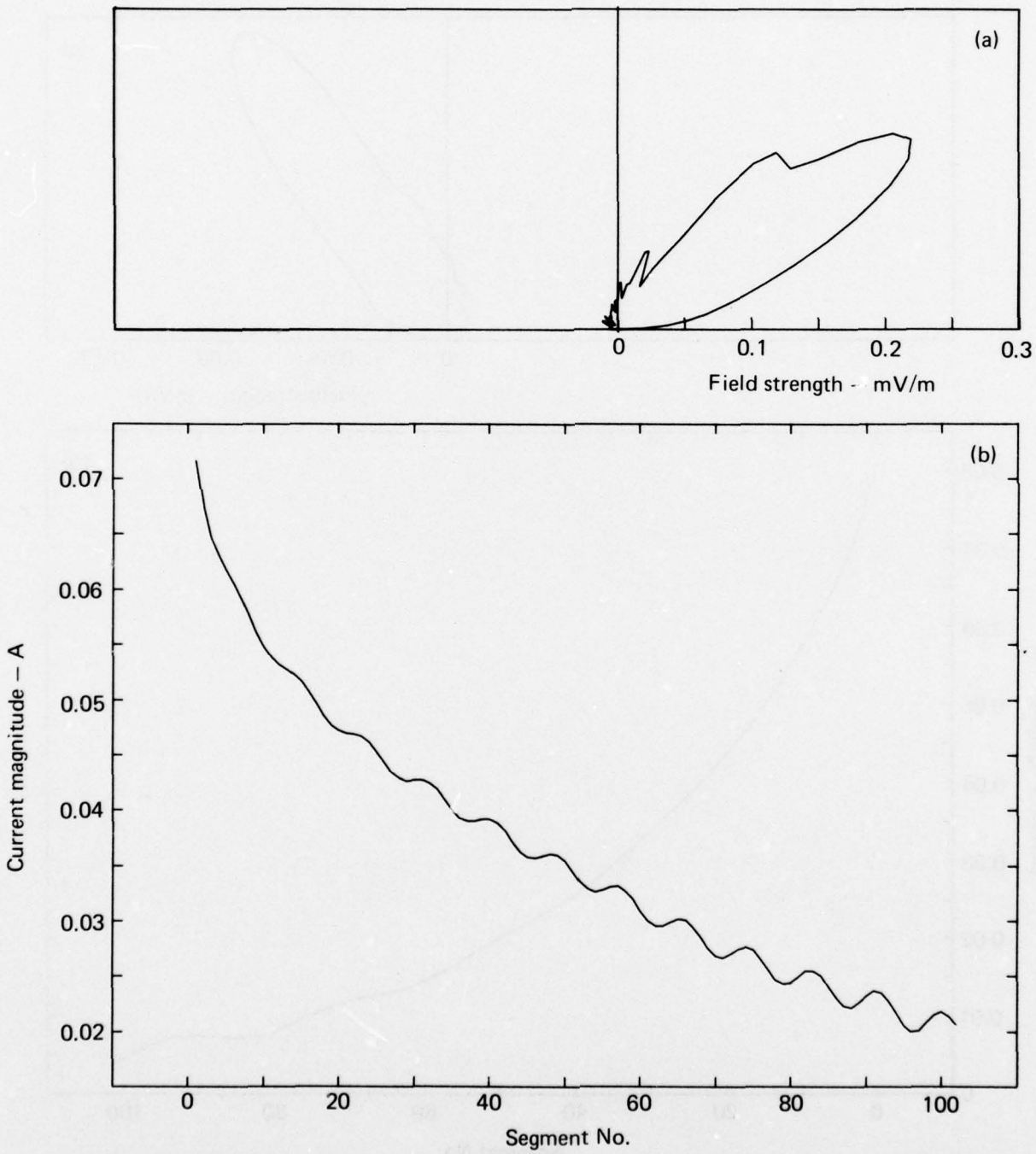

Fig. A27. Results from a vertical half-rhombic antenna: (a) radiation pattern; (b) magnitude of the current on the antenna. L = 200 m; H_v = 15 m; freq = 10 MHz; R_{LOAD} = 300 Ω.

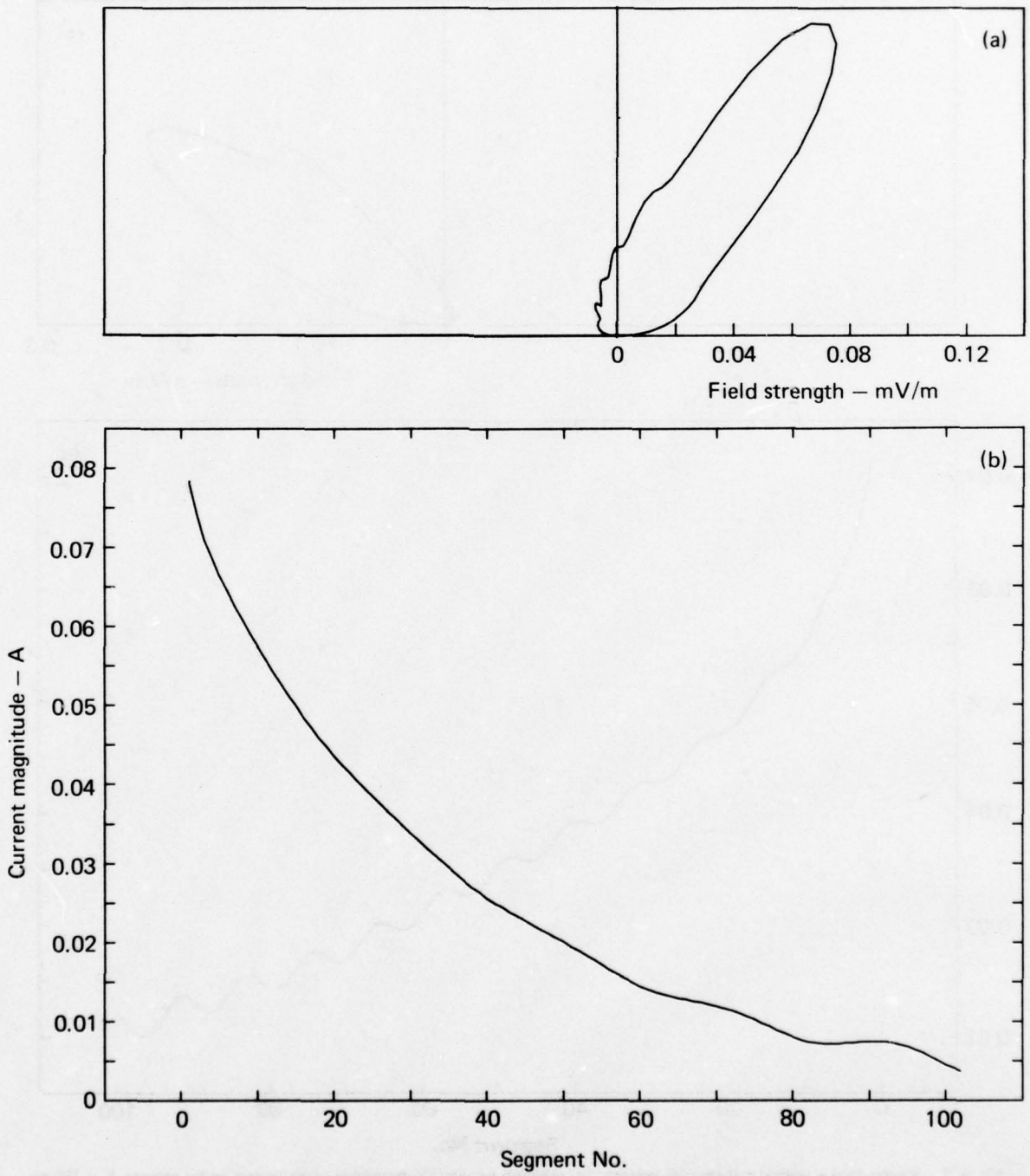

Fig. A28. Results from a vertical half-rhombic antenna: (a) radiation pattern; (b) magnitude of the current on the antenna. L = 200 m; H_v = 2 m; freq = 6 MHz; R_{LOAD} = 300 Ω.

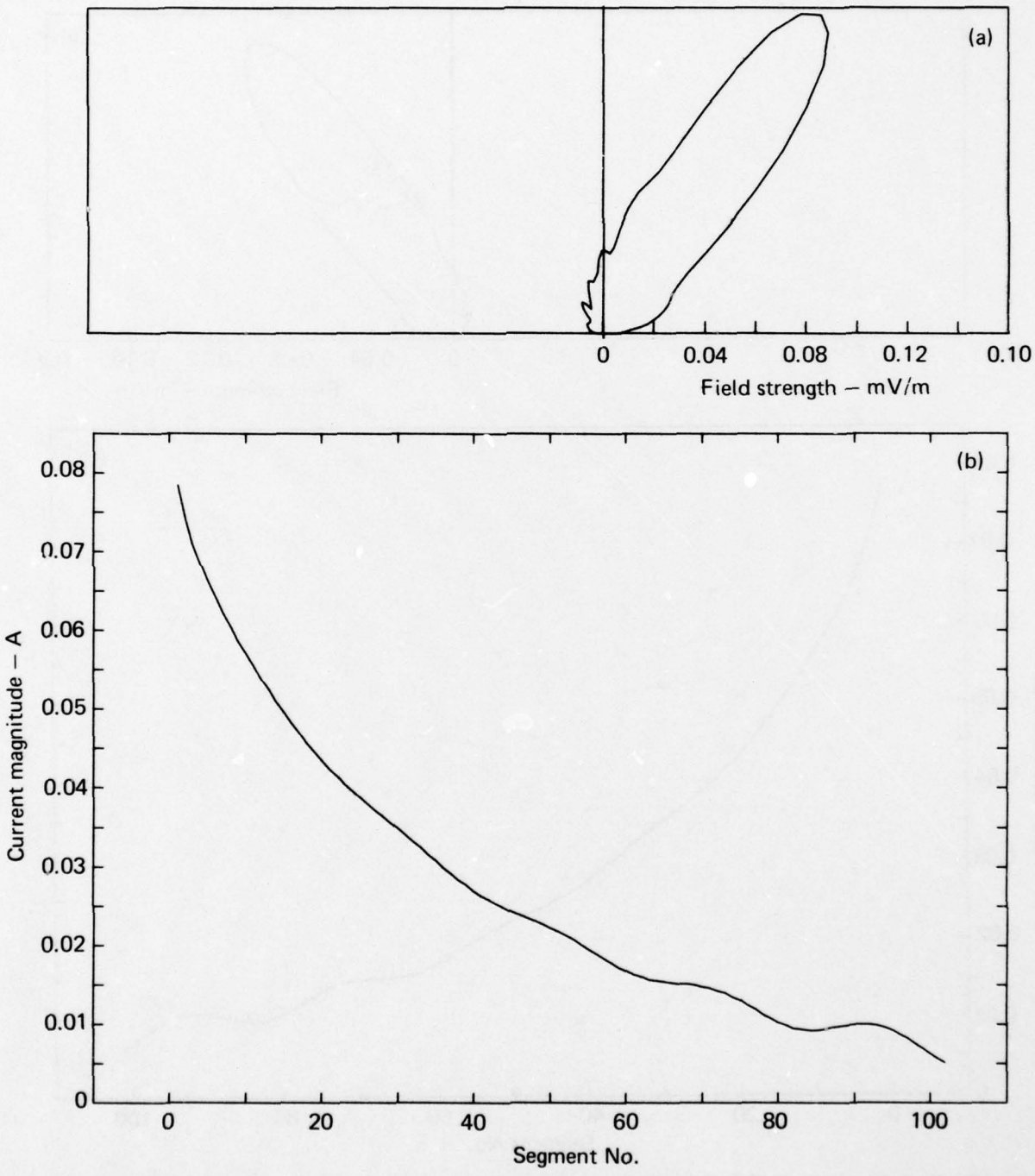

Fig. A29. Results from a vertical half-rhombic antenna: (a) radiation pattern; (b) magnitude of the current on the antenna. L = 200 m; H_v = 5 m; freq = 6 MHz; R_{LOAD} = 300 Ω.

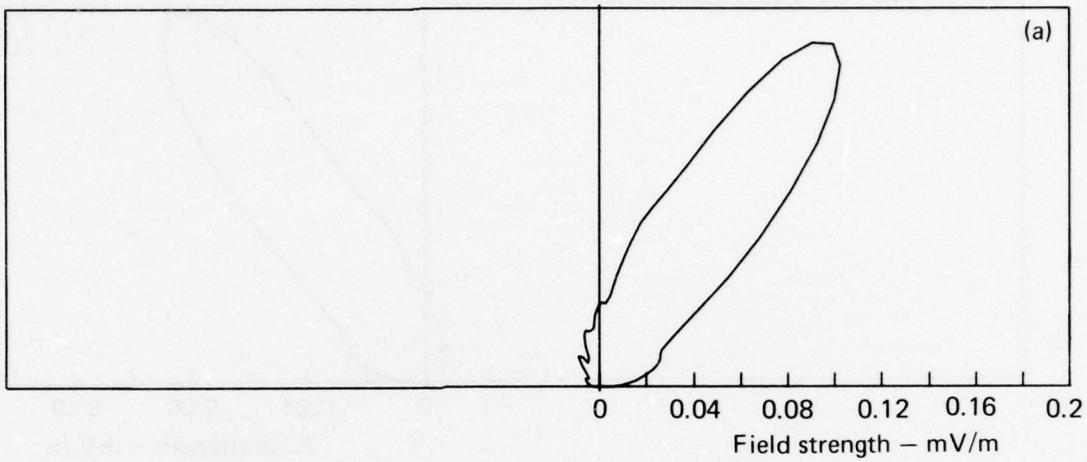

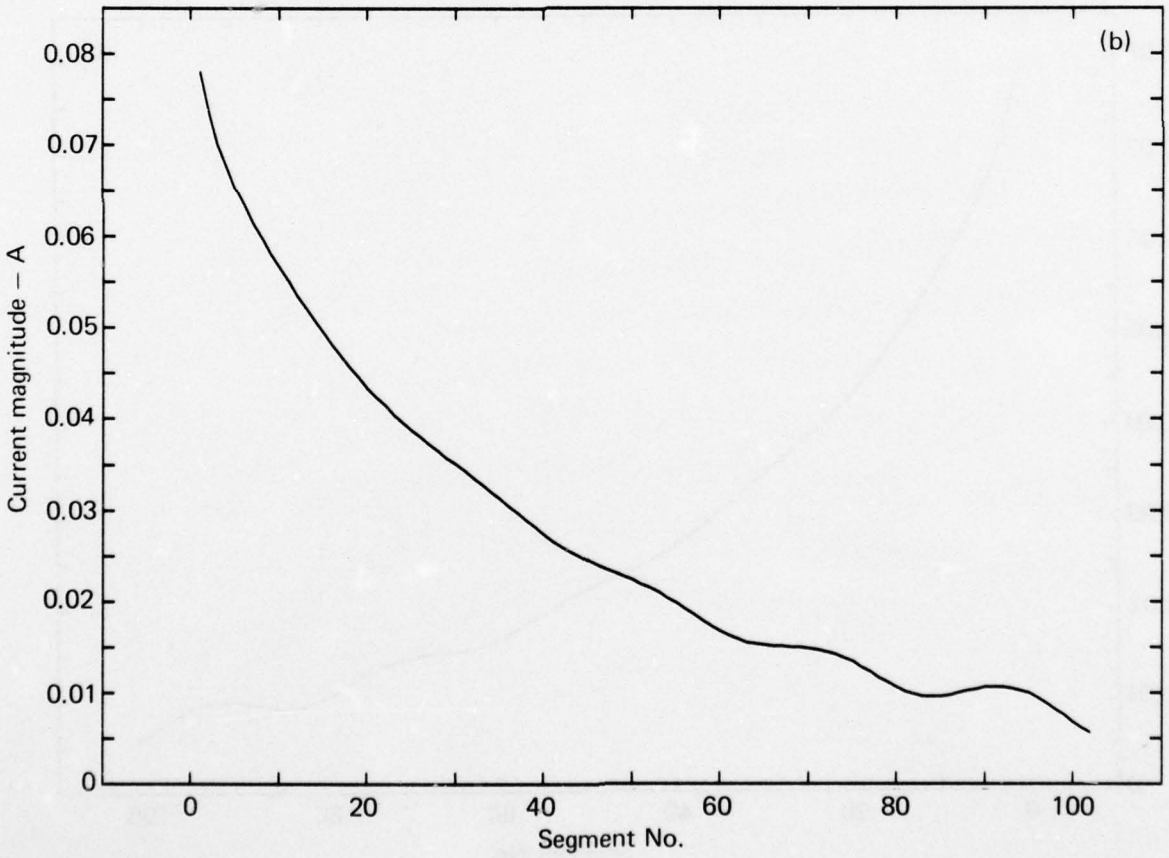

Fig. A30. Results from a vertical half-rhombic antenna: (a) radiation pattern; (b) magnitude of the current on the antenna. L = 200 m; H_v = 10 m; freq = 6 MHz; R_{LOAD} = 300 Ω.

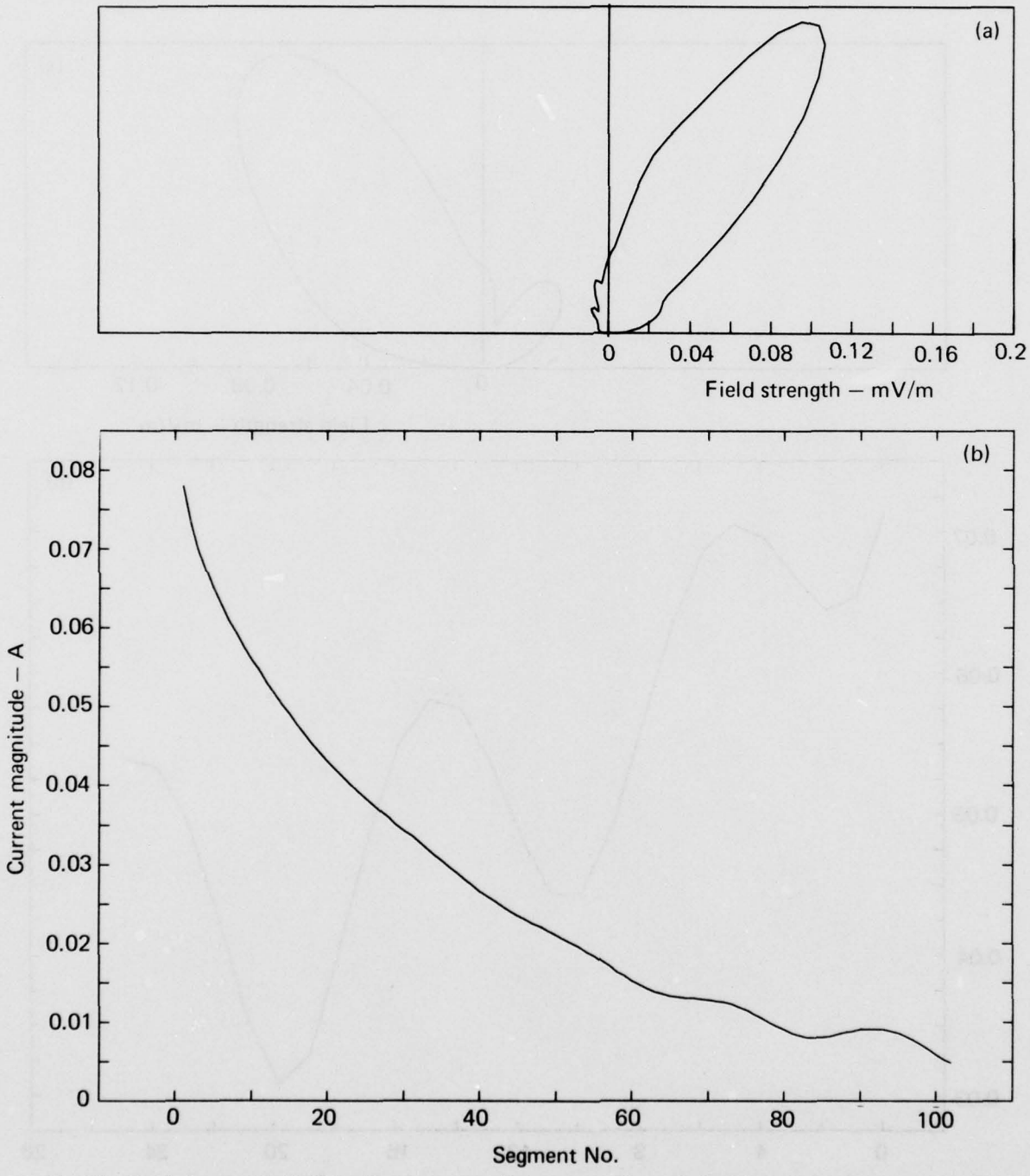

Fig. A31. Results from a vertical half-rhombic antenna: (a) radiation pattern; (b) magnitude of the current on the antenna. L = 200 m; H_v = 15 m; freq = 6 MHz; R_{LOAD} = 300 Ω.

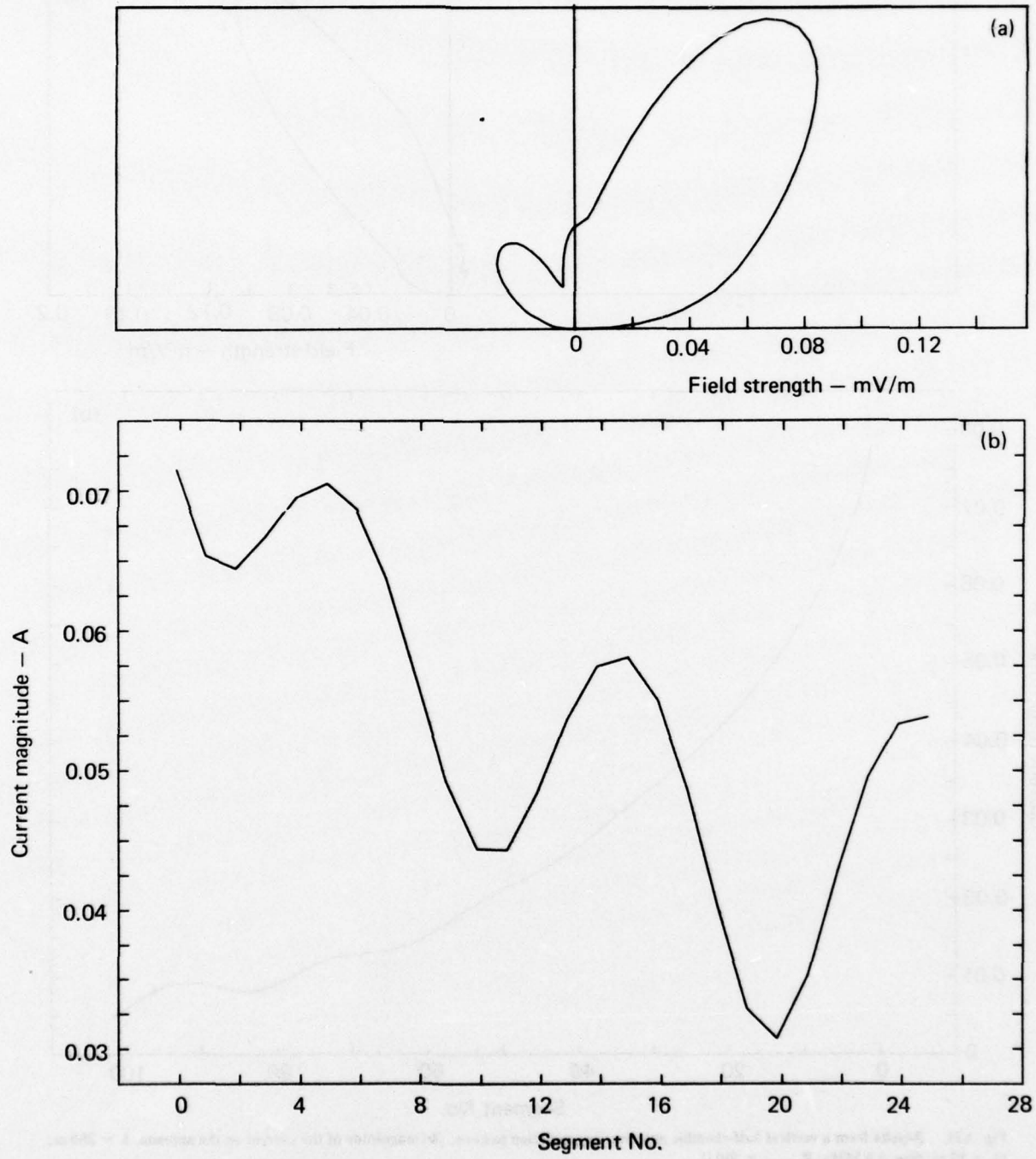

Fig. A32. Results from a vertical half-rhombic antenna: (a) radiation pattern; (b) magnitude of the current on the antenna. L = 50 m; H_v = 5 m; freq = 10 MHz; R_{LOAD} = 100 Ω.

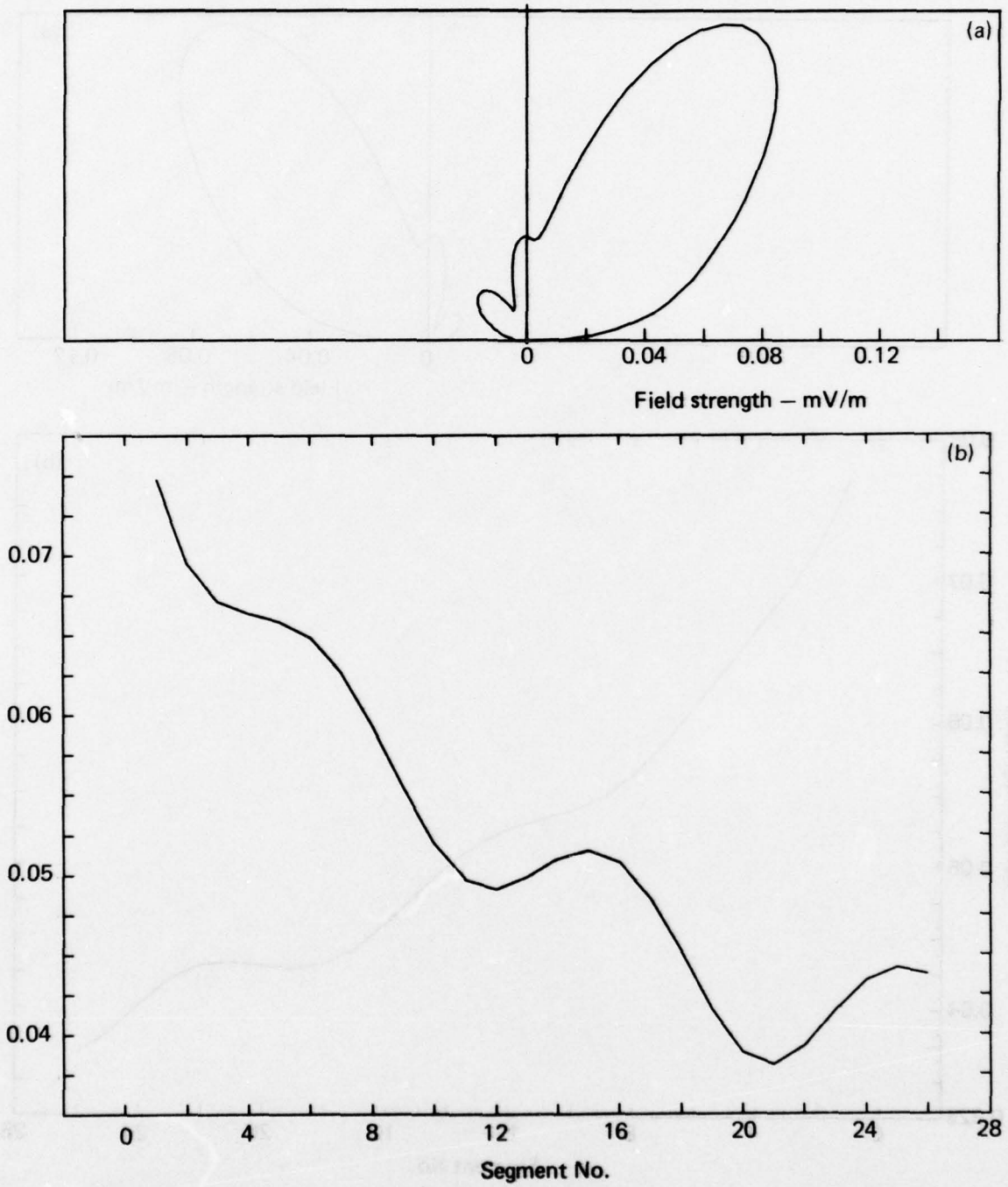

Fig. A33. Results from a vertical half-rhombic antenna: (a) radiation pattern; (b) magnitude of the current on the antenna. L = 50 m; H_v = 5 m; freq = 10 MHz; R_{LOAD} = 200 Ω.

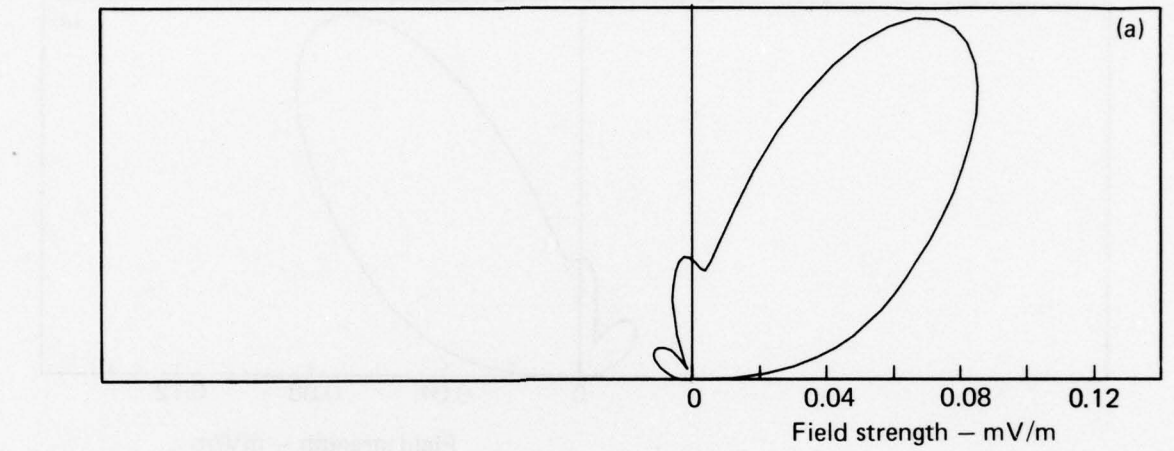

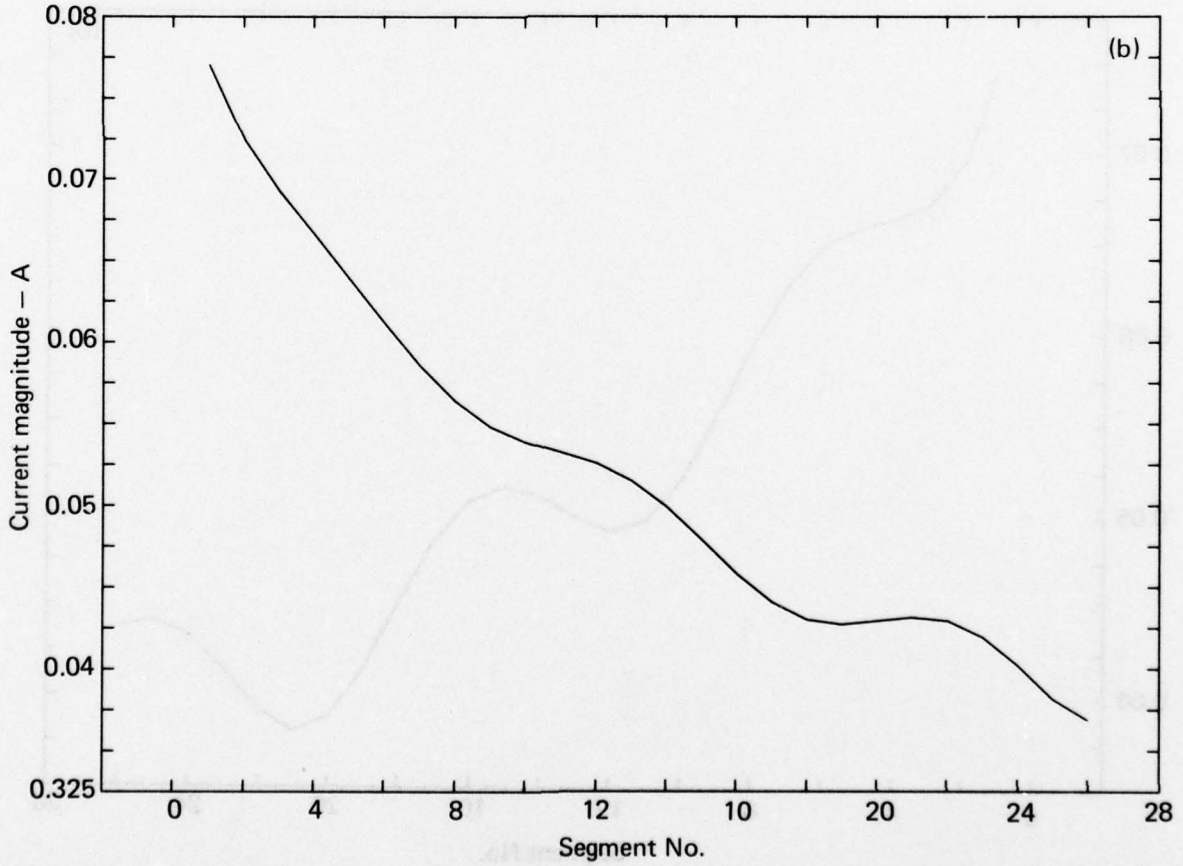

Fig. A34. Results from a vertical half-rhombic antenna: (a) radiation pattern; (b) magnitude of the current on the antenna. L = 50 m; H_v = 5 m; freq = 10 MHz; R_{LOAD} = 300 Ω.

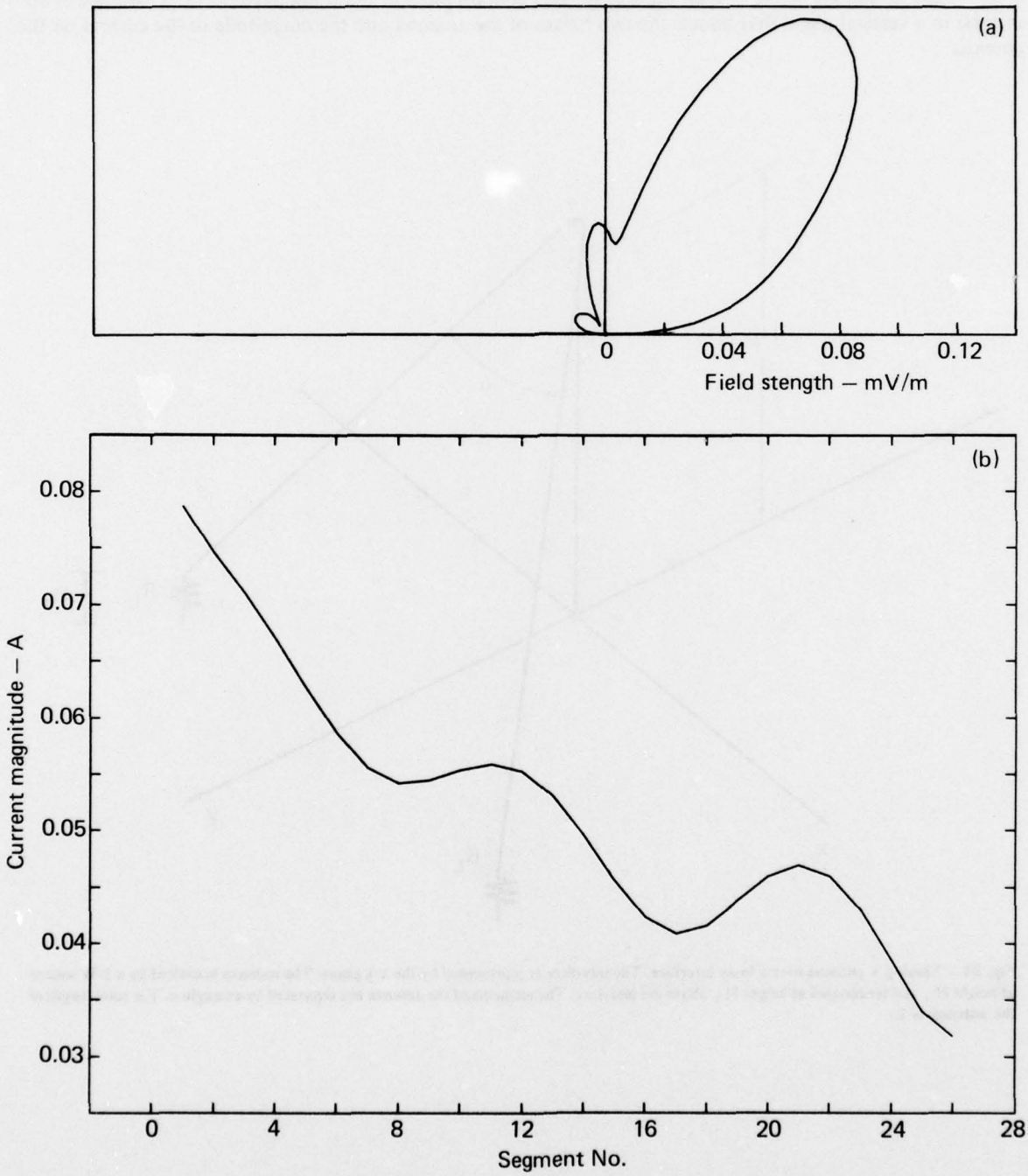

Fig. A35. Results from a vertical half-rhombic antenna: (a) radiation pattern; (b) magnitude of the current on the antenna. L = 50 m; H_v = 5 m; freq = 10 MHz; R_{LOAD} = 400 Ω.

APPENDIX B. RESULTS FOR A SLOPING V ANTENNA

The sloping V antenna is shown in Fig. B1. All data shown in this appendix are for $\sigma = 10^{-3}$ mho/m, $\epsilon_r = 4$, $R_L = 300\ \Omega$, and $H_L = H_S = 2$ m. Figures B2-B23 contain plots of radiation patterns (at a distance of 10^5 meters) in a vertical plane that bisects the two halves of the antenna and the magnitude of the current on the antenna.

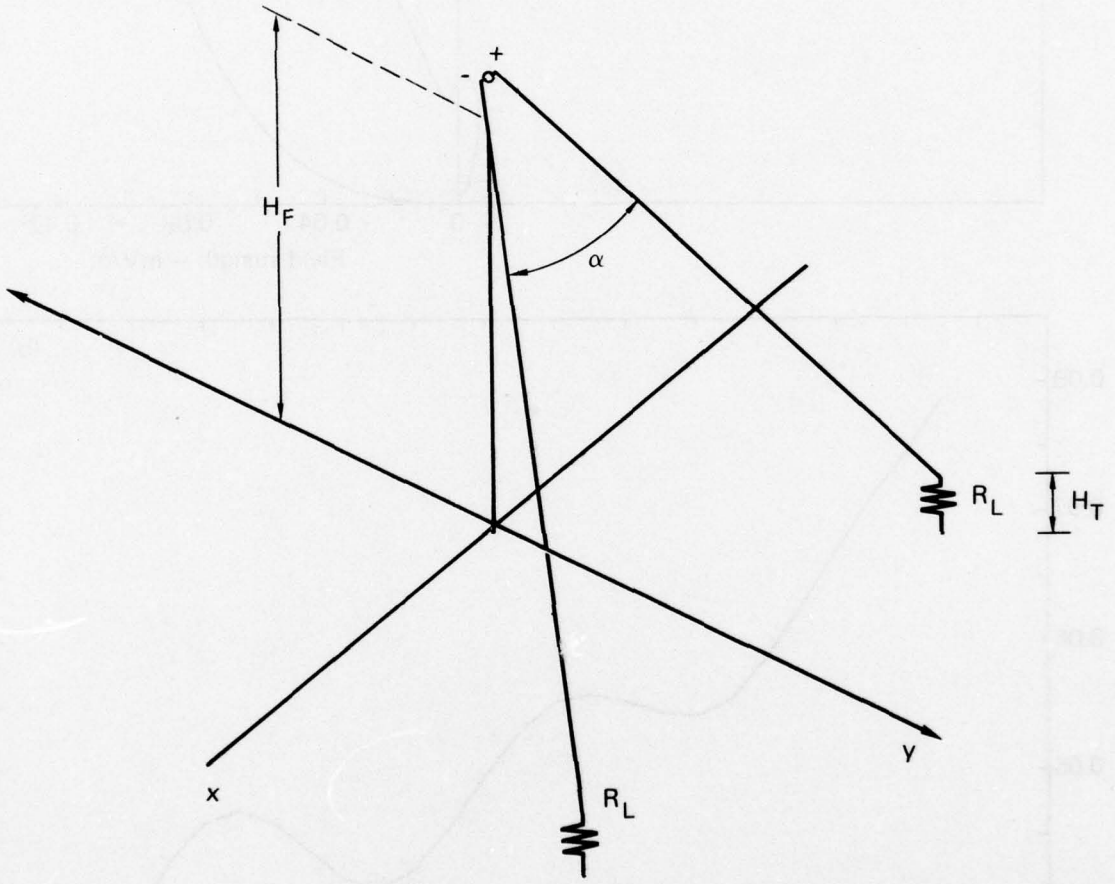

Fig. B1. Sloping V antenna over a lossy interface. The interface is represented by the x-y plane. The antenna is excited by a 1-W source at height H_F and terminated at height H_T above the interface. The elements of the antenna are separated by an angle α. The total length of the antenna is L.

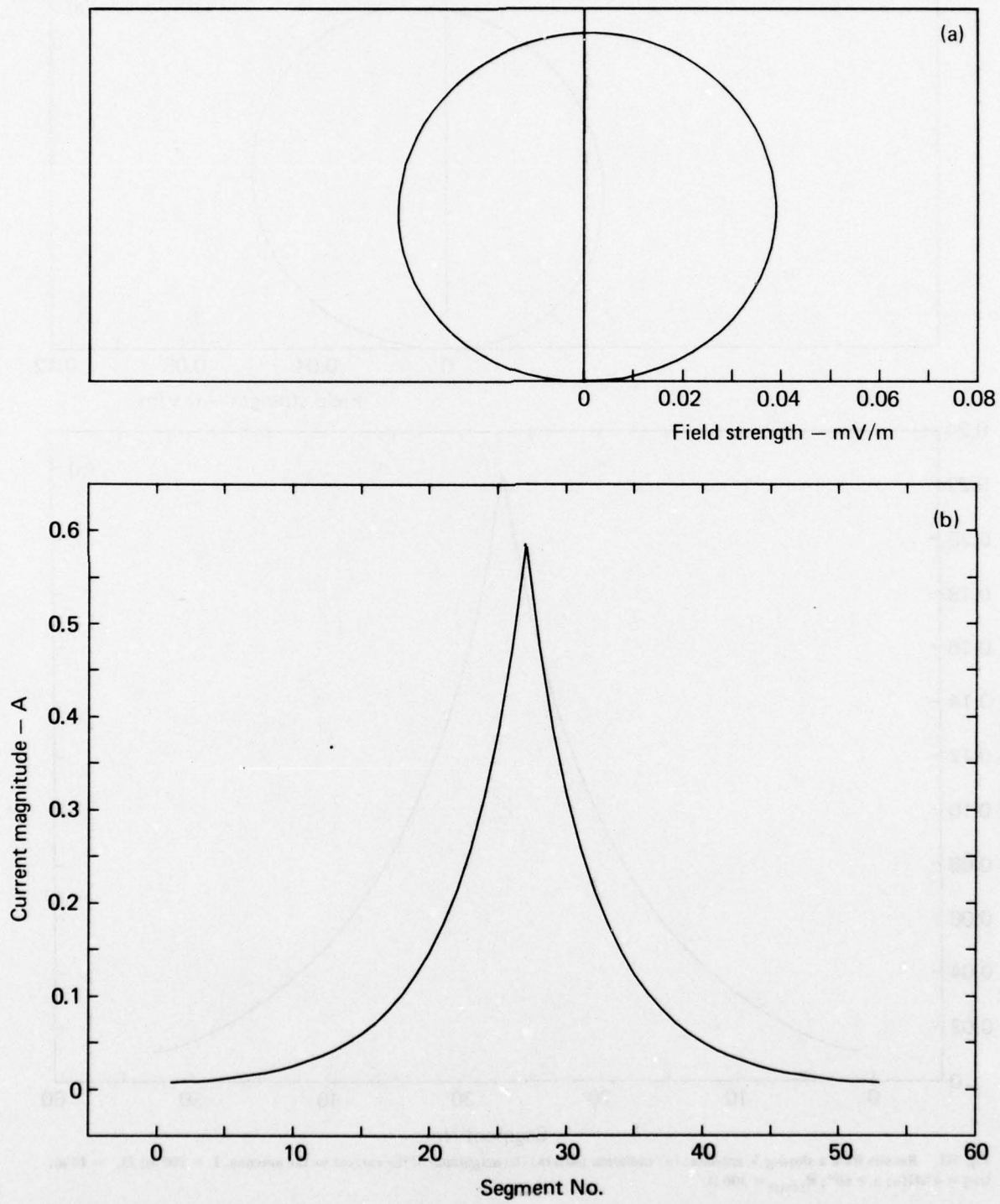

Fig. B2. Results from a sloping V antenna: (a) radiation pattern; (b) magnitude of the current on the antenna. L = 100 m; H_F = 10 m; freq = 2 MHz; α = 60°. Note that here and in the following figures, the current is shown on both arms of the antenna with the source in the middle of the diagram.

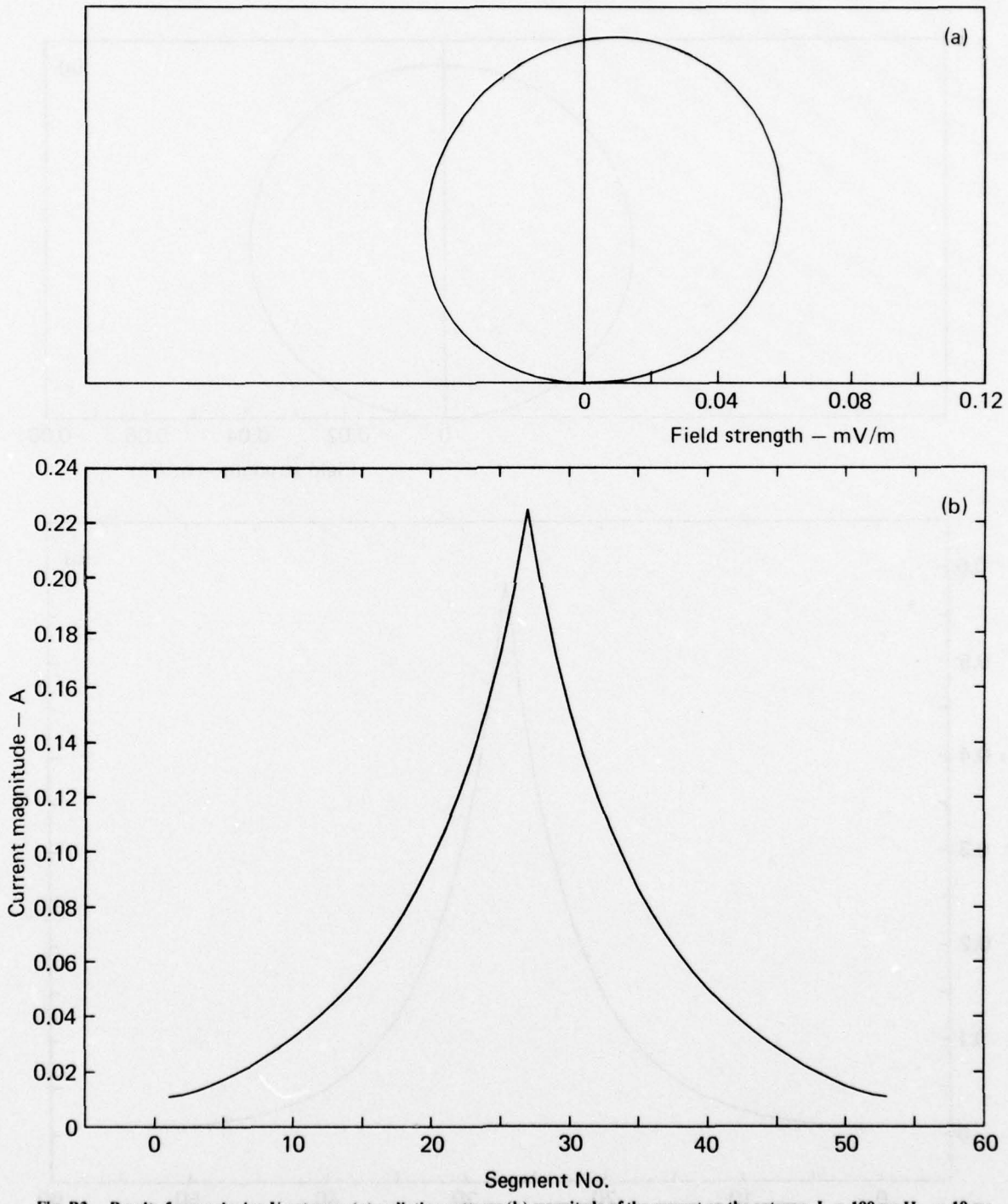

Fig. B3. Results from a sloping V antenna: (a) radiation pattern; (b) magnitude of the current on the antenna. L = 100 m; H_F = 10 m; freq = 4 MHz; $\alpha = 60°$; $R_{LOAD} = 300\ \Omega$.

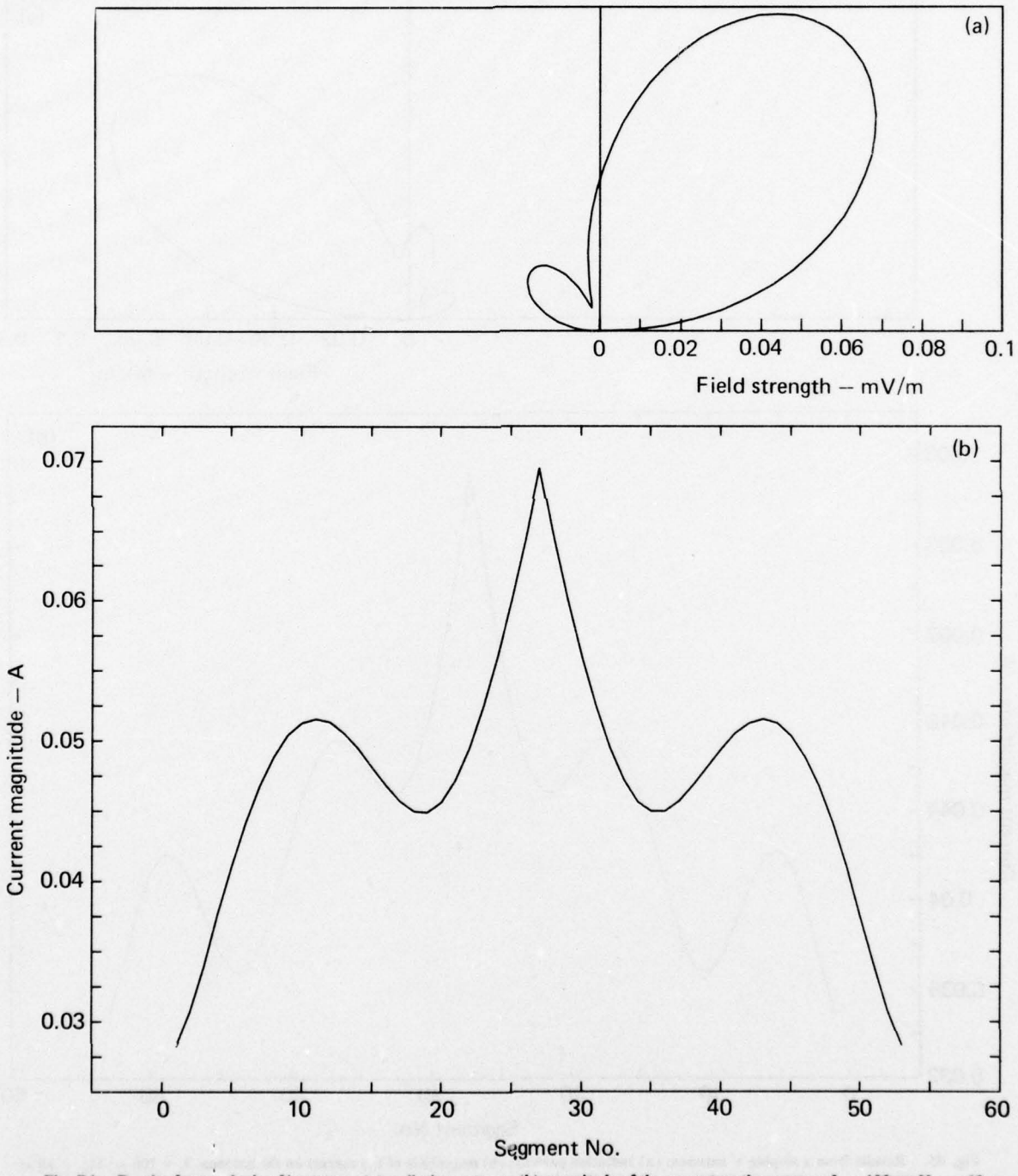

Fig. B4. Results from a sloping V antenna: (a) radiation pattern; (b) magnitude of the current on the antenna. L = 100 m; H_F = 10 m; freq = 6 MHz; $\alpha = 60°$; $R_{LOAD} = 300\ \Omega$.

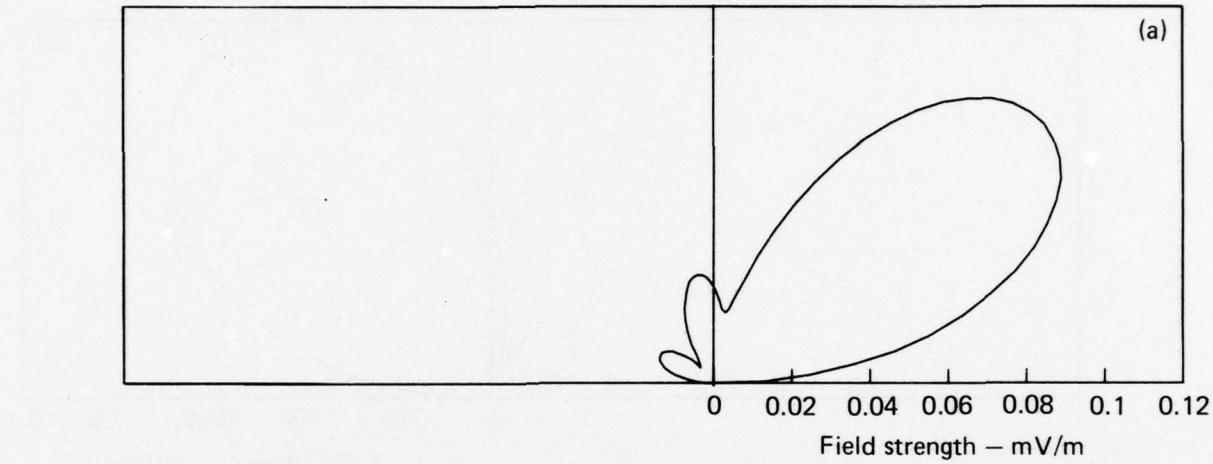

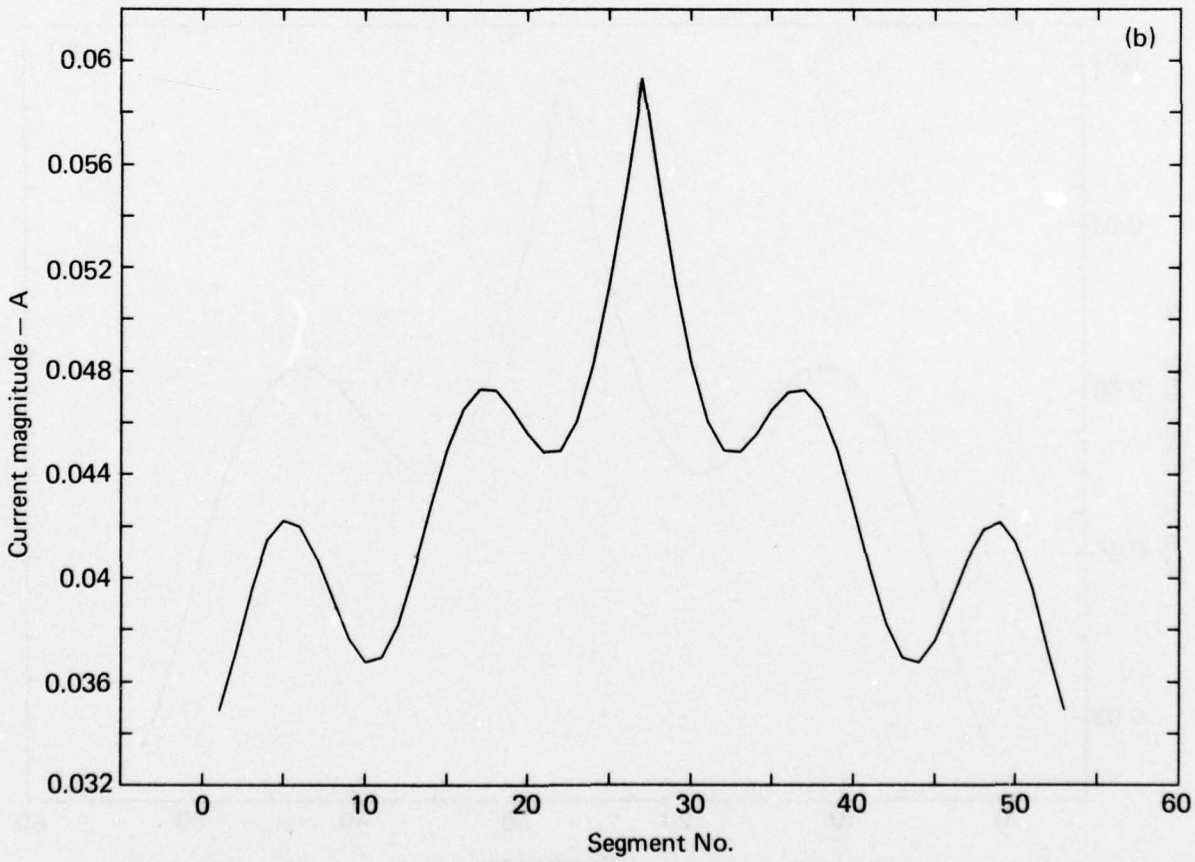

Fig. B5. Results from a sloping V antenna: (a) radiation pattern; (b) magnitude of the current on the antenna. L = 100 m; H_E = 10 m; freq = 8 MHz; $\alpha = 60°$; $R_{LOAD} = 300\ \Omega$.

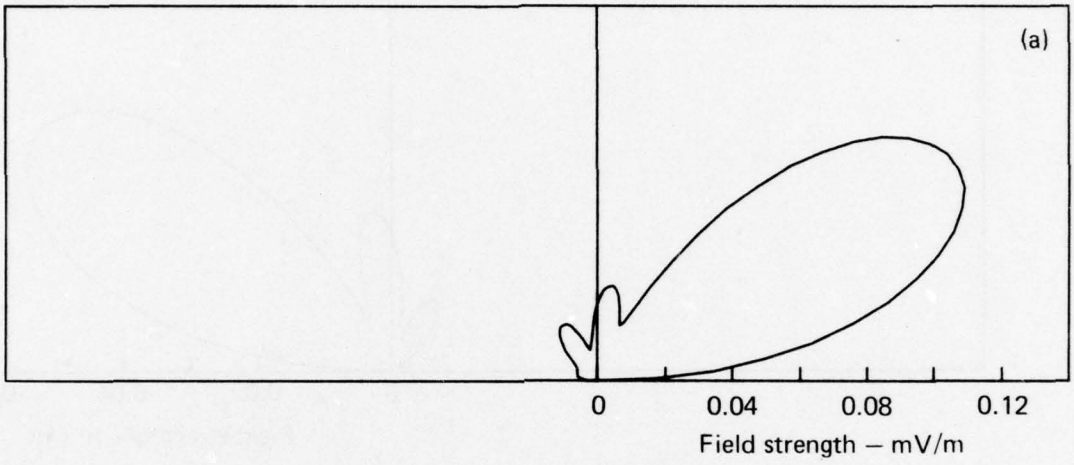

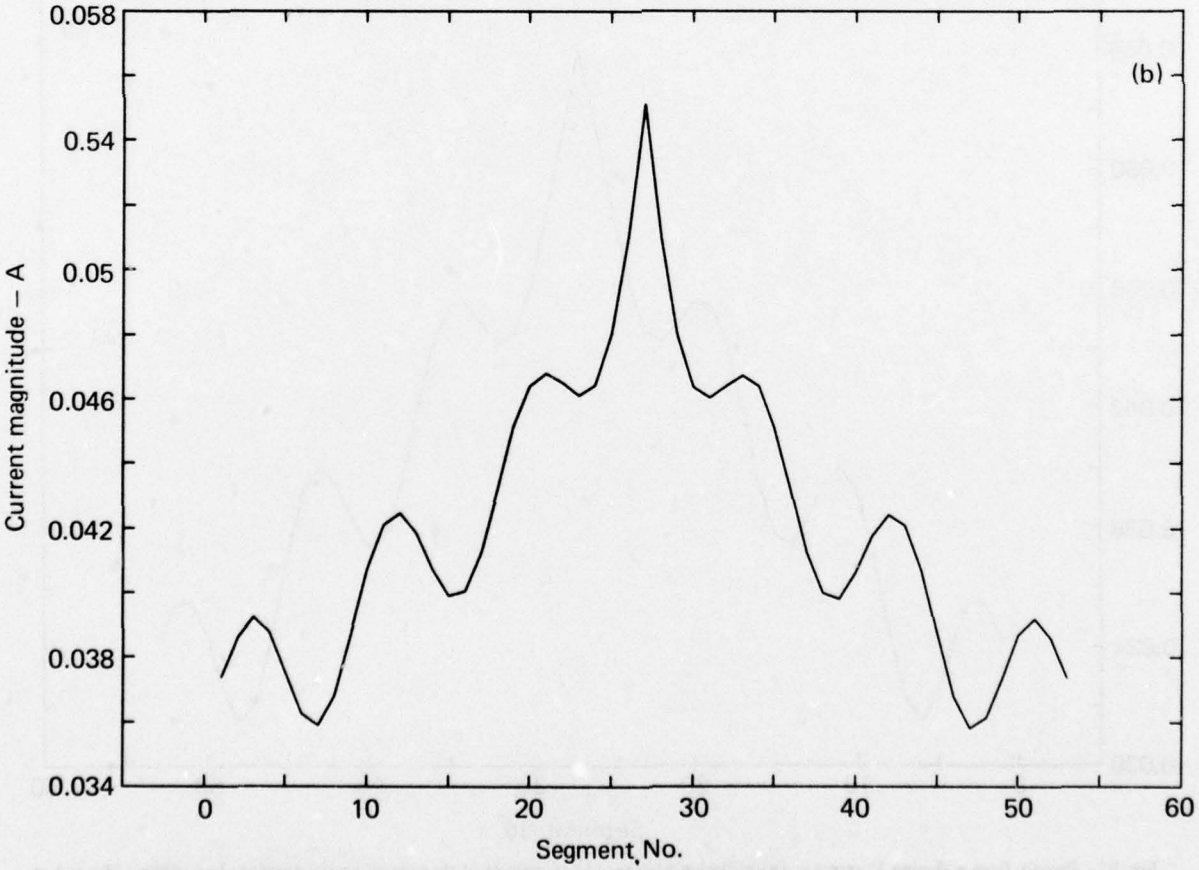

Fig. B6. Results from a sloping V antenna: (a) radiation pattern: (b) magnitude of the current on the antenna. L = 100 m; H_F = 10 m; freq = 10 MHz; $\alpha = 60°$; $R_{LOAD} = 300\ \Omega$.

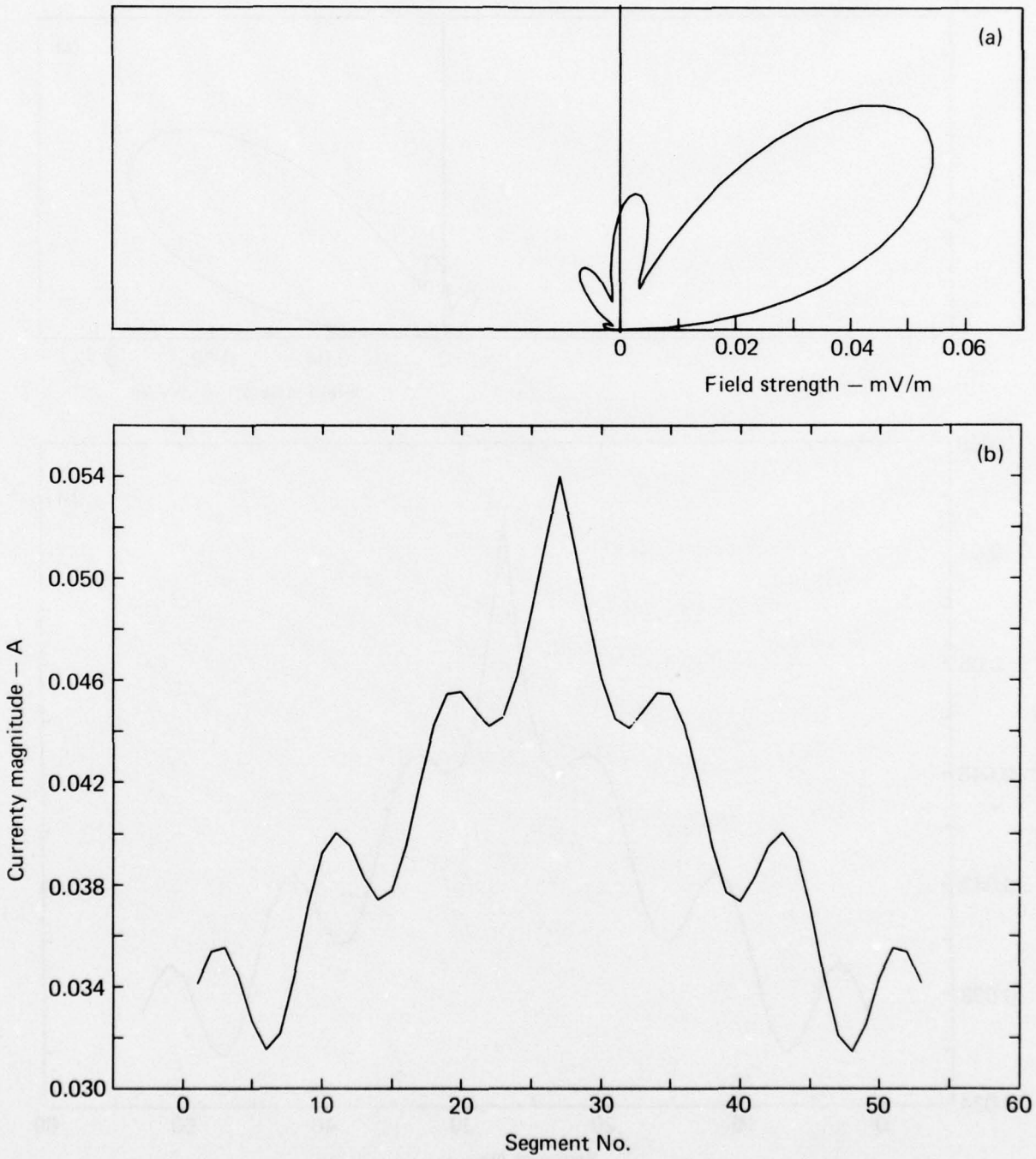

Fig. B7 Results from a sloping V antenna: (a) radiation pattern; (b) magnitude of the current on the antenna. L = 100 m; H_F = 2 m; freq = 10 MHz; $\alpha = 60°$; $R_{LOAD} = 300\ \Omega$.

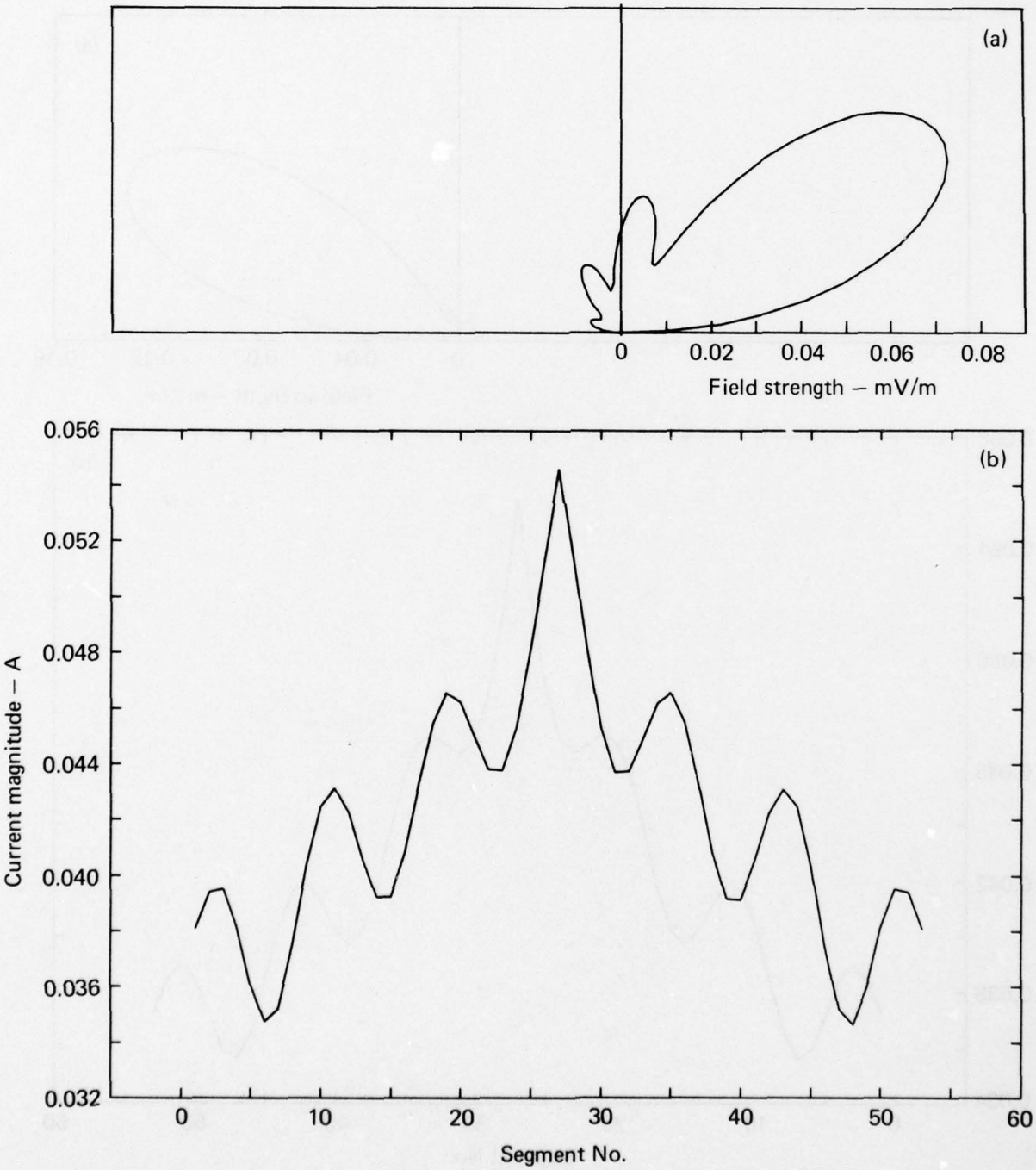

Fig. B8 Results from a sloping V antenna: (a) radiation pattern; (b) magnitude of the current on the antenna. L = 100 m; H_F = 5 m; freq = 10 MHz; $\alpha = 60°$; $R_{LOAD} = 300\ \Omega$.

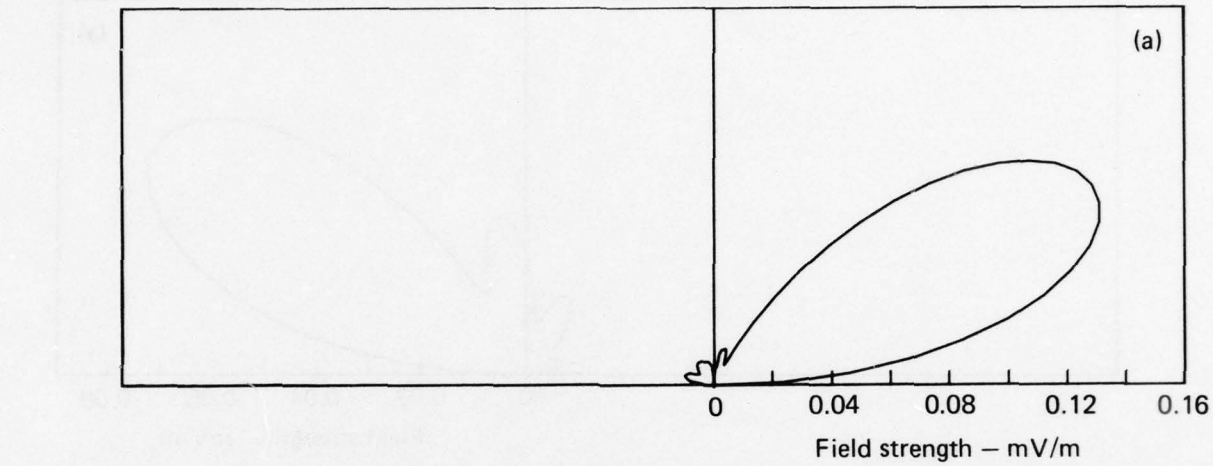
(a)
0
0.04
0.08
0.12
0.16
Field strength – mV/m

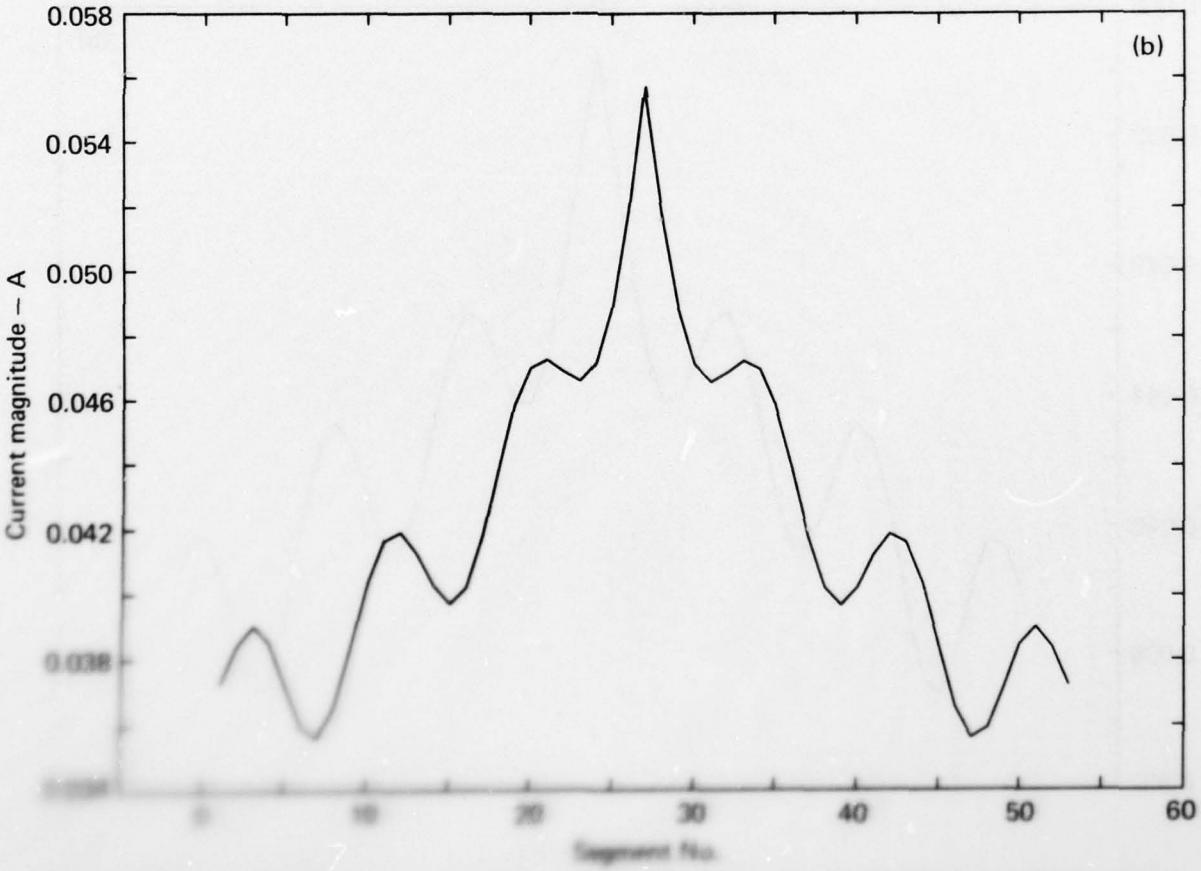
(b)
0.058
0.054
0.050
0.046
0.042
0.038
Current magnitude – A
10
20
30
40
50
60
Segment No.

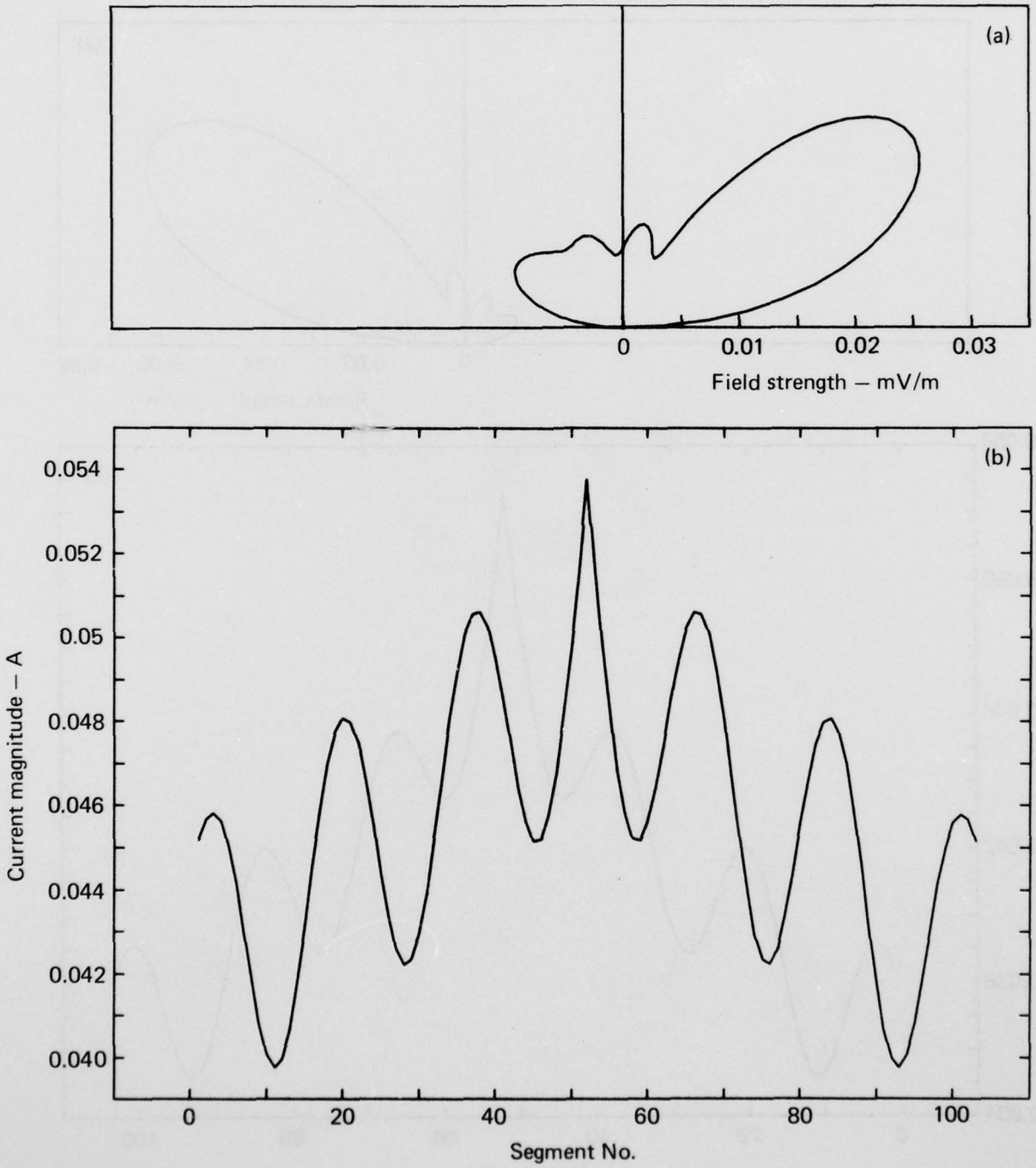

Fig. B10. Results from a sloping V antenna: (a) radiation pattern; (b) magnitude of the current on the antenna. L = 200 m; H_t = 10 m; freq = 10 MHz; $\alpha = 10°$; $R_{LOAD} = 300\ \Omega$.

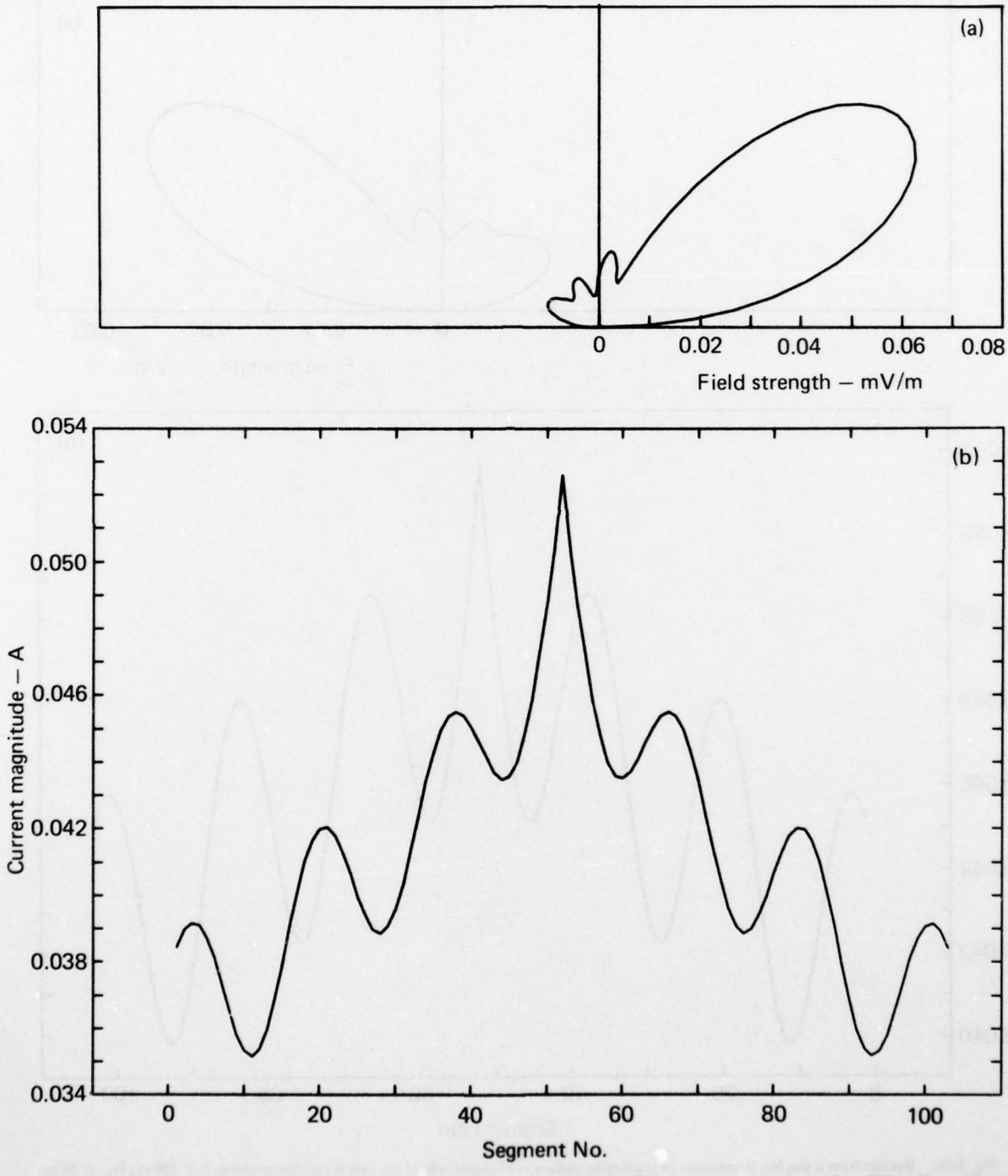

Fig. B11. Results from a sloping V antenna: (a) radiation pattern; (b) magnitude of the current on the antenna. L = 200 m; H_t = 10 m; freq = 10 MHz; α = 30°; R_{LOAD} = 300 Ω.

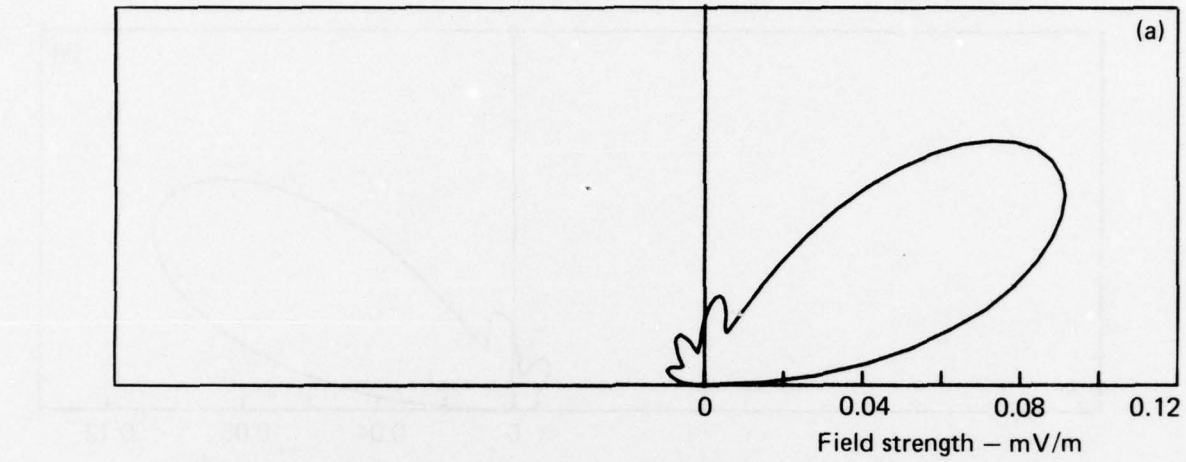

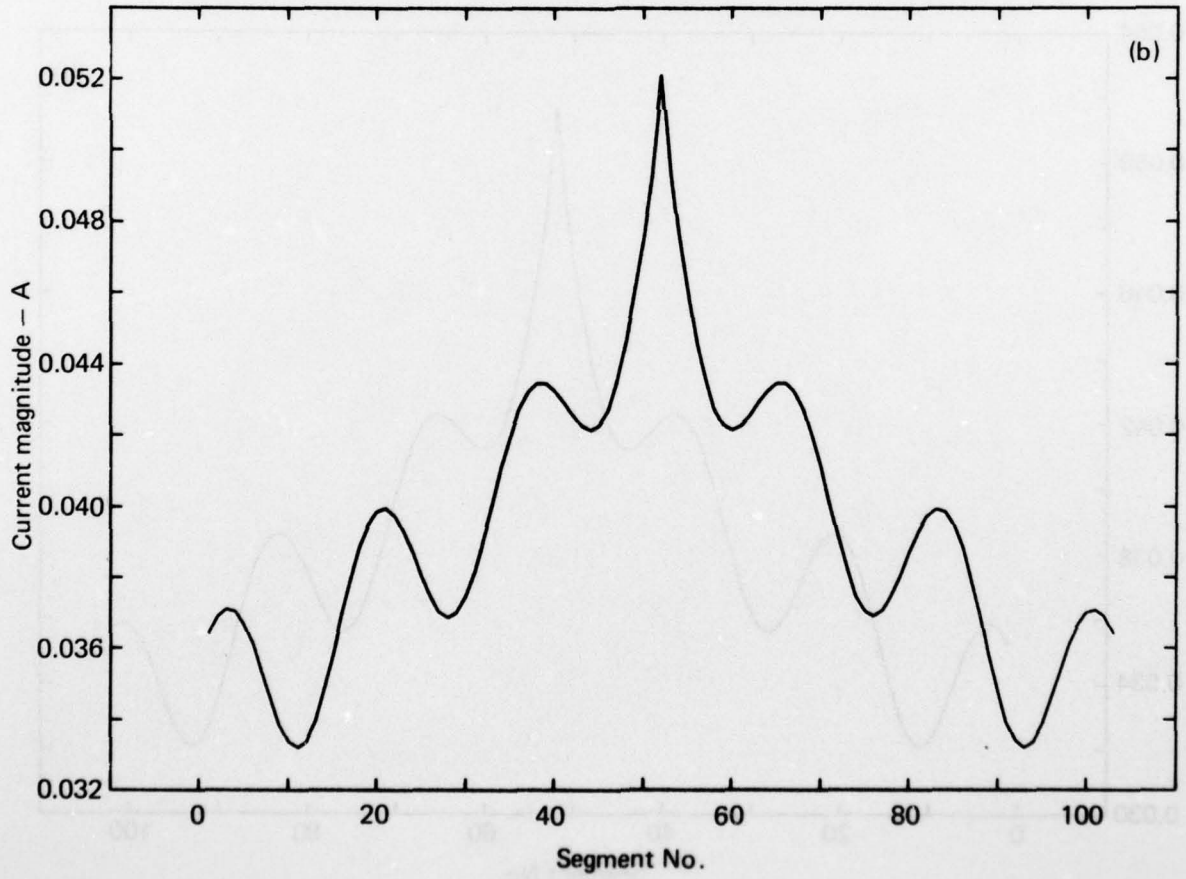

Fig. B12. Results from a sloping V antenna: (a) radiation pattern; (b) magnitude of the current on the antenna. L = 200 m; H_1 = 10 m; freq = 10 MHz; α = 50°; R_{LOAD} = 300 Ω.

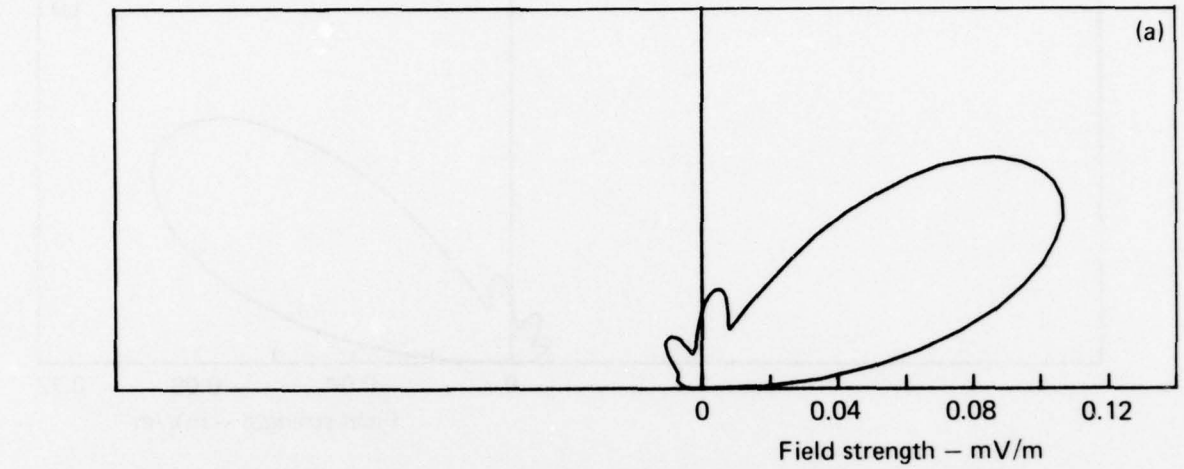

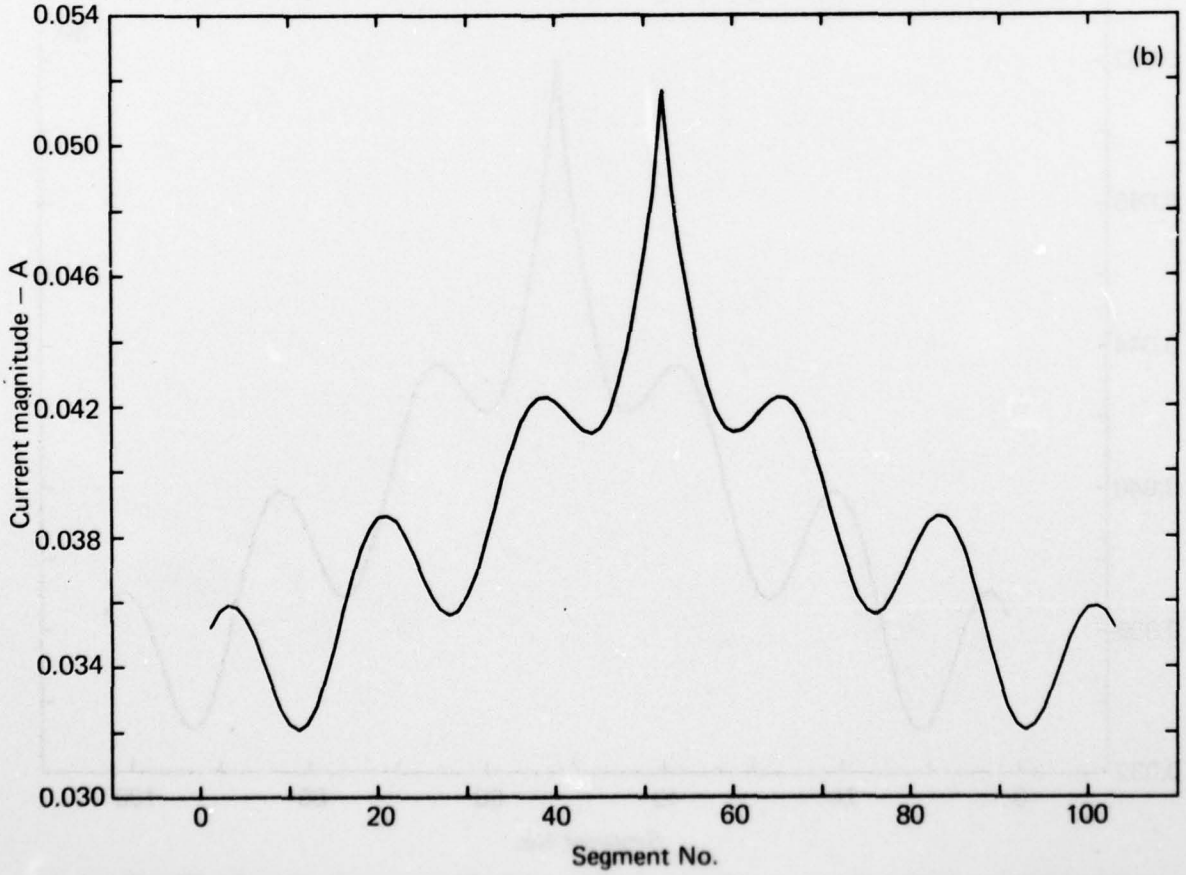

Fig. B13. Results from a sloping V antenna: (a) radiation pattern; (b) magnitude of the current on the antenna. L = 200 m; H_1 = 10 m; freq = 10 MHz; $\alpha = 70°$; $R_{LOAD} = 300\ \Omega$.

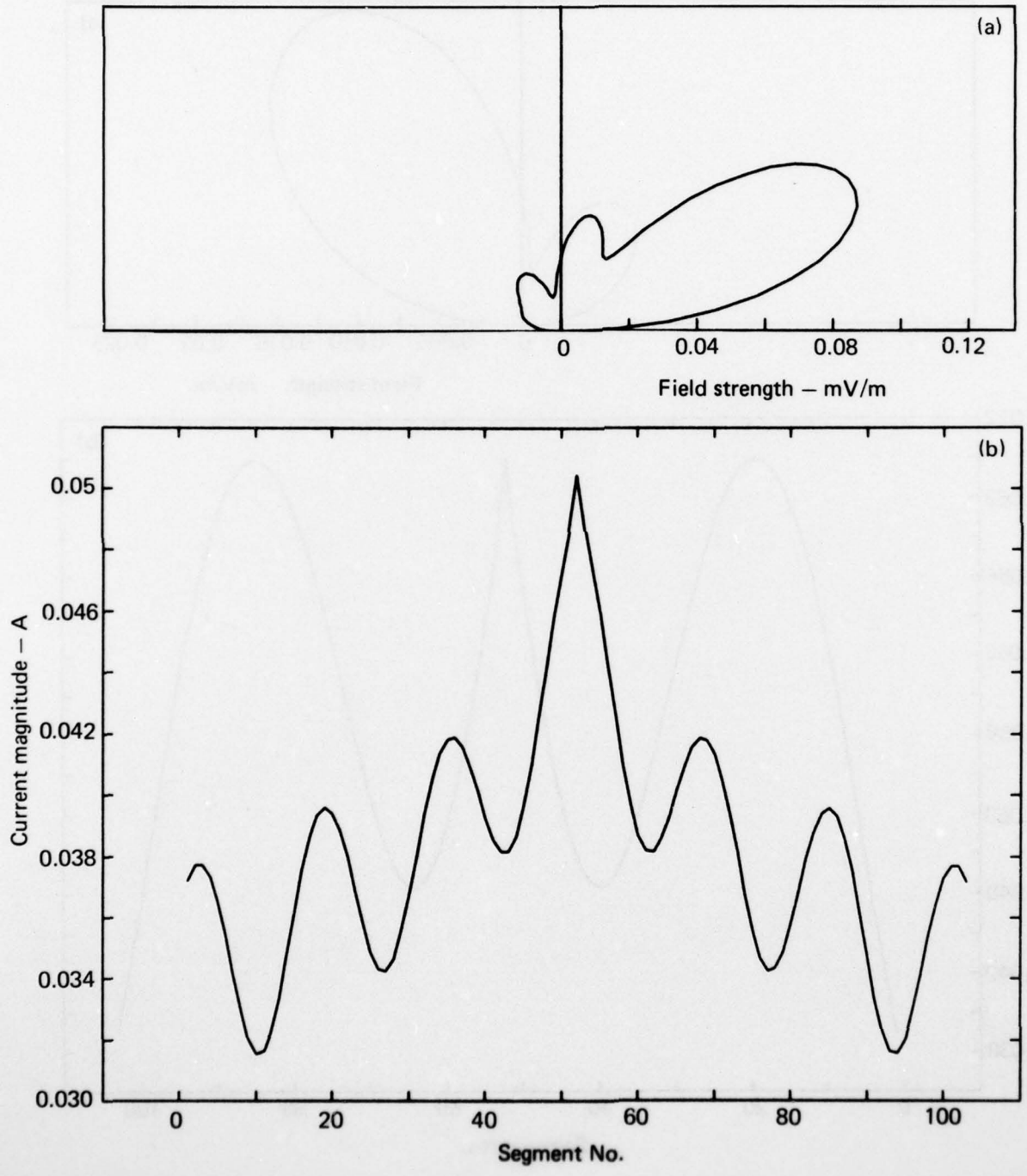

Fig. B14. Results from a sloping V antenna: (a) radiation pattern; (b) magnitude of the current on the antenna. L = 200 m; H_2 = 10 m; freq = 10 MHz; α = 90°; R_{LOAD} = 300 Ω.

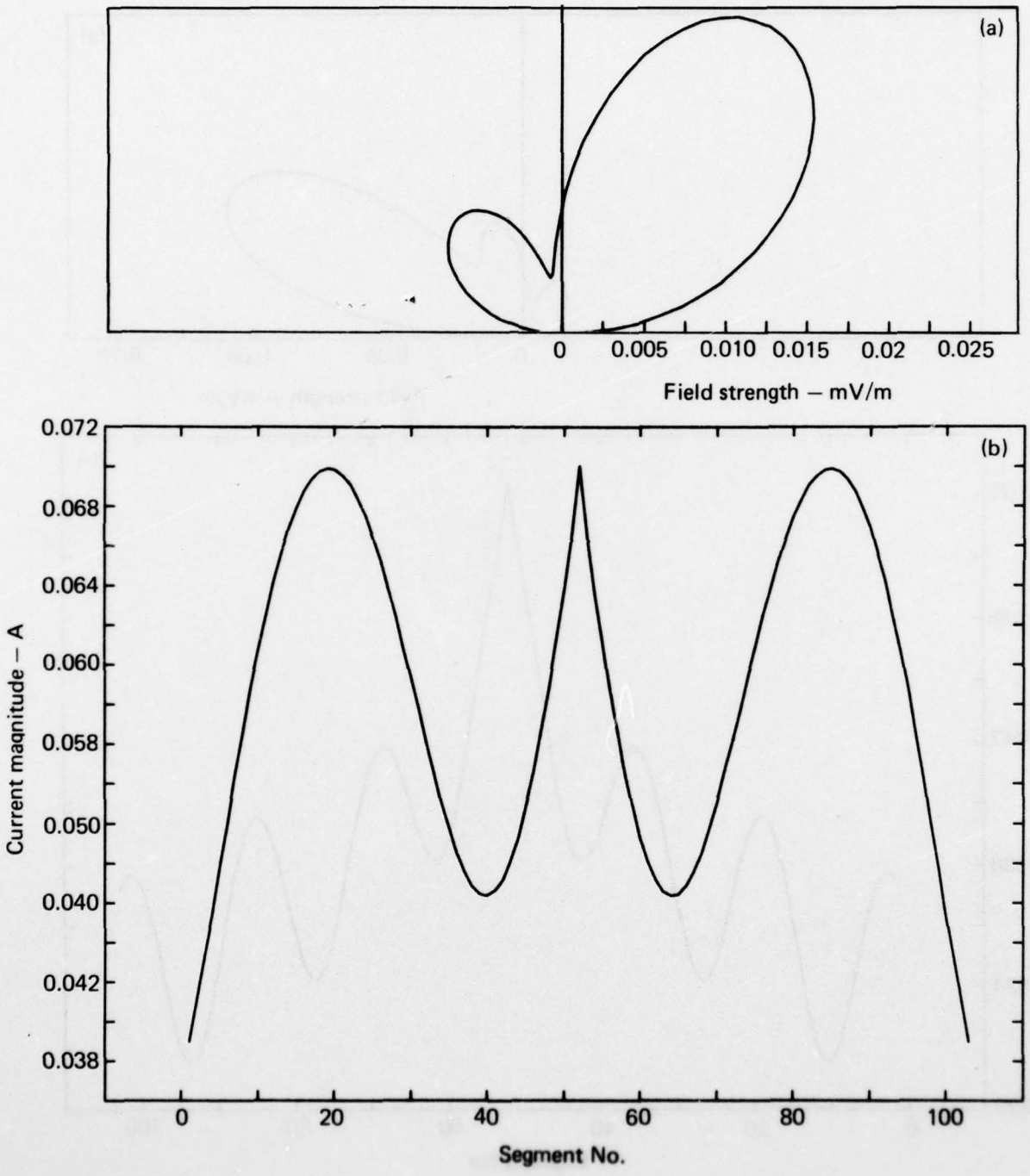

Fig. B15. Results from a sloping V antenna: (a) radiation pattern; (b) magnitude of the current on the antenna. L = 200 m; H_1 = 10 m; freq = 6 MHz; α = 10°; R_{LOAD} = 500 Ω.

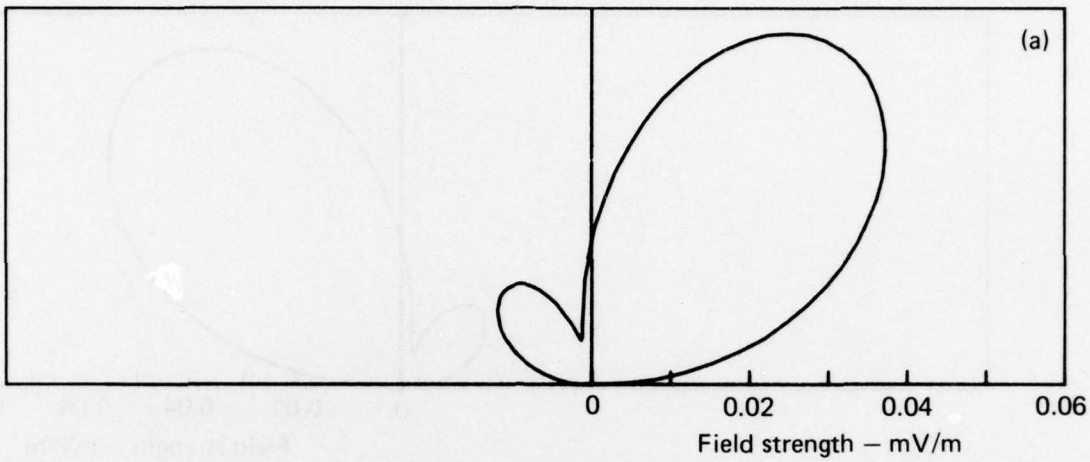

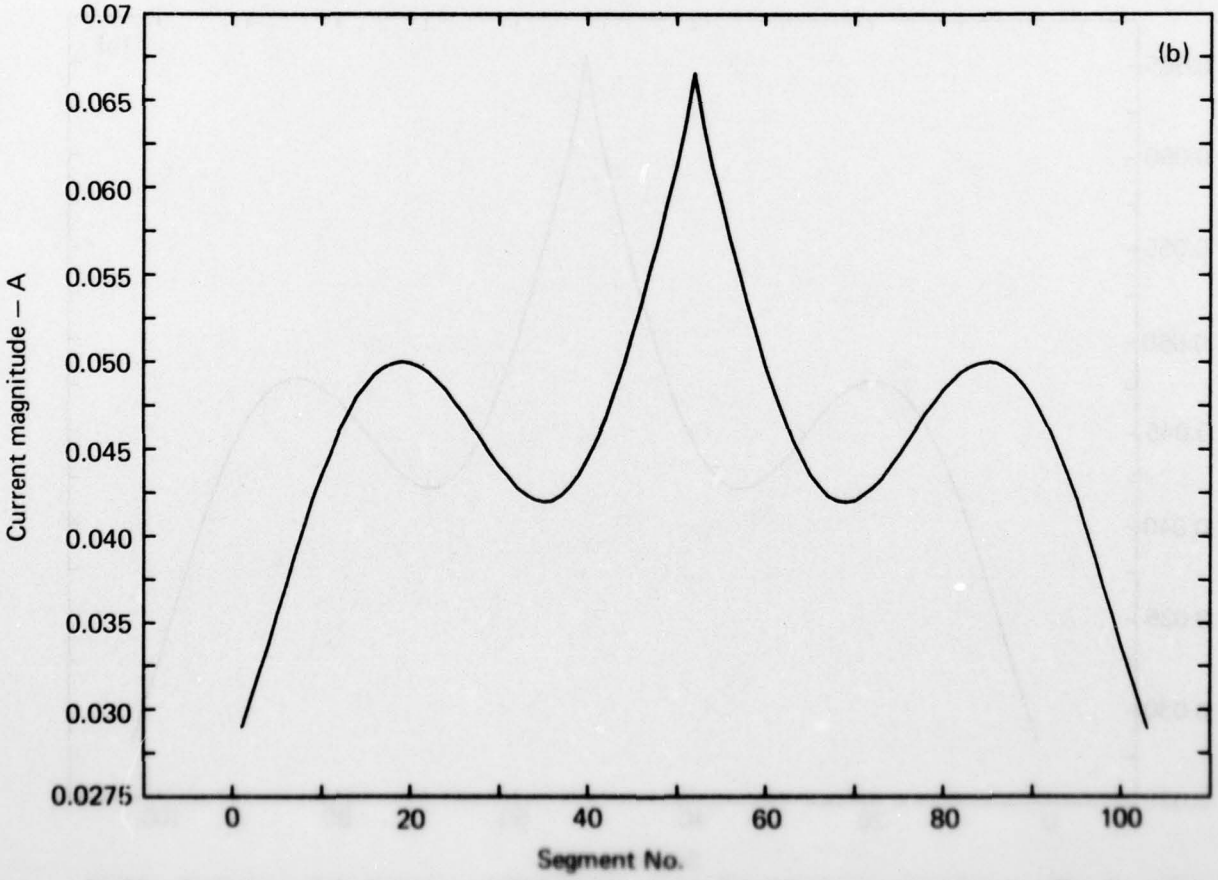

Fig. B16. Results from a sloping V antenna: (a) radiation pattern; (b) magnitude of the current on the antenna. l_1 = 200 m; H_1 = 10 m; f_{req} = 6 MHz; α = 30°; R_{Load} = 500 Ω.

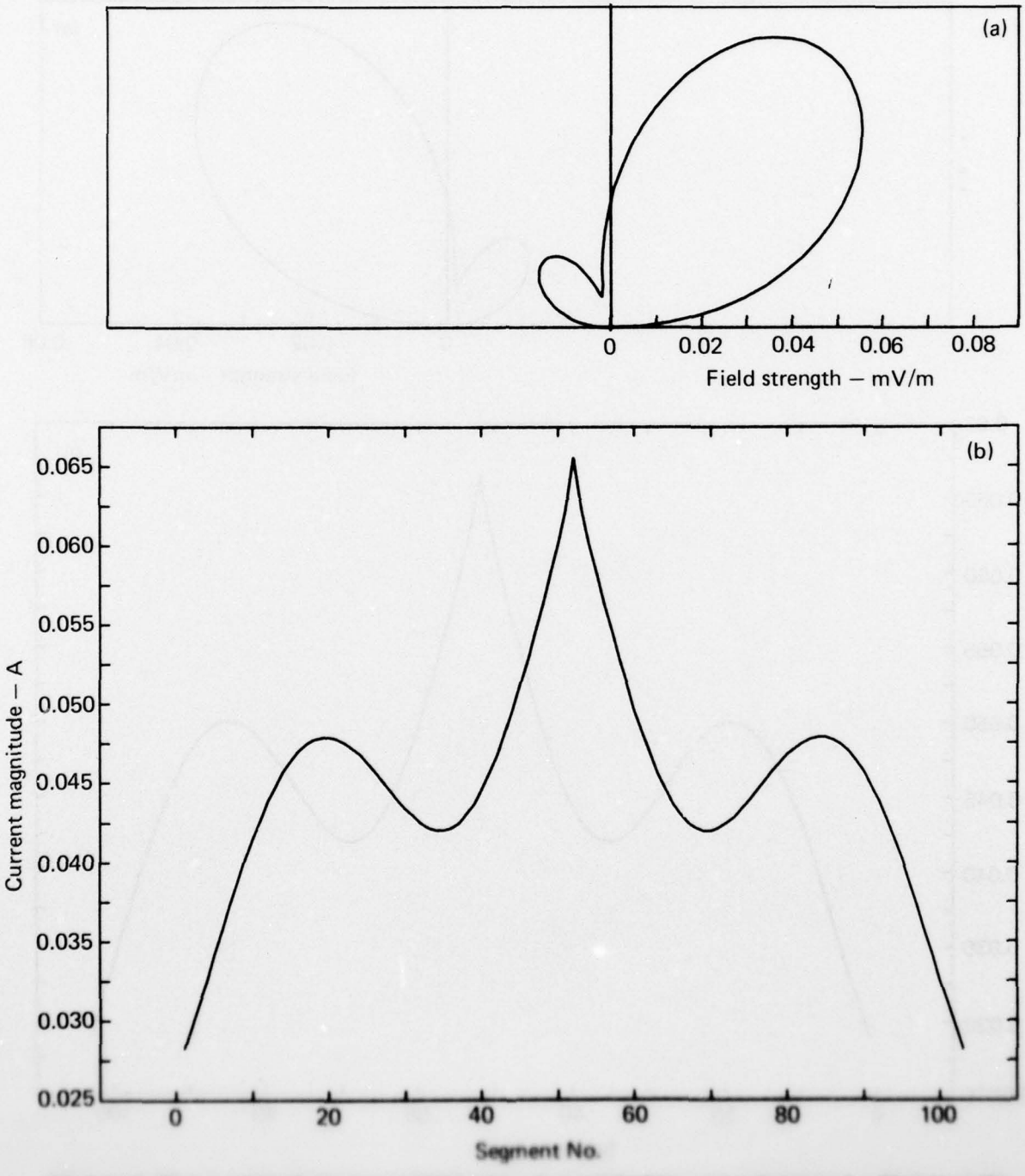

Fig. 8[illegible]. Results from a sloping V antenna: (a) radiation pattern; (b) magnitude of the current on the antenna. [illegible]

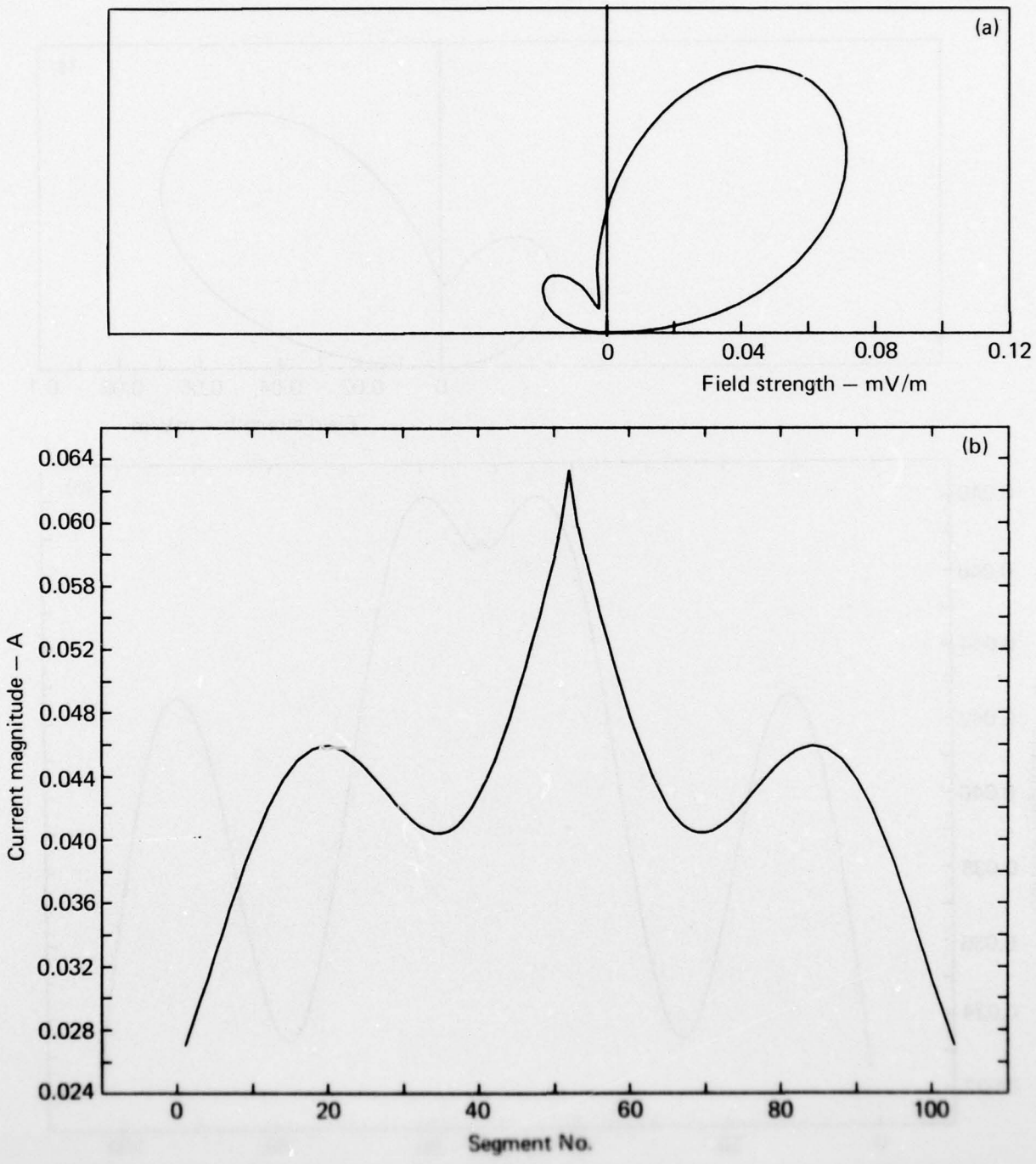

Fig. 5I8. Results from a sloping V antenna: (a) radiation pattern; (b) magnitude of the current on the antenna. L = 200 m; H_1 = 10 m; freq = 6 MHz; α = 70°; R_{ground} = 300 Ω.

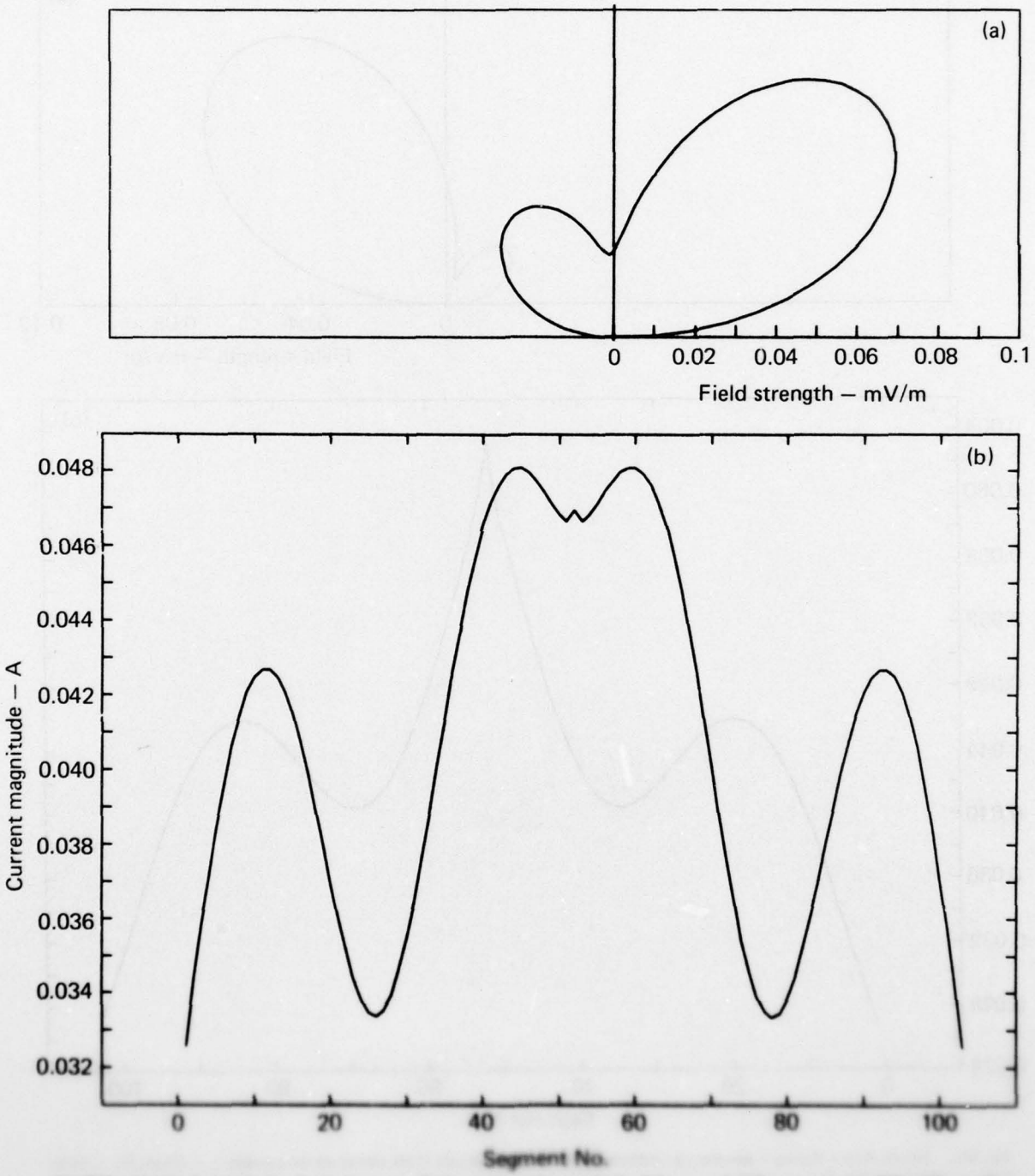
(a)
0
0.02
0.04
0.06
0.08
0.1
Field strength — mV/m
(b)
0.048
0.046
0.044
0.042
0.040
0.038
0.036
0.034
0.032
Current magnitude — A
0
20
40
60
80
100
Segment No.

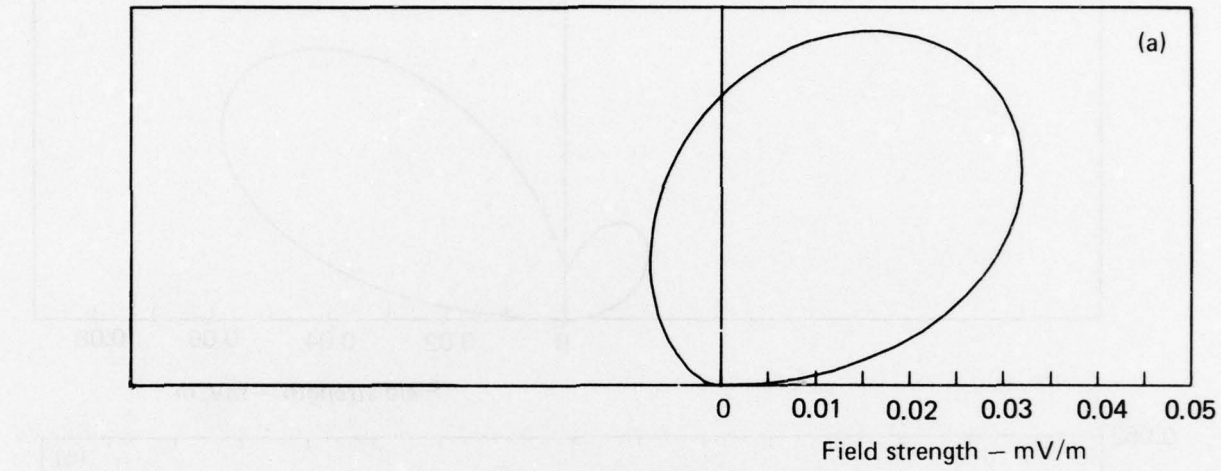
(a)
0
0.01
0.02
0.03
0.04
0.05
Field strength – mV/m

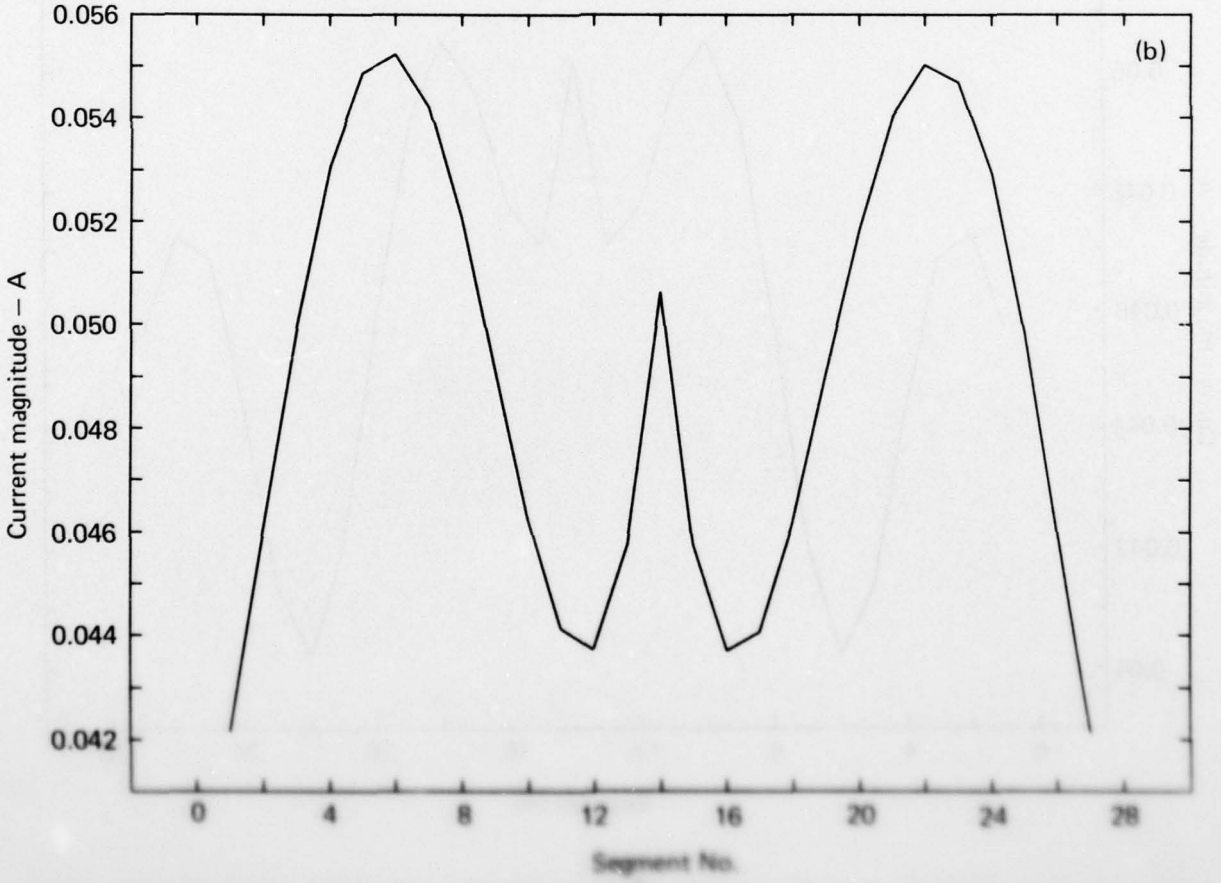
(b)
0.056
0.054
0.052
0.050
0.048
0.046
0.044
0.042
Current magnitude – A
0
4
8
12
16
20
24
28
Segment No.

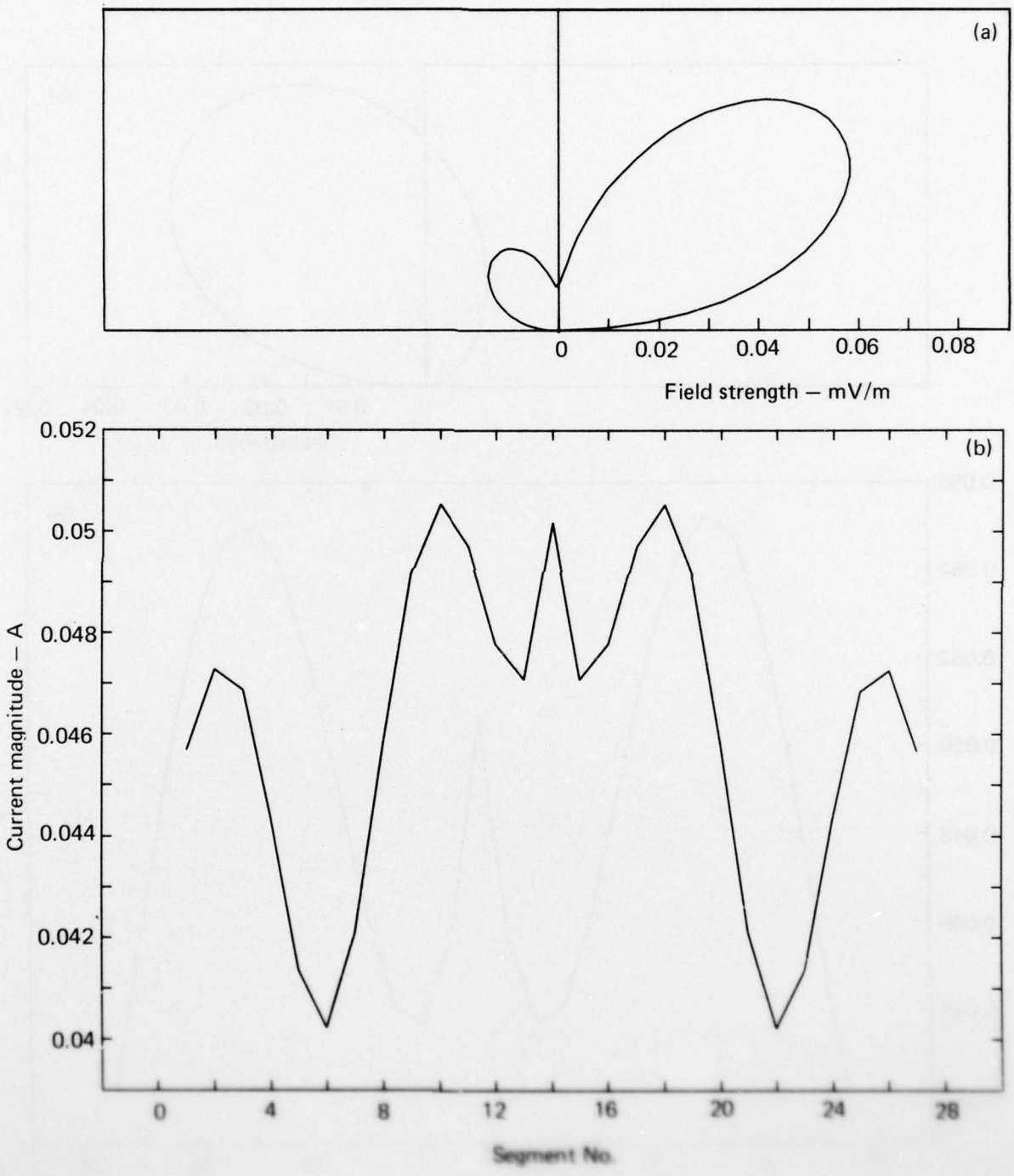
(a)
0
0.02
0.04
0.06
0.08
Field strength – mV/m
(b)
0.052
0.05
0.048
0.046
0.044
0.042
0.04
Current magnitude – A
0
4
8
12
16
20
24
28
Segment No.

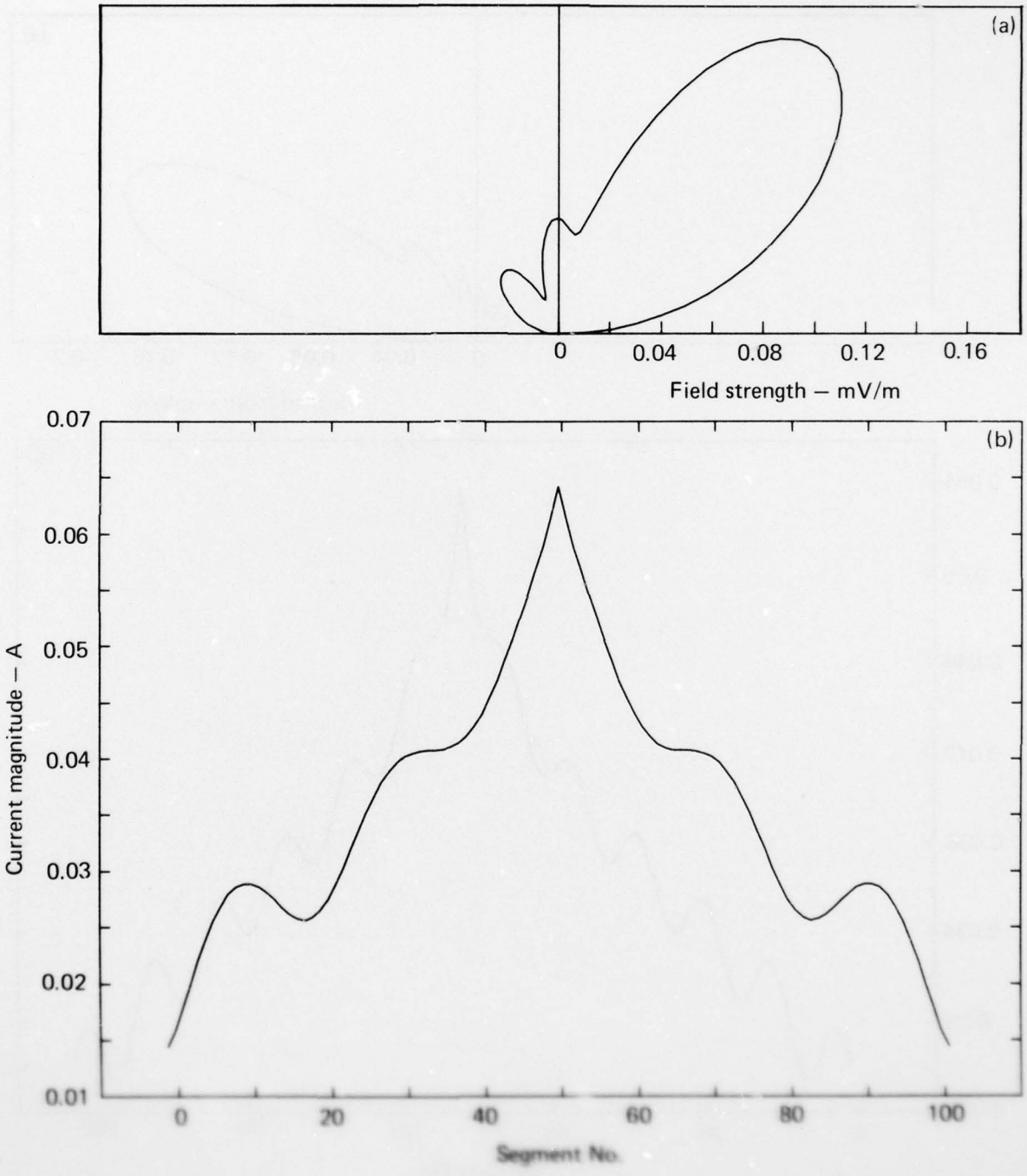
(a)
0
0.04
0.08
0.12
0.16
Field strength – mV/m
(b)
0.07
0.06
0.05
0.04
0.03
0.02
0.01
Current magnitude – A
0
20
40
60
80
100
Segment No.

AD-A056 732 CALIFORNIA UNIV LIVERMORE LAWRENCE LIVERMORE LAB F/G 20/14
SOMINT: AN IMPROVED MODEL FOR STUDYING CONDUCTING OBJECTS NEAR --ETC(U)
FEB 78 J N BRITTINGHAM, E K MILLER, J T OKADA W-7405-ENG-48
UNCLASSIFIED UCRL-52423 NL

2 OF 2
AD
A056732

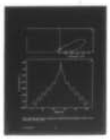

END
DATE
FILMED
9 -78
DDC

OF 2

56732

1.0
1.1
1.25
1.4
1.6
1.8
2.0
2.2
2.5
2.8
3.2
3.6
4.0
4.5
5.0

MICROCOPY RESOLUTION TEST CHART
NATIONAL BUREAU OF STANDARDS-1963-A

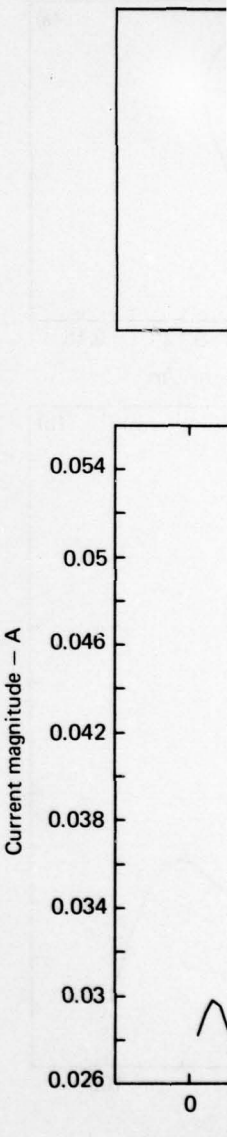

Fig. B23. Results fro
freq = 10 MHz; α = 6

GPO 789-086/4978

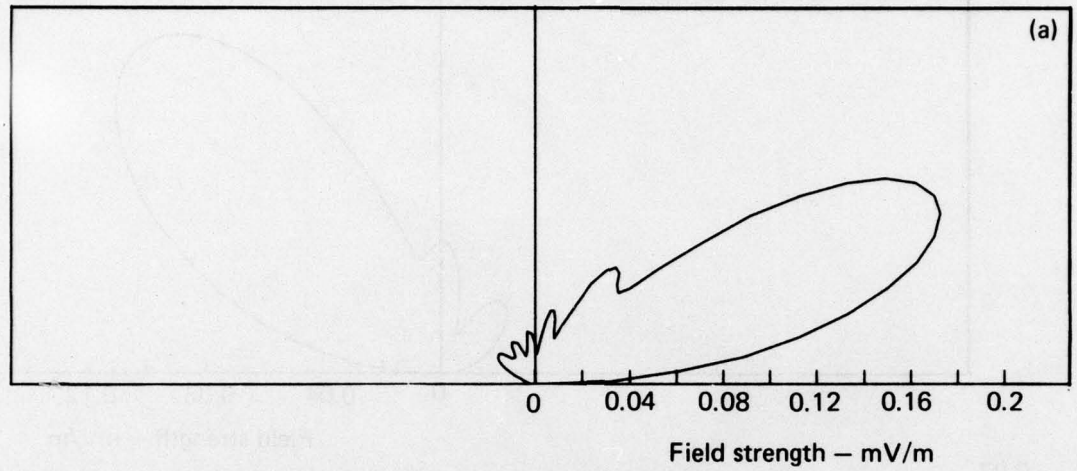

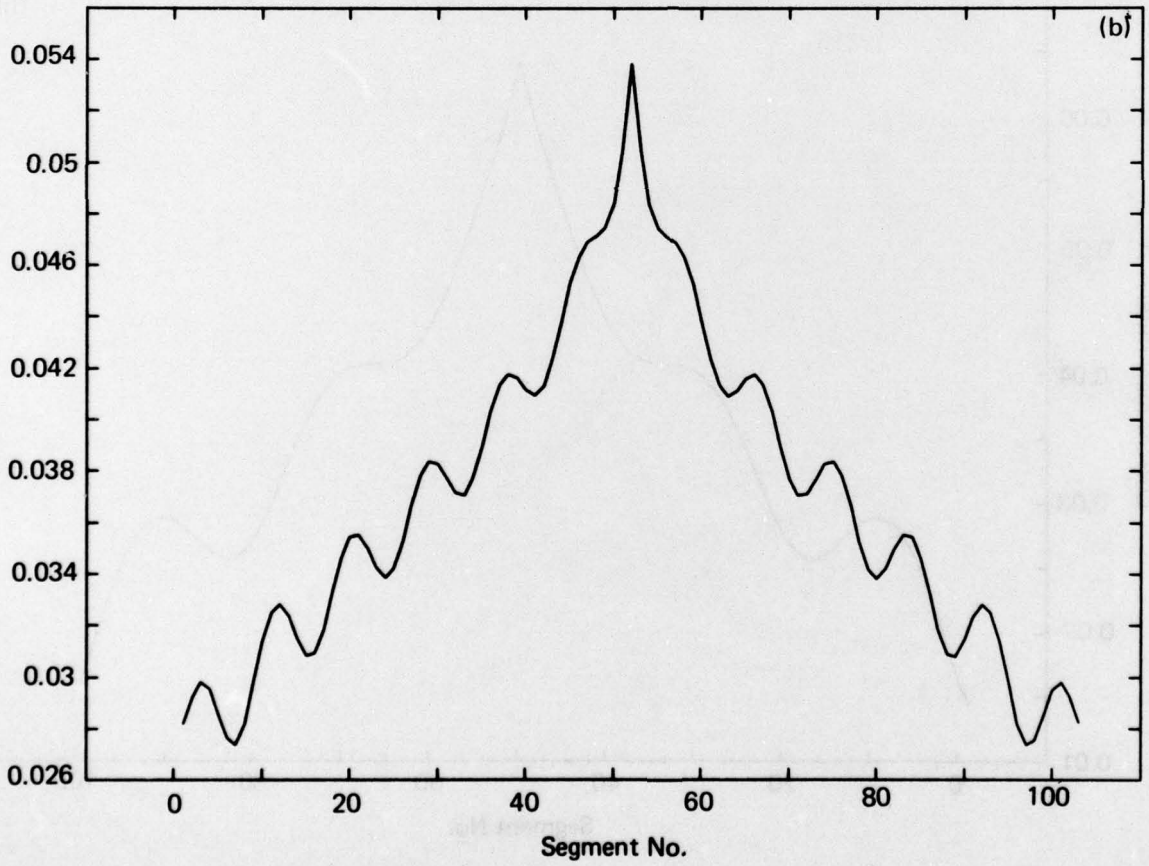

Fig. B23. Results from a sloping V antenna: (a) radiation pattern; (b) magnitude of the current on the antenna. L. = 200 m; H_t = 10 m; freq = 10 MHz; $\alpha = 60°$; $R_{LOAD} = 300\ \Omega$.